Politecnico di Torino

ScuDo
Scuola di Dottorato ~ Doctoral School
WHAT YOU ARE, TAKES YOU FAR

Doctoral Dissertation
Doctoral Program in Electrical, Electronics and Communications Engineering
(34th cycle)

Numerical Techniques for the Automated Design of Metasurface Antennas

By

Marcello Zucchi

******

Supervisor:
Prof. Giuseppe Vecchi

Doctoral Examination Committee:
Prof. Anthony Grbic, Referee, University of Michigan
Prof. Enrica Martini, Referee, Università degli Studi di Siena

Politecnico di Torino
2022

Declaration

I hereby declare that, the contents and organization of this dissertation constitute my own original work and does not compromise in any way the rights of third parties, including those relating to the security of personal data.

Marcello Zucchi
2022

* This dissertation is presented in partial fulfillment of the requirements for **Ph.D. degree** in the Graduate School of Politecnico di Torino (ScuDo).

Acknowledgements

This work was supported by the Italian Ministry of Research PRIN 2017S29ZLA "Metasurface Antennas for Space Applications". The author would like to thank the reviewers for their helpful comments.

Abstract

This thesis presents the theory and development of a novel approach for the automated design of metasurface antennas. The introduced method is fully numerical and can be applied to the design of 3D metasurfaces, allowing the transformation of a given incident field into a radiated field that satisfies mask-type amplitude constraints.

The design of metasurfaces is challenging due to their intrinsic multi-scale features, as they are composed by many subwavelength scattering elements. The process is made possible by the introduction of macroscopic models that describe the behaviour of the metasurface in terms of an equivalent *impedance boundary condition* (IBC), which defines the relationship between the tangential electric and magnetic fields on either side of the metasurface. To be implemented in practice, the obtained impedance must be *realizable*, i.e., it must be passive and lossless, with reactance values within practical manufacturing limits.

In this work the focus is on the *macroscopic* design of metasurfaces, i.e., the design of the surface impedance profile that leads to the desired radiated field. Common techniques for the macroscopic design of metasurface antennas rely on analytical approximations for the incident and scattered fields, as well as for the impedance profile. This limits their application to simple geometries, and the ability to deal with arbitrary specifications is minimal. To overcome these limitations, recently new approaches have been proposed which frame the design as an inverse source problem, allowing more generality in the definition of the incident and scattered fields. However, they are formulated as an input-output field transformation on the two sides of a metasurface, preventing their application to cases where the incident field is on the surface (e.g., surface wave based metasurface antennas).

The method introduced in this work is based on a formulation of the scattering problems as an *integral equation*, where the unknown is the equivalent electric current only. The process involves the synthesis of this current, constrained to correspond to a

realizable impedance, and to radiate a field obeying the requirements. The impedance is obtained from the synthesized current only at the end of the process. This method requires no a-priori information or heuristics on the impedance distribution.

The current-based design avoids the solution of the forward problem at each iteration, greatly reducing the computational burden, and the formulation is such that all relevant operations in the iterative process can be evaluated with $O(N \log N)$ complexity, where N is the number of unknowns for the current. Another benefit is the ability to enforce mask-type (inequality) constraints, as opposed to pattern matching techniques adopted by previous methods, allowing to incorporate all relevant figures of merit (gain, side-lobe levels, polarization ratio, etc.) directly into the design instance.

To demonstrate the validity of the proposed method, it has been applied to the design of metasurface antennas of practical relevance. Application examples concentrate on the case of on-surface incident field and far-field pattern specifications in terms of realized gain. The obtained results confirm the feasibility of the macroscopic design for medium- and large-size circular metasurfaces, with pencil- and shaped-beam patterns, and for both linear and circular polarization. Design examples for different geometries, i.e., elliptical and symmetric strip, are also included to demonstrate the flexibility of the approach.

Contents

List of Figures

List of Tables

Chapter 1

Introduction

In the last decade, the use of *metasurfaces* for the manipulation of electromagnetic fields has been a topic of continuously expanding relevance [1]. They find application in several areas, from antennas to microwave components, and over a wide range of frequencies, from microwaves to optical ones. Examples include low-profile antennas, lenses, polarizers and radomes; reflectarrays and transmitarrays have also seen realization with metasurfaces. Recently, the concept of reconfigurable intelligent surfaces (RIS) [2] has been proposed for 5G and beyond-5G environments. In all these applications, the metasurface interacts with an incident, assigned field, generating the radiated field; the metasurface is engineered so that this radiated field has the desired properties.

From the structural point of view, metasurfaces are a class of artificial surfaces that represent the two-dimensional version of metamaterials, as they are formed by the arrangement (usually periodic) of sub-wavelength scattering elements on a thin supporting layer. By varying the size and shape of these individual elements, it is possible to tailor the electromagnetic behaviour of the surface, achieving properties that cannot be commonly found in nature. They can be realized with a variety of technologies: currently, the most popular ones are the use of printed conductive elements (e.g., patches, slotted patches, meanders, etc.) and all-metal pillars (Fig. 1.1). Within printed-type structures, the main difference between the various classes is in terms of the number of layers: low-profile antennas are usually single-layer, while trasmit-type structures require more than one layer to ensure functionality and absence of reflection. Another difference is in the nature of the incident (source) field:

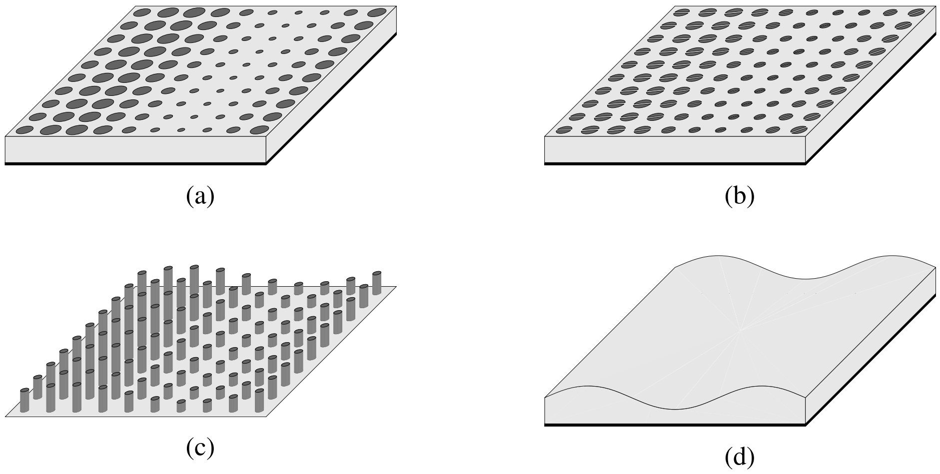

Fig. 1.1 Different technologies for the realization of spatially-variable metasurfaces: (a) printed circular patches with variable radius, (b) slotted circular patches, (c) metallic pillars with variable heights, and (d) grounded dielectric slab with variable thickness.

in low-profile antennas it is usually generated by a feed embedded in the surface (e.g., through a pin), which launches a guided surface wave in the grounded dielectric; in all other cases, the feed is external and illuminates the metasurface.

The full-wave analysis of metasurface antennas is challenging due to their multiscale features: many sub-wavelength unit cells are combined to form surfaces that can have a large size in terms of wavelengths. However, their macroscopic behaviour can be effectively modelled in terms of constitutive surface parameters, that determine the appropriate boundary conditions [3]; these parameters are derived through homogenization techniques that depend on the size of the unit cells and the operating frequency.

The representation in terms of a continuous distribution of equivalent surface impedance has not only enhanced the electromagnetic analysis of large metasurface antennas, but it has also enabled their design, by allowing the process to be carried out in two distinct phases. The design aims at finding the spatial distribution of a surface impedance; after that, the final layout is achieved by choosing suitable unit cells and finding their parameters so that they produce the previously determined impedance profile. The unit cell analysis is usually done with the assumption of local periodicity, which is the approach followed by virtually all published works (see [4] for an application of this approximation). The choice of the unit cells is not part of this work and can be realized with a variety of existing approaches, e.g., [5, 6].

The conception and systematic design of spatially varying metasurfaces has been initially based on wave physics and analytical considerations, e.g., [7, 8], [6, 9]. However, analytically-based approaches cannot accommodate for arbitrary design specifications, which has prompted for research into automated design algorithms based on numerical techniques. Ideally, the process would be totally automatic, starting from the specifications and ending with the metasurface layout, requiring no extra information or user intervention. The demand for such methods motivated the research presented in this work.

1.1 State of the Art

The state of the art for the design of metasurface antennas can be conceptually divided into two main categories: "2D" and "3D" methods. The cases in which one spatial coordinate is considered invariant or periodic in the design – and thus ignorable – are termed "2D", while this restriction is not present for "3D" methods. Another important distinction is between two different types of field specifications: pattern-matching and mask-type inequalities. In pattern-matching the objective is to obtain a given field, i.e. minimizing the "error" from this given pattern. Mask-type specifications, on the other hand, are more general (and more useful in practice): an "ideal" pattern is not known, and instead the field amplitude is required to satisfy inequalities, i.e., to lie within an upper and lower bound; the spatial variations of the bounds are called "masks". A practically relevant sub-class of this problem is the one in which one seeks to maximize the main beam gain in the prescribed direction. Consistent with the scope of this work, only those approaches that aim at the fully numerical design of the metasurface will be reviewed.

2D methods The approach in [10] employs a dual optimization, considering equivalent currents and impedance at the same time, with an alternating type of optimization; this requires a solution of the forward problem at each step. A method based on optimizing the currents only would dispense from the solution of the forward problem during the iterations: an important step in this direction is in [11, 12] where reactivity is enforced directly; the resulting (non-convex) optimization instance is tackled with a global optimization algorithm, but this approach was further improved in [13], employing a gradient-based optimization. Consistent with previous works, also [14] explicitly considers a transmission-reflection problem through the (stacked) metasurface layers, i.e., for an exciting field not generated on-surface. For this problem, fields are represented in terms of traveling waves in each (sub-wavelength) unit cell: this allows to formulate the problem directly in terms of circuit elements, with the currents expressed through them; as a result, the circuit elements are the direct unknowns of the inverse problem, with passivity and absence of losses intrinsically enforced. These important works address the problem of (phaseless) pattern matching —as opposed to mask-type (inequality) field specifications. A scattering approach to synthesis is also presented in [15]. In [16] a multi-layer, dual-band method is presented for a transmission-type metasurface with pattern-matching requirements; the method builds upon the work in [17]. The design is done in two steps: in the first step, equivalent currents are synthesized without passivity requirements and complex impedance values are obtained from these; in the second step, reactance values are optimized to match the field produced by the complex impedance. Finally, [18] addresses the electromagnetically consistent optimization of the surface impedance in RIS at a design and system level.

3D methods Regarding “3D” methods, the work in [19–21] employs equivalent currents only, expressed in terms of entire-domain basis functions for circular and elliptical domains; the method requires to formulate the problem as an amplitude and phase field matching. In [22] equivalent currents are first found from radiated field mask-type requirements, and a 3D realizable metasurface is subsequently obtained via optimization (involving machine learning) and exploiting the degrees of freedom of non-radiating currents (similar to [23]). The work in [24] lies between 2D and 3D methods. It performs the automated design of a 2D metamaterial with cylindrical symmetry, using a 2D FEM forward problem with a constrained gradient-based method. A similar approach is adopted in [25], where the forward problem is dealt with in terms of a 2D circuit network solver, using reduced-order models of the unit cells to reduce the computational load. Finally, the works in [26] and [27] employ a global optimization. At each iteration, a solution to the forward problem is required; to reduce its cost, [26] exploited the body-of-revolution (BOR) symmetry, while [27] specialized entire-domain basis functions [28]. Finally, global optimization of unit cell and limited size binary metasurfaces have also been reported in the literature, e.g., in [29].

1.2 Aim of this work

The present work introduces an automatic 3D method for the design of metasurface antennas. The procedure aims to find a *passive* and *lossless* impedance profile (as required for the physical implementation), with constraints on the values of the surface reactance (imposed by technological limits), and allowing arbitrary mask-type specifications on the radiated field. The dissertation focuses on the design of scalar impedance profiles, although the requirements of passivity and absence of losses are formally derived for the general case of tensorial impedance.

The goal is reached by a formulation of the electromagnetic scattering problem as a Surface Integral Equation (SIE), and involves the gradient-based optimization of *only* the surface equivalent electric current derived from it. This allows to leverage readily available numerical methods for the solution of integral equations. The numerical challenges arising from a 3D problem and the size of the structure are addressed by a formulation that is computationally efficient, requiring a minimal number of matrix-vector products per iteration. The objective function and its gradient can be computed with almost-linear, $O(N \log N)$ complexity (N is the number of unknowns for the current) via the so-called fast formulation of the forward problem. Finally, the line search procedure is computed in a fast, iterative way with consecutive approximation of the objective function with fourth-order polynomials that are minimized analytically.

The incident field is arbitrary, although this work mainly deals with the case where the source is embedded on the surface, as necessary in low-profile metasurface antennas. This represents one of the most challenging design scenarios, as the coupling between the source and the metasurface is much stronger than in externally-fed antennas (e.g., reflectarrays). Hence, controlling the reflected power becomes crucial.

1.3 Thesis outline

The thesis is composed of four main chapters, which are organized as follows:

- Chapter 1 introduces the concept of metasurface antennas and their design. The state of the art is reviewed and the aim of the thesis is stated.

- Chapter 2 presents the analytical and numerical formulation needed for the analysis of metasurface antennas. The concept of impedance boundary condition is introduced, and the requirement for passivity and losslessness are derived for scalar and tensorial impedances. The SIE formulation is defined, along with the numerical methods adopted for its solution. These concepts form the basis for the design approach presented in the next chapter.
- In Chapter 3, the proposed approach for the automatic design of metasurface antennas is described, both from the conceptual and the algorithmic point of view. The constraints are formally defined, and the current-based optimization algorithm is outlined. Lastly, the resulting numerical complexity is analyzed.
- Chapter 4 collects a series of numerical results for a variety of geometries and target pattern configurations. The method is applied to design circular metasurfaces of different electrical size, as well as elliptical ones and strip antennas. Both linear and circular polarizations are considered, with pencil beam and shaped beam patterns. The effectiveness of the proposed approach is validated by the solution of the forward EFIE-IBC system with the obtained impedance profile.
- In Chapter 5, a brief summary of the presented material is given, along with possible future developments and improvements.

Chapter 2

Analysis of Metasurface Antennas

In this chapter, the framework for the analysis of metasurface antennas is introduced. Starting from the impedance boundary condition needed for the modelling of the metasurface, the integral equation formulation is derived. Lastly, the numerical methods commonly used to solve these electromagnetic problems are presented.

2.1 Impedance Boundary Condition

The metasurface is modelled as an *Impedance Boundary Condition* (IBC) [3], which relates the tangential electric field to the jump of the tangential magnetic field:

$$\boldsymbol{E}_{\tan} = \overline{\overline{\boldsymbol{Z}}} \cdot \left[\hat{\boldsymbol{n}} \times (\boldsymbol{H}^{+} - \boldsymbol{H}^{-})\right] , \tag{2.1}$$

where $\overline{\overline{\boldsymbol{Z}}}(\boldsymbol{r})$ is the space-varying value of the impedance parameter, which in general is of tensorial nature. Superscripts $+$ and $-$ refer to the two sides of the surface ($\hat{\boldsymbol{n}}$ points toward the $+$ side), and $\boldsymbol{E}_{\tan} = \left(\overline{\overline{\boldsymbol{I}}} - \hat{\boldsymbol{n}}\hat{\boldsymbol{n}}\right) \cdot \boldsymbol{E}$ is the electric field tangential to the surface. The term “impedance” comes from the fact that a discontinuity of the tangential magnetic field is due to an equivalent surface electric current $\boldsymbol{J} = \hat{\boldsymbol{n}} \times (\boldsymbol{H}^{+} - \boldsymbol{H}^{-})$, and the IBC can be equivalently written as

$$\boldsymbol{E}_{\tan} = \overline{\overline{\boldsymbol{Z}}} \cdot \boldsymbol{J}. \tag{2.2}$$

The value of the $\overline{\overline{\boldsymbol{Z}}}$ is derived from the geometry of the unit cell, through homogenization techniques that differ depending on the application (see, e.g., [6]). As this work deals only with the reconstruction of the impedance profile, these techniques will not be discussed further.

A tensor impedance is modelled by choosing a local orthonormal basis $(\hat{\boldsymbol{u}}, \hat{\boldsymbol{v}})$, and introducing four basis dyadics as follows [30]:

$$\overline{\overline{\boldsymbol{I}}} = \hat{\boldsymbol{u}}\hat{\boldsymbol{u}} + \hat{\boldsymbol{v}}\hat{\boldsymbol{v}}, \tag{2.3}$$

$$\overline{\overline{\boldsymbol{N}}} = \hat{\boldsymbol{v}}\hat{\boldsymbol{u}} - \hat{\boldsymbol{u}}\hat{\boldsymbol{v}} = \hat{\boldsymbol{n}}\times\overline{\overline{\boldsymbol{I}}}, \tag{2.4}$$

$$\overline{\overline{\boldsymbol{K}}} = \hat{\boldsymbol{u}}\hat{\boldsymbol{u}} - \hat{\boldsymbol{v}}\hat{\boldsymbol{v}}, \tag{2.5}$$

$$\overline{\overline{\boldsymbol{L}}} = \hat{\boldsymbol{v}}\hat{\boldsymbol{u}} + \hat{\boldsymbol{u}}\hat{\boldsymbol{v}}. \tag{2.6}$$

Other basis can be used (e.g., $\hat{\boldsymbol{u}}\hat{\boldsymbol{u}}$, $\hat{\boldsymbol{u}}\hat{\boldsymbol{v}}$, $\hat{\boldsymbol{v}}\hat{\boldsymbol{u}}$ and $\hat{\boldsymbol{v}}\hat{\boldsymbol{v}}$), but this choice offers some advantages in the analysis of passive and lossless metasurfaces, as will be made clear in the next section. The general form of a tensor impedance takes the form

$$\overline{\overline{\boldsymbol{Z}}} = Z_{\scriptscriptstyle I}\,\overline{\overline{\boldsymbol{I}}} + Z_{\scriptscriptstyle N}\,\overline{\overline{\boldsymbol{N}}} + Z_{\scriptscriptstyle K}\,\overline{\overline{\boldsymbol{K}}} + Z_{\scriptscriptstyle L}\,\overline{\overline{\boldsymbol{L}}}. \tag{2.7}$$

The four dyadic basis can be divided into two groups. $\overline{\overline{\boldsymbol{I}}}$ and $\overline{\overline{\boldsymbol{N}}}$ do not depend on the direction (i.e., the choice of unit vectors, as long as they are orthonormal), and are therefore isotropic. An impedance boundary is termed *isotropic* if its impedance dyadic can be completely expressed in terms of two-dimensional isotropic dyadics. On the contrary, an impedance boundary that has non-zero $\overline{\overline{\boldsymbol{K}}}$ and/or $\overline{\overline{\boldsymbol{L}}}$ components is termed *anisotropic*. An anisotropic impedance means that its response depends on the direction of the applied electric field. This provides more flexibility in the manipulation of the fields, in particular for the control of polarization.

2.1.1 Passivity and losslessness condition

In all practical cases, the impedance must be *passive* and *lossless*. This ensures that it can be physically implemented with printed conductive patches with negligible losses, and without the need for active elements. The meaning of these conditions from an energetic point of view can be investigated starting from the expression for the surface complex power density absorbed by a surface (see App. A.1),

$$\tilde{p} = \boldsymbol{E}_{\text{tan}} \cdot \left[\hat{\boldsymbol{n}}\times(\boldsymbol{H}^{+} - \boldsymbol{H}^{-})\right]^{*} = \boldsymbol{E}_{\text{tan}} \cdot \boldsymbol{J}^{*}. \tag{2.8}$$

This general formula is valid whenever the surface introduces a discontinuity in the magnetic field. The passivity and losslessness (PL) condition requires $\mathrm{Re}\,\tilde{p} = 0$ everywhere on the impedance surface. If the considered impedance is scalar, i.e., $\overline{\overline{\boldsymbol{Z}}} = Z\,\overline{\overline{\boldsymbol{I}}}$, the PL condition reads

$$\begin{aligned} 0 &= \mathrm{Re}\left(\boldsymbol{E}_{\tan} \cdot \boldsymbol{J}^*\right) \\ &= \mathrm{Re}\left(Z\boldsymbol{J} \cdot \boldsymbol{J}^*\right) \\ &= \mathrm{Re}\,Z\left|\boldsymbol{J}\right|^2, \end{aligned} \tag{2.9}$$

which is true only if the impedance is purely reactive, i.e.,

$$\mathrm{Re}\,Z = 0. \tag{2.10}$$

The derivation of the PL condition for a general tensor impedance is much more involved, and is reported in App. B. It requires

$$\mathrm{Re}\,Z_I = \mathrm{Im}\,Z_N = \mathrm{Re}\,Z_K = \mathrm{Re}\,Z_L = 0. \tag{2.11}$$

In view of this, the general form of a passive and lossless impedance tensor is

$$\overline{\overline{\boldsymbol{Z}}} = \mathrm{j}X_I\overline{\overline{\boldsymbol{I}}} + R_N\overline{\overline{\boldsymbol{N}}} + \mathrm{j}X_K\overline{\overline{\boldsymbol{K}}} + \mathrm{j}X_L\overline{\overline{\boldsymbol{L}}}. \tag{2.12}$$

The term R_N implies an instantaneous transfer of energy from one polarization to the other. This is tipically achieved by resonant unit cells that exhibit a bianisotropic behaviour (e.g., split ring or omega particle). However, the use of these geometries complicates the layout design and is outside the scope of this work. Consequently, only unit cells with $R_N = 0$ will be considered.

2.2 Surface Integral Equation formulation

Electromagnetic problems involving metasurfaces can be analyzed with different formulations. In particular, for single-layer metasurfaces, the choice is between the *opaque* and *transparent impedance* formulation. The opaque formulation assumes that the impedance surface is impenetrable, and that fields are only on one side of it, which in turn implies that equivalent currents flow only on that side and

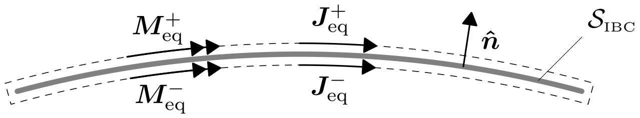

Fig. 2.1 Representation of equivalent currents for the application of the Equivalence Theorem to the case of a metasurface.

the background medium is usually homogeneous. On the contrary, a transparent impedance allows the fields to exist on both sides of the metasurface, with a multilayer background medium. For reasons that will become clear later, the latter formulation is employed in this work. It relies on the *Surface Equivalence Theorem* [31, p. 653], which states that the solution of an electromagnetic problem external to a volume $\mathcal{V}$, containing the sources, remains unchanged if one removes all sources and materials inside the volume and places equivalent sources on the boundary $\partial\mathcal{V}$, defined as

$$\boldsymbol{J}_{\text{eq}} = \hat{\boldsymbol{n}} \times \boldsymbol{H}, \tag{2.13}$$

$$\boldsymbol{M}_{\text{eq}} = -\hat{\boldsymbol{n}} \times \boldsymbol{E}. \tag{2.14}$$

Consider a volume that bounds a metasurface $\mathcal{S}_{\text{IBC}}$ (Fig. 2.1). If the volume collapses to the surface from both sides, the total equivalent currents are given by the sum of the equivalent currents on each side,

$$\boldsymbol{J}_{\text{eq}} = \boldsymbol{J}_{\text{eq}}^{+} + \boldsymbol{J}_{\text{eq}}^{-} = \hat{\boldsymbol{n}} \times \left(\boldsymbol{H}^{+} - \boldsymbol{H}^{-}\right), \tag{2.15}$$

$$\boldsymbol{M}_{\text{eq}} = \boldsymbol{M}_{\text{eq}}^{+} + \boldsymbol{M}_{\text{eq}}^{-} = -\hat{\boldsymbol{n}} \times \left(\boldsymbol{E}^{+} - \boldsymbol{E}^{-}\right), \tag{2.16}$$

where the normal unit vector $\hat{\boldsymbol{n}}$ points toward the $+$ side. A simplifying assumption is that the metasurface introduces discontinuities in the magnetic field only, which is practically the case for metasurfaces realized with printed conducting patches, ensuring $\boldsymbol{M}_{\text{eq}} = \boldsymbol{0}$. With (2.15), (2.1) can be equivalently written as

$$\boldsymbol{E}_{\tan} = \overline{\overline{\boldsymbol{Z}}} \cdot \boldsymbol{J}_{\text{eq}}. \tag{2.17}$$

The tangential electric field can be expressed as the sum of the incident field $\boldsymbol{E}_{\text{inc}}$, radiated by the source in the absence of the metasurface, and of the scattered field $\boldsymbol{E}_{\text{sc}} = \mathcal{L}\boldsymbol{J}_{\text{eq}}$, radiated by the equivalent currents. This allows to express the electromagnetic problem as an *Electric Field Integral Equation* (EFIE-IBC):

$$\left[\boldsymbol{E}_{\text{inc}}(\boldsymbol{r}) + \mathcal{L}\boldsymbol{J}_{\text{eq}}(\boldsymbol{r})\right]_{\tan} = Z(\boldsymbol{r})\boldsymbol{J}_{\text{eq}}(\boldsymbol{r}), \qquad \forall \boldsymbol{r} \in \mathcal{S}_{\text{IBC}}, \tag{2.18}$$

where the unknown is the equivalent electric current $\boldsymbol{J}_{\text{eq}}$; $\mathcal{L}$ is the *Electric Field Integral Operator* (EFIO) defined as

$$\mathcal{L}\boldsymbol{J}(\boldsymbol{r}) = \iint\limits_{\mathcal{S}_{\text{IBC}}} \overline{\overline{\boldsymbol{G}}}^{\text{EJ}}(\boldsymbol{r}, \boldsymbol{r}') \cdot \boldsymbol{J}(\boldsymbol{r}') \, \mathrm{d}S(\boldsymbol{r}'), \tag{2.19}$$

where $\overline{\overline{\boldsymbol{G}}}^{\text{EJ}}$ is the multilayer dyadic Green's function for the background medium [32]. It is noted that here the problem is formulated in terms of a transparent IBC, which requires the Green's function of the layered background medium. This approach has been shown to be significantly more stable than the one involving the opaque version of the IBC [33], which would not need the more complex mentioned Green's function. This approach also allows for a better description of spatial dispersion (the dielectric medium effect is fully described), and eases the passage from the impedance profile $Z(\boldsymbol{r})$ to the design of the individual unit cells (which will not be discussed in this work).

It is also of interest to look at the computation of the field radiated by equivalent currents, as it is usually this field that is the target of the optimization process. If the radiated field specifications are not in the the Fraunhofer (far field) region, radiation is obtained via application of the EFIO, $\mathcal{L}\boldsymbol{J}$. When the field specifications are in the far field (FF), the *radiation operator* $\mathcal{R}$ is given by

$$\mathcal{R}\boldsymbol{J}(\hat{\boldsymbol{r}}) = \frac{\mathrm{j}k_0}{2\pi} \, \overline{\overline{\boldsymbol{G}}}^{\text{FF}}(\hat{\boldsymbol{r}}) \cdot \iint\limits_{\mathcal{S}_{\text{IBC}}} \boldsymbol{J}(\boldsymbol{r}') \, \mathrm{e}^{\mathrm{j}k_0 \hat{\boldsymbol{r}} \cdot \boldsymbol{r}'} \, \mathrm{d}S(\boldsymbol{r}'), \tag{2.20}$$

where the multilayer FF tensor is defined as

$$\overline{\overline{\boldsymbol{G}}}^{\text{FF}}(\hat{\boldsymbol{r}}) = -g^{\text{TM}}(\hat{\boldsymbol{r}}) \, \hat{\boldsymbol{\theta}}\hat{\boldsymbol{\rho}} - \cos\theta \, g^{\text{TE}}(\hat{\boldsymbol{r}}) \, \hat{\boldsymbol{\varphi}}\hat{\boldsymbol{\varphi}}. \tag{2.21}$$

Here, $\hat{\boldsymbol{r}}$, $\hat{\boldsymbol{\theta}}$ and $\hat{\boldsymbol{\varphi}}$ are the unit vectors for a spherical coordinate system, and

$$\hat{\boldsymbol{\rho}} = \cos\phi \, \hat{\boldsymbol{x}} + \sin\phi \, \hat{\boldsymbol{y}}, \tag{2.22}$$

with g^{TM} and g^{TE} being the longitudinal transmission line transfer functions for the TE and TM components [34, p. 1182] and θ and ϕ being the polar and azimuthal angles describing the direction of radiation. Note that in the above the radiated far field has been normalized to $\exp(-\mathrm{j}k_0 r)/r$. A detailed derivation of the far field computation, for the relevant case of single-layer metasurfaces, is reported in App. C.

2.3 Numerical methods

The framework in which the electromagnetic problem has been formulated requires the adoption of numerical methods for its solution. In particular, the discretization follows the usual Method of Moments approach [35]: the surface $\mathcal{S}_{\mathrm{IBC}}$ is represented as a triangular mesh, and the sought current $\boldsymbol{J}$ is approximated as a linear combination of Rao-Wilton-Glisson (RWG) basis functions $\boldsymbol{\Lambda}_n$ [36], defined on the N internal mesh edges,

$$\boldsymbol{J}(\boldsymbol{r}) = \sum_{n=1}^{N} I_n \, \boldsymbol{\Lambda}_n(\boldsymbol{r}). \tag{2.23}$$

The linear system corresponding to the discretized problem is obtained by testing the integral equation (2.18) with the same set of basis functions (Galerkin's method), where testing is carried out by means of the bilinear form

$$\langle \, \boldsymbol{a} \, , \boldsymbol{b} \, \rangle = \iint\limits_{\mathcal{S}_{\mathrm{IBC}}} \boldsymbol{a} \cdot \boldsymbol{b} \, \mathrm{d}S. \tag{2.24}$$

With this discretization, the integral equation (2.18) transforms into the linear system

$$\mathsf{V}_{\mathrm{inc}} + \mathsf{L}\mathsf{I} = \mathsf{Z}\mathsf{I}, \tag{2.25}$$

where the array I collects the RWG basis coefficients I_n, and

$$(\mathsf{L})_{mn} = \langle \, \boldsymbol{\Lambda}_m \, , \mathcal{L}\boldsymbol{\Lambda}_n \, \rangle, \tag{2.26}$$

$$(\mathsf{Z})_{mn} = \langle \, \boldsymbol{\Lambda}_m \, , Z\boldsymbol{\Lambda}_n \, \rangle, \tag{2.27}$$

$$(\mathsf{V}_{\mathrm{inc}})_m = \langle \, \boldsymbol{\Lambda}_m \, , \boldsymbol{E}_{\mathrm{inc}} \, \rangle. \tag{2.28}$$

In presence of an impedance surface, the problem of finding the equivalent electric current coefficients I requires the solution of the linear system

$$\big(\mathbf{Z} - \mathbf{L}\big)\mathsf{I} = \mathsf{V}_{\mathrm{inc}}. \tag{2.29}$$

Enforcement of radiated field specifications involves sampling the field at a discrete set of points; for the case of specifications in the FF region, the sampling points $\hat{\boldsymbol{r}}_j$ are on the unit sphere, and defined by the spherical coordinates (θ_j, ϕ_j). There are two tangential polarizations per sampling point. The radiated field samples at $\hat{\boldsymbol{r}}_j, j = 1, \ldots, N_{\mathrm{f}}$ are assembled in column vectors $\mathsf{E}_\theta, \mathsf{E}_\varphi \in \mathbb{C}^{N_{\mathrm{f}}}$ and, considering the discretization of the current in (2.23), they may be expressed as:

$$\mathsf{E}_\theta = \mathsf{E}_\theta^0 + \mathbf{R}_\theta \mathsf{I}, \tag{2.30}$$

$$\mathsf{E}_\varphi = \mathsf{E}_\varphi^0 + \mathbf{R}_\varphi \mathsf{I}, \tag{2.31}$$

where the fields E_θ^0 and E_φ^0 are those due to the incident field (present in the absence of the metasurface), and the radiation matrices $\mathbf{R}_\theta, \mathbf{R}_\varphi \in \mathbb{C}^{N_{\mathrm{f}} \times N}$ are defined as follows:

$$(\mathbf{R}_\theta)_{jn} = \hat{\boldsymbol{\theta}}_j \cdot \mathcal{R}\boldsymbol{\Lambda}_n(\hat{\boldsymbol{r}}_j), \tag{2.32}$$

$$(\mathbf{R}_\varphi)_{jn} = \hat{\boldsymbol{\varphi}}_j \cdot \mathcal{R}\boldsymbol{\Lambda}_n(\hat{\boldsymbol{r}}_j). \tag{2.33}$$

2.3.1 Fast algorithms

In the design of electrically large antennas, it is necessary to exploit fast numerical algorithms for feasibility reasons. The optimization strategy must take this into account, as will be detailed later. Fast factorizations (e.g., [37]) are related to iterative solutions of the forward problem (2.25); they allow to store only near-field interactions of the EFIO matrix $\mathbf{L}$ (i.e., with $O(N)$ storage requirement) and to perform matrix-vector products $\mathbf{L}\mathsf{I}$ in $O(N \log N)$ complexity (i.e., with $O(N \log N)$ operations per product). Fast factorizations are also required in the computation of the radiated fields in (2.30), (2.31) to avoid computation and storage of the radiation matrices.

In this work, the matrix-vector products involving the EFIO operator are performed by means of a GIFFT algorithm [38, 39]. The computation of the far-field radiation is done by an upward pass of the multilevel fast multipole algorithm (MLFMA) with FFT interpolation on a regular grid of far-field points in the u-v space [37, Sec. 3.5.5].

2.3.2 Conditioning of the EFIE-IBC linear system

The solution of (2.29) requires the use of iterative methods when dealing with electrically large antennas. The convergence properties of these methods strongly depend on the condition number of the matrix representing the linear system. Algebraic preconditioning techniques are available to improve the conditioning of the EFIE-IBC system, but they do not constitute the focus of the present work and will not be discussed further.

For the EFIE-IBC, the average surface impedance Z_{avg} is linked to the condition number of the matrix $(\mathbf{Z} - \mathbf{L})$, as discussed in [33]. In this regard, it is helpful to analyze the behaviour of the condition number as a function of the imaginary part of the average impedance. The results, shown in Fig. 2.2, have been obtained for a square plate of side $4\lambda_0$, with a mesh size of $\lambda_0/10$.

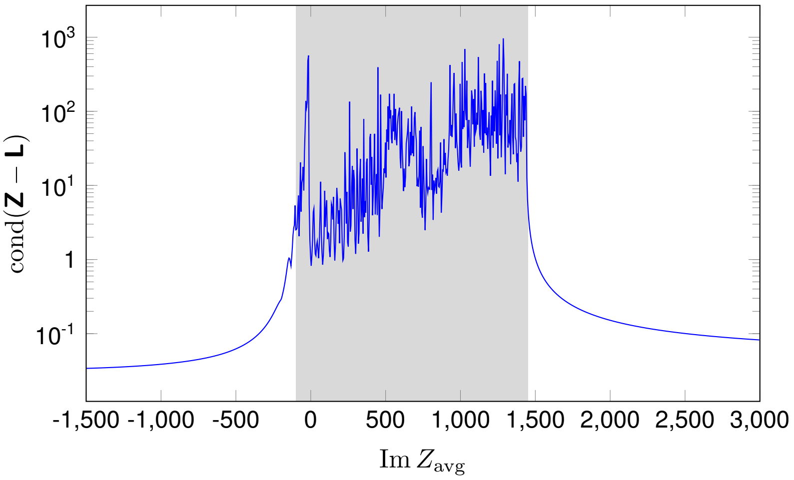

Fig. 2.2 Condition number of the matrix $(\mathbf{Z} - \mathbf{L})$ as a function of the average reactance $\text{Im}\, Z_{\text{avg}}$. The interval of numerical instability (high condition number) is highlighted.

As it is clear, there is a well defined interval of reactance values for which the condition number grows to very large values. This fact must be taken into account when establishing the admissible range for the reactance, in such a way that the resulting average falls outside of the problematic interval.

Chapter 3

Automated Design of Metasurface Antennas

In this chapter, the automated design procedure is described. Starting from the geometry and the source field, the constraints are defined. The design begins with a current-based optimization, which results in an equivalent current distribution satisfying the requirements, followed by the computation of the actual impedance profile. The complete design procedure is outlined in Fig. 3.1. The work presented in this chapter has been submitted for publication and is available as a preprint (see Publications section).

3.1 Geometry and source field

The geometry of the antenna and of the background medium is the starting point of the design. This choice, together with the feed specification, dictates the achievable performances (maximum gain, etc.); therefore, the user should carefully consider these points. The focus will be on the design of planar, single-layer metasurfaces on a dielectric substrate, excited by a surface wave (Fig. 3.2).

The proposed procedure is numerical and as such requires the discretization of the solution domain; owing to the surface integral formulation presented in Sec. 2.2, only the impedance surface S_{IBC} needs to be meshed. This is done by considering a tessellation composed of N_{c} triangular cells $\mathcal{S}_i$ (see Fig. 3.3 for an example).

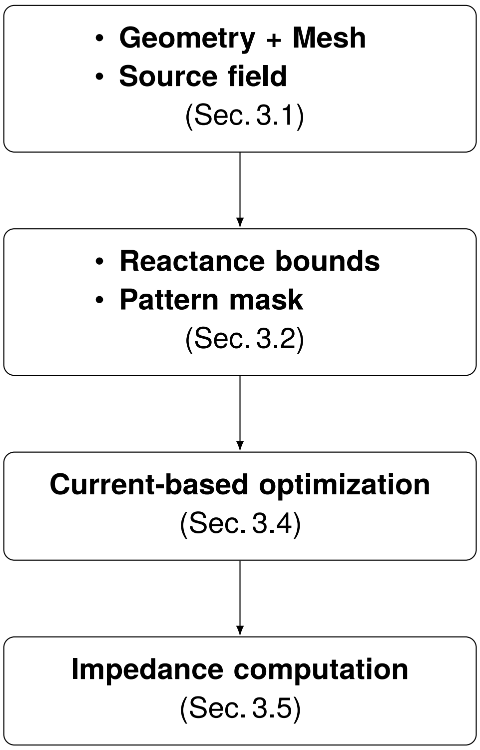

Fig. 3.1 Flowchart of the complete design procedure

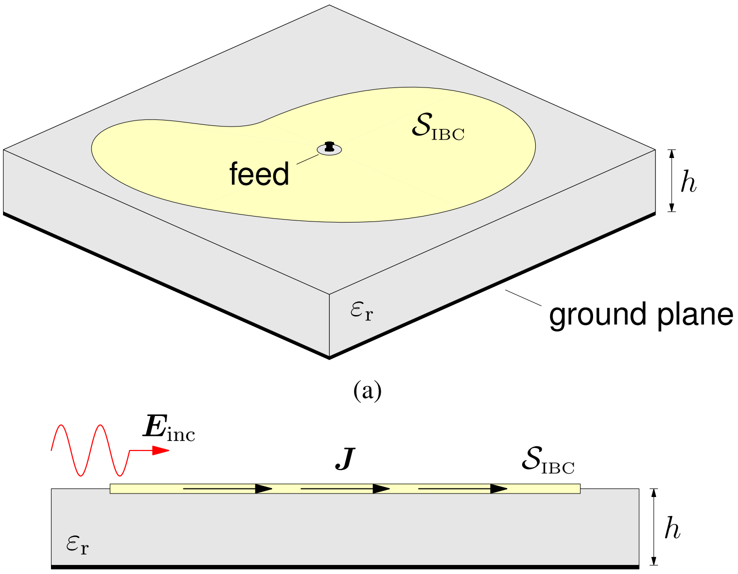

(a)

(b)

Fig. 3.2 Example of geometry for the considered metasurface antenna layout: (a) 3D view, for the case in which the source of the incident field is on-surface, (b) cross section with the equivalent currents $\boldsymbol{J}$.

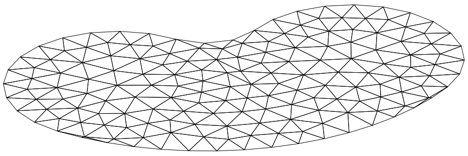

Fig. 3.3 Example of mesh employed in the design. Only the impedance surface is discretized, and the effect of the grounded substrate (background medium) is taken into account by the multilayer Green's function.

The current is approximated as a linear combination of N RWG basis functions (as detailed in Sec. 2.3).

The source field defines how the antenna is excited. The feed can be on the surface level, exciting a guided surface wave in the dielectric substrate, or external, illuminating the aperture from a distance. The case of an on-surface feed is more susceptible to the reflection of power at the input, a problem which must be addressed in the design procedure. In all cases, one needs to estimate the *input power* of the source field, as needed in the definition of the optimization instance (the calculations for the particular case of a vertical pin exciting a surface wave are reported in App. A.4).

It must be stressed that the setup of the design procedure is not restricted to planar, single-layer geometries in a multilayer environment, but can be applied in general to arbitrarily shaped surfaces in heterogeneous background media. However, as the algorithm requires the formulation of a surface integral equation, the computation of the required matrices and of the incident field can become cumbersome. Moreover, the availability of fast methods for the computation of matrix-vector products is limited in the case of arbitrary geometries.

3.2 Constraint definition

The aim of the design procedure is to obtain an impedance profile that is physically and technologically realizable, and that radiates a field pattern obeying the field specifications when it interacts with the source field. Therefore, it is important to examine what these constraints mean and how they can be enforced.

3.2.1 Realizability

To obtain a physically realizable impedance, the metasurface must be locally *passive* and *lossless*, meaning that for each point on the surface, the active power should neither be dissipated, nor provided. This translates in the following condition for the impedance:

$$\operatorname{Re} Z(\boldsymbol{r}) = 0, \quad \forall \boldsymbol{r} \in S_{\mathrm{IBC}}. \tag{3.1}$$

Moreover, the range of realizable reactance (imaginary part of the impedance) values depends on the chosen unit cell type, employed technology and practical (e.g., size) limits; these bounds must be taken into account in the design process, i.e.,

$$X_{\mathrm{L}} \leq \operatorname{Im} Z(\boldsymbol{r}) \leq X_{\mathrm{U}}, \quad \forall \boldsymbol{r} \in S_{\mathrm{IBC}}. \tag{3.2}$$

These two requirements ensure that the metasurface can be implemented by means of the chosen unit cells. Numerical considerations can also influence the range of acceptable reactance values, as analyzed in Sec. 2.3.2, since the full design cycle includes a validation process in which the optimized impedance profile is used in the solution of the forward problem. In fact, if the resulting linear system (2.29) is badly conditioned, noise in the solution can prevent convergence of the iterative solver, even if the physical design is satisfactory.

3.2.2 Field specifications

The radiated field specifications may be both in the far field region or closer; in this work, the focus is on far field specifications, as these are the most common ones in the design of antennas. They are expressed in terms of the field amplitude (power density); both the total (“t”) amplitude and the co- (“co”) and cross-polarized (“x”) components are considered:

$$F^{\mathrm{co}}(\hat{\boldsymbol{r}}, \mathsf{I}) = \left|\boldsymbol{E}(\hat{\boldsymbol{r}}, \mathsf{I}) \cdot \hat{\boldsymbol{p}}^{*}(\hat{\boldsymbol{r}})\right|^{2}, \tag{3.3}$$

$$F^{\mathrm{cx}}(\hat{\boldsymbol{r}}, \mathsf{I}) = \left|\boldsymbol{E}(\hat{\boldsymbol{r}}, \mathsf{I}) \cdot \hat{\boldsymbol{q}}^{*}(\hat{\boldsymbol{r}})\right|^{2}, \tag{3.4}$$

$$F^{\mathrm{tot}}(\hat{\boldsymbol{r}}, \mathsf{I}) = \left|\boldsymbol{E}(\hat{\boldsymbol{r}}, \mathsf{I})\right|^{2}. \tag{3.5}$$

where $\hat{\boldsymbol{p}}$ and $\hat{\boldsymbol{q}} = \hat{\boldsymbol{r}} \times \hat{\boldsymbol{p}}^*$ are the co- and cross-polarization unit vectors, respectively. Tab. 3.1 lists the choice of unit vectors for the most common types of polarization. The definitions for linear polarization are taken from [40].

Field specifications are of the *mask type*, i.e., defined in general via inequalities of the kind

$$M_{\mathrm{L}}(\hat{\boldsymbol{r}}, \mathsf{I}) \leq F(\hat{\boldsymbol{r}}, \mathsf{I}) \leq M_{\mathrm{U}}(\hat{\boldsymbol{r}}, \mathsf{I}), \tag{3.6}$$

for each considered far field direction $\hat{\boldsymbol{r}}$. The mask values must typically be defined in terms of directivity or gain. Observe that pattern-matching, i.e., fitting a specific (amplitude) field pattern, is a special case of the above, i.e.,

$$F(\hat{\boldsymbol{r}}, \mathsf{I}) = M(\hat{\boldsymbol{r}}, \mathsf{I}) \qquad \longrightarrow \qquad M(\hat{\boldsymbol{r}}, \mathsf{I}) \leq F(\hat{\boldsymbol{r}}, \mathsf{I}) \leq M(\hat{\boldsymbol{r}}, \mathsf{I}), \tag{3.7}$$

with $M_{\mathrm{L}} = M_{\mathrm{U}} = M$, that is easier to address as it does not require inequalities.

Specification of an *absolute* lower bound to the main lobe (co-polarization) may be a requirement in some designs; on the other hand, sidelobe and cross-polarization levels have to be defined *relative* to the *actual* level in the main beam. This way, the relative levels comply with the specifications even when the main lobe requirement is not met by the solution. This can be made specific as follows. Let $\hat{\boldsymbol{r}}_0$ be the specified beam pointing direction; the reference main-lobe level F_{ref} is defined as the average over a small angular region Ω_0 around the maximum radiation direction $\hat{\boldsymbol{r}}_0$,

$$F_{\mathrm{ref}}(\mathsf{I}) = \frac{1}{\Omega_0} \iint\limits_{\Omega_0} F^{\mathrm{co}}(\hat{\boldsymbol{r}}, \mathsf{I})\, \mathrm{d}\Omega(\hat{\boldsymbol{r}}). \tag{3.8}$$

The above is an extension of the amplitude in the specified beam direction, $F^{\mathrm{co}}(\hat{\boldsymbol{r}}_0)$, to which it reduces in a trivial manner; use of this averaged level typically makes the optimization instance more robust especially in shaped-beam design instances (e.g. flat-top). Given a lower bound M_0 for the reference level, the only absolute requirement will thus be

$$F_{\mathrm{ref}}(\mathsf{I}) \geq M_0, \tag{3.9}$$

with all others becoming relative to F_{ref}.

It is convenient to break down the specifications in the main lobe (ML) region Ω_{ML} and in the side-lobe (SL) region Ω_{SL}, as they are functionally different. Overall,

Table 3.1 Choice of unit vectors for the most common polarization types.

Polarization	Co-pol $\hat{\boldsymbol{p}}$	Cross-pol $\hat{\boldsymbol{q}}$
Linear (Ludwig I)	$\sin\theta\sin\varphi\,\hat{\boldsymbol{r}} + \cos\theta\sin\varphi\,\hat{\boldsymbol{\theta}} + \cos\varphi\,\hat{\boldsymbol{\varphi}}$	$\sin\theta\cos\varphi\,\hat{\boldsymbol{r}} + \cos\theta\cos\varphi\,\hat{\boldsymbol{\theta}} - \sin\varphi\,\hat{\boldsymbol{\varphi}}$
Linear (Ludwig II)	$\dfrac{\sin\varphi\cos\theta\,\hat{\boldsymbol{\theta}} + \cos\varphi\,\hat{\boldsymbol{\varphi}}}{\sqrt{1-\sin^2\theta\sin^2\varphi}}$	$\dfrac{\cos\varphi\,\hat{\boldsymbol{\theta}} - \sin\varphi\cos\theta\,\hat{\boldsymbol{\varphi}}}{\sqrt{1-\sin^2\theta\sin^2\varphi}}$
Circular (CW)	$\dfrac{(\cos\theta\sin\varphi + \mathrm{j}\cos\varphi)\,\hat{\boldsymbol{\theta}} + (\cos\varphi - \mathrm{j}\cos\theta\sin\varphi)\,\hat{\boldsymbol{\varphi}}}{\sqrt{2(1-\sin^2\theta\sin^2\varphi)}}$	$\dfrac{(\cos\theta\sin\varphi - \mathrm{j}\cos\varphi)\,\hat{\boldsymbol{\theta}} + (\cos\varphi + \mathrm{j}\cos\theta\sin\varphi)\,\hat{\boldsymbol{\varphi}}}{\sqrt{2(1-\sin^2\theta\sin^2\varphi)}}$
Circular (CCW)	$\dfrac{(\cos\theta\sin\varphi - \mathrm{j}\cos\varphi)\,\hat{\boldsymbol{\theta}} + (\cos\varphi + \mathrm{j}\cos\theta\sin\varphi)\,\hat{\boldsymbol{\varphi}}}{\sqrt{2(1-\sin^2\theta\sin^2\varphi)}}$	$\dfrac{(\cos\theta\sin\varphi + \mathrm{j}\cos\varphi)\,\hat{\boldsymbol{\theta}} + (\cos\varphi - \mathrm{j}\cos\theta\sin\varphi)\,\hat{\boldsymbol{\varphi}}}{\sqrt{2(1-\sin^2\theta\sin^2\varphi)}}$

this results in the following set of specifications:

$$M_{\mathrm{L}}^{\mathrm{co}}(\hat{\boldsymbol{r}},\mathsf{I}) \le F^{\mathrm{co}}(\hat{\boldsymbol{r}},\mathsf{I}) \le M_{\mathrm{U}}^{\mathrm{co}}(\hat{\boldsymbol{r}},\mathsf{I}), \quad \hat{\boldsymbol{r}} \in \Omega_{\mathrm{ML}}, \tag{3.10}$$

where

$$M_{\mathrm{L}}^{\mathrm{co}}(\hat{\boldsymbol{r}},\mathsf{I}) = \mu_{\mathrm{L}}^{\mathrm{co}}(\hat{\boldsymbol{r}})\, F_{\mathrm{ref}}(\mathsf{I}), \tag{3.11}$$

$$M_{\mathrm{U}}^{\mathrm{co}}(\hat{\boldsymbol{r}},\mathsf{I}) = \mu_{\mathrm{U}}^{\mathrm{co}}(\hat{\boldsymbol{r}})\, F_{\mathrm{ref}}(\mathsf{I}), \tag{3.12}$$

with the upper requirement being absent in pencil-beam type specifications. The parameters $\mu_{\mathrm{L}}^{\mathrm{co}}$ and $\mu_{\mathrm{U}}^{\mathrm{co}}$ represent the lower and upper relative levels for the co-polarization component in the main beam. For the cross-polarization and total magnitude, the masks take the form

$$F^{\mathrm{cx}}(\hat{\boldsymbol{r}},\mathsf{I}) \le M_{\mathrm{U}}^{\mathrm{cx}}(\hat{\boldsymbol{r}},\mathsf{I}), \quad \hat{\boldsymbol{r}} \in \Omega_{\mathrm{ML}}, \tag{3.13}$$

$$F^{\mathrm{tot}}(\hat{\boldsymbol{r}},\mathsf{I}) \le M_{\mathrm{U}}^{\mathrm{tot}}(\hat{\boldsymbol{r}},\mathsf{I}), \quad \hat{\boldsymbol{r}} \in \Omega_{\mathrm{SL}}, \tag{3.14}$$

where

$$M_{\mathrm{U}}^{\mathrm{cx}}(\hat{\boldsymbol{r}},\mathsf{I}) = \sigma^{\mathrm{cx}}(\hat{\boldsymbol{r}})\, F_{\mathrm{ref}}(\mathsf{I}), \tag{3.15}$$

$$M_{\mathrm{U}}^{\mathrm{tot}}(\hat{\boldsymbol{r}},\mathsf{I}) = \sigma^{\mathrm{SL}}(\hat{\boldsymbol{r}})\, F_{\mathrm{ref}}(\mathsf{I}). \tag{3.16}$$

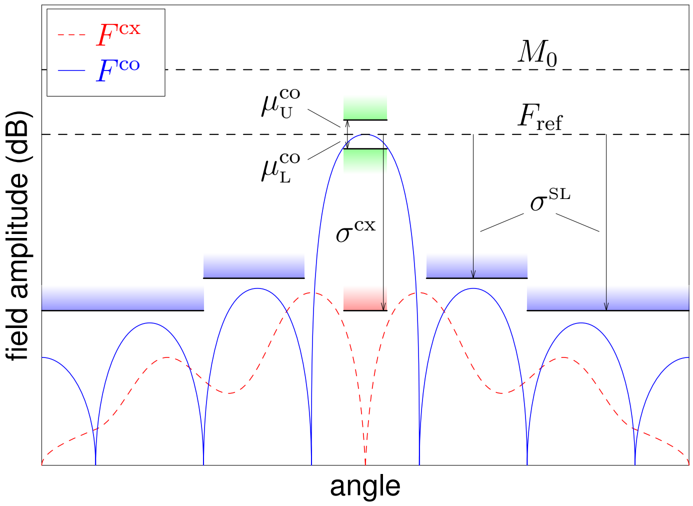

Fig. 3.4 Example of far-field specifications: objective level M_0, reference level F_{ref}, main lobe co-pol masks $M_{\mathrm{L}}^{\mathrm{co}}$, $M_{\mathrm{U}}^{\mathrm{co}}$ (green), cross-pol mask $M_{\mathrm{U}}^{\mathrm{cx}}$ (red) and side lobes mask $M_{\mathrm{U}}^{\mathrm{tot}}$ (blue). Vertical arrows indicate relative levels.

The parameter σ^{cx} defines the cross-polarization ratio in the main lobe, while σ^{SL} represents the desired relative level for the side lobes. An example of mask-type constraints, with all the parameters, is depicted in Fig. 3.4.

3.3 Alternate Projection Algorithm

In the search for an effective algorithm for the design of metasurfaces obeying the realizability constraints and the field specifications, the initial focus was on an *Alternate Projection Algorithm*, inspired by well-known algorithms for pattern synthesis [41–43], and adapted to include the constraints on the impedance. This attempt resulted in the algorithm listed in Algorithm 1 [44]. Starting from the reactance bounds and the field specifications, it tries to find a current that radiates a field obeying the requirements, as well as being consistent with the EFIE-IBC equation for a feasible choice of the impedance. It does that by alternatively projecting the current on the set corresponding to feasible impedances, and on that of currents radiating a feasible field, hence its name.

The impedance on each cell is computed as the ratio of the local power to the magnitude squared of the current (averaged over the cell surface),

$$Z = \frac{\iint_S \boldsymbol{E} \cdot \boldsymbol{J}^* \, \mathrm{d}S}{\iint_S |\boldsymbol{J}|^2 \, \mathrm{d}S}, \tag{3.17}$$

as will be detailed in Sec. 3.5, and is easily projected in the feasible set by setting the real part to zero and clipping the imaginary part if it goes out of bounds. The *impedance projection operator* is defined as

$$\mathcal{P}_Z(Z) = \begin{cases} \mathrm{j}\,\mathrm{Im}\,Z, & \text{if } X_{\mathrm{L}} \leq \mathrm{Im}\,Z \leq X_{\mathrm{U}} \\ \mathrm{j}X_{\mathrm{L}}, & \text{if } \mathrm{Im}\,Z < X_{\mathrm{L}} \\ \mathrm{j}X_{\mathrm{U}}, & \text{if } \mathrm{Im}\,Z > X_{\mathrm{U}} \end{cases} \tag{3.18}$$

Then, a new current is obtained from the solution of the EFIE-IBC (2.29), and the radiated field is computed. The radiated field is then projected inside the mask specifications by clipping the values that are out bounds, by means of the *field* *projection operator*,

$$\mathcal{P}_E(\boldsymbol{E}) = \begin{cases} \boldsymbol{E}, & \text{if } M_\mathrm{L} \leq |\boldsymbol{E}|^2 \leq M_\mathrm{U} \\ \boldsymbol{E}\sqrt{\dfrac{M_\mathrm{L}}{|\boldsymbol{E}|^2}}, & \text{if } |\boldsymbol{E}|^2 < M_\mathrm{L} \\ \boldsymbol{E}\sqrt{\dfrac{M_\mathrm{U}}{|\boldsymbol{E}|^2}}, & \text{if } |\boldsymbol{E}|^2 > M_\mathrm{U} \end{cases} \tag{3.19}$$

The next iterate for the current is obtained by finding the one that radiates a field that best approximates the projected one (least-squares inversion), i.e.,

$$\mathsf{I}_{k+1} = \underset{\mathsf{I}\in\mathbb{C}^N}{\arg\min} \left\|\mathsf{E} - \mathbf{R}\mathsf{I}\right\|^2 . \tag{3.20}$$

Finally, the *relative variation* of the current is computed,

$$\varepsilon_\mathsf{I} = \frac{\|\mathsf{I}_{k+1} - \mathsf{I}_k\|}{(\|\mathsf{I}_{k+1}\| + \|\mathsf{I}_k\|)/2}, \tag{3.21}$$

and its value is compared with the threshold τ that defines the minimum variation allowed. If the relative variation is less than τ, it means that the two currents are equal within the tolerance, which in turn implies that the current complies with all the requirements and the process has reached convergence.

Algorithm 1 Alternate Projection Algorithm for the design of Metasurface Antennas.

```
Input: reactance bounds, field specs
Output: $Z$
  while $k = 0, \dots, K_\mathrm{max} - 1$ and $\varepsilon_\mathsf{I} < \tau$ do
      Compute $Z$ with (3.128)
      Project $Z$ with (3.18)
      Solve $(\mathbf{Z} - \mathbf{L})\mathsf{I}_k = \mathsf{V}_\mathrm{inc}$
      Compute radiated field $\mathsf{E} = \mathbf{R}\mathsf{I}_k$
      Project radiated field with (3.19)
      Compute $\mathsf{I}_{k+1}$ with (3.20)
      Compute $\varepsilon_\mathsf{I}$ with (3.21)
      $k \leftarrow k + 1$
  end while
```

This algorithm guarantees that the impedance and the current are always consistent with the EFIE-IBC. However, this is obtained at the expense of solving the resulting linear system (2.29), and the inverse-source problem (3.20) at each iteration. As a result, the computational complexity becomes prohibitively large already for medium-sized antennas, even if fast algorithms are used. Note that this complexity is comparable to that of analogous approaches, e.g., [10]; however, keeping in mind that the target was the 3D design of large surfaces, the alternate projection approach was not pursued further. The focus has then shifted on a different formulation, presented in the next section, which overcomes this drawback.

3.4 Current-based Optimization Algorithm

In this section, the proposed approach for the design of metasurface antennas is detailed. The outcome of the design process must be the spatial distribution of the surface impedance; however, the optimization is formulated in such a way that it involves *only* the equivalent current—not the impedance. On exit, the process yields the optimized current, from which a corresponding impedance is obtained (as described in Sec. 3.5). This current-based design process avoids the solution of the forward problem (2.25) at each step, with obvious advantages in terms of numerical complexity. Of course, this is possible only if the current being sought-for can be constrained to correspond to a passive and lossless surface, in addition to radiating a field that satisfies the related requirements. Moreover, the reactance associated to the current must be bounded by practical realizability limits—again, without computing this reactance explicitly during the process.

The "optimal" current is obtained as the solution of an *unconstrained* optimization problem, where the fitness is expressed in terms of cost functionals to be minimized:

$$\mathsf{I}^\star = \arg\min_{\mathsf{I}\in\mathbb{C}^N} f(\mathsf{I}), \tag{3.22}$$

where the overall functional f is composed of a term f_{rlz} that expresses the compliance with realizability constraints, and a term f_{rad} that quantifies the fitness of the radiated field,

$$f(\mathsf{I}) = f_{\text{rlz}}(\mathsf{I}) + f_{\text{rad}}(\mathsf{I}). \tag{3.23}$$

As explained above, it is crucial to express these terms as functions of the current *only*; this point will be addressed in Secs. 3.4.1 and 3.4.2.

An important observation is that requirements involving inequalities, like those of field masks in (3.6) or reactance bounds (3.2), are conveniently expressed as quantities to be minimized by means of the ramp function

$$\mathrm{r}(x) = \max(x, 0), \tag{3.24}$$

with which a condition of the type $a \leq b$ becomes $\mathrm{r}(a - b) = 0$.

For the class of constraints of relevance here, the associated minimization instance is non-convex. Hence, strategies to overcome the non-convexity shortcomings, and in particular local trappings, are very important. Inspired by [12], the choice is to resort to functionals that are of polynomial type in the current coefficients, in particular fourth-degree polynomials, with added rectification (via the ramp function) where needed. The most general expression for the functional takes the form

$$\begin{aligned} f(\mathsf{I}) &= \sum_d q_d(\mathsf{I})\, s_d(\mathsf{I}) + \sum_d \mathrm{r}^2(t_d(\mathsf{I})) \\ &= \big(\mathsf{q}(\mathsf{I})\big)^{\mathsf{T}} \mathsf{s}(\mathsf{I}) + \mathrm{r}\big(\mathsf{t}(\mathsf{I})\big)^{\mathsf{T}} \mathrm{r}\big(\mathsf{t}(\mathsf{I})\big), \end{aligned} \tag{3.25}$$

with

$$\mathsf{q}(\mathsf{I}) = [\cdots q_d(\mathsf{I}) \cdots]^{\mathsf{T}}, \tag{3.26}$$

$$\mathsf{s}(\mathsf{I}) = [\cdots s_d(\mathsf{I}) \cdots]^{\mathsf{T}}, \tag{3.27}$$

$$\mathsf{t}(\mathsf{I}) = [\cdots t_d(\mathsf{I}) \cdots]^{\mathsf{T}}. \tag{3.28}$$

The function $\mathrm{r}^2(x) = \max(x, 0)^2$ is continuous with continuous first derivative, while q_d, s_d and t_d are multivariable quadratic functions of the current coefficients, i.e., of the form

$$q_d(\mathsf{I}) = \Phi\big(\mathsf{I}^{\mathsf{H}} \mathbf{A}_d \mathsf{I} + \mathsf{I}^{\mathsf{H}} \mathsf{b}_d + c_d\big), \qquad \Phi = \mathrm{Re} \text{ or } \mathrm{Im}, \tag{3.29}$$

where $\mathbf{A}_d \in \mathbb{C}^{N \times N}$ are positive definite matrices, $\mathsf{b}_d \in \mathbb{C}^N$ are column vectors and $c_d \in \mathbb{C}$ are constants. The advantage of this choice is apparent: for even-degree polynomials, the functional is bounded below, and goes to $+\infty$ as $\|\mathsf{I}\| \longrightarrow +\infty$. Moreover, a polynomial of degree four limits the number of possible local minima, while still allowing enough flexibility in the definition of the functional. Finally, in the adopted formulation the matrices $\mathbf{A}_d$ are chosen in such a way that the computation of each term of (3.25) can be accelerated (either A_d is sparse or the matrix-vector product $\mathsf{A}_d\mathsf{I}$ can be computed with fast algorithms).

For the minimization of (3.22), a *non-linear conjugate gradient* algorithm [45, p. 121] is employed (Algorithm 2). Given the large size of the problem, the numerical cost of computing the functional *and* its gradient at each iteration is an issue of paramount importance. In particular, all operations corresponding to computing the near- or far field of a given current can be performed with the so-called "fast factorizations" mentioned in Sec. 2.3.1, with $O(N)$ memory requirements and $O(N \log N)$ complexity. The proposed approach, as will be seen in Sec. 3.4.3, is able to fully exploit these methods for the computation of the functional and of its gradient.

Algorithm 2 Non-linear conjugate gradient algorithm.

```
Input: $\mathsf{I}_0$
Output: $\mathsf{I}^\star$
  Compute $\nabla f(\mathsf{I}_0)$
  $\mathsf{p}_0 \leftarrow -\nabla f(\mathsf{I}_0)$
  for $k = 0, \ldots, K_{\max} - 1$ do
      Compute $\alpha_k$ by minimizing $f(\mathsf{I}_k + \alpha_k \mathsf{p}_k)$
      $\mathsf{I}_{k+1} \leftarrow \mathsf{I}_k + \alpha_k \mathsf{p}_k$
      Compute $\nabla f(\mathsf{I}_{k+1})$
      Compute $\beta_k$
      $\mathsf{p}_{k+1} \leftarrow -\nabla f(\mathsf{I}_{k+1}) + \beta_k \mathsf{p}_k$
  end for
  $\mathsf{I}^\star \leftarrow \mathsf{I}_{K_{\max}}$
```

The other relevant step is the *line search* that must be carried out at each step of the iterative process. This is a deceivingly simple task, as it involves only a one-dimensional minimization along the search direction, which in principle can be performed with a variety of standard approaches. However, as well known in the literature, the difficult part is in finding the *interval* in which this search must be carried out. The devised polynomial approach will allow to perform this in an analytical (possibly iterative), definite manner (Sec. 3.4.4).

Finally, it is possible to enforce a smoothing of the resulting current prior to the impedance computation; this can be done with a variety of standard approaches (see, e.g., [14]). However, the choice has been to avoid this step, in order to check the intrinsic degree of regularity of the solution, without introducing additional parameters in the process.

3.4.1 Enforcement of realizability constraints

As discussed, realizability requires local passivity and absence of losses, as well as bounds on the impedance values. Passivity and losslessness can be expressed directly in terms of the (local) active power density; the magnitude of the reactance, instead, can be expressed in terms of (local) stored energy density. Hence, all realizability constraints can be cast in terms of power densities; this allows to express them as functions of the current only, and also to satisfy the requirement of being of polynomial nature.

The discussion starts with the definition of the power density absorbed by a surface (see App. A.1),

$$\tilde{p}(\boldsymbol{r}) = \boldsymbol{E} \cdot \boldsymbol{J}^*, \tag{3.30}$$

that is related to the local impedance, via the IBC (2.1), as

$$\tilde{p}(\boldsymbol{r}) = Z \left|\boldsymbol{J}\right|^2 = \operatorname{Re} Z \left|\boldsymbol{J}\right|^2 + \mathrm{j} \operatorname{Im} Z \left|\boldsymbol{J}\right|^2 . \tag{3.31}$$

The requirement for passivity and losslessness imposes that $P = 0$, i.e.,

$$\operatorname{Re}\left(\boldsymbol{E} \cdot \boldsymbol{J}^*\right) = 0. \tag{3.32}$$

It is important to note that, in order to preserve global passivity, one needs to enforce (3.32) locally in an explicit manner [12] (otherwise, one could have zero global dissipated power but with active terms with $P < 0$ compensating losses). This will be achieved by minimizing the square of the local power density, P^2, thus preserving the polynomial nature of its definition.

The requirement (3.2) is closely related to the stored (reactive) energy density. In fact, looking at the imaginary part of (3.31), the bounds in (3.2) imply

$$X_{\mathrm{L}} \left|\boldsymbol{J}\right|^2 \leq \operatorname{Im}\left(\boldsymbol{E} \cdot \boldsymbol{J}^*\right) \leq X_{\mathrm{U}} \left|\boldsymbol{J}\right|^2 . \tag{3.33}$$

It is important to recall that inequality conditions like (3.33) can be expressed in terms of the ramp function; however, this function does not have a continuous

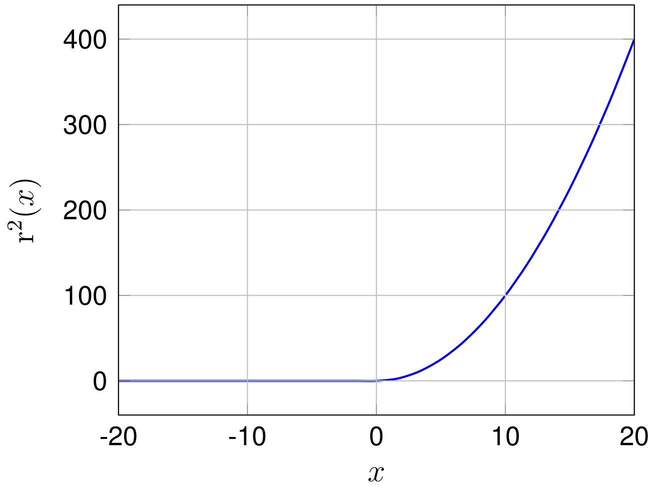

Fig. 3.5 Squared ramp function $\mathrm{r}^2(x) = \max(x, 0)^2$.

derivative. This problem can be overcome by using the *squared ramp function* $\mathrm{r}^2(x) = \max(x, 0)^2$, which is a continuous function with continuous derivative (Fig. 3.5). This allows the use of inequalities in the functional gradients at the only expense of having *piecewise* polynomial functions, but everywhere continuous and differentiable.

As a final remark, since the impedance does not appear in the conditions above, there is no guarantee that the obtained current is such as to correspond to a scalar impedance; if required by the design constraints, this condition must be enforced explicitly. In presence of a scalar impedance, the current and the electric field have the same direction (in the complex sense). From Schwarz's inequality, it follows that the (complex) inner product of two parallel vectors is equal to the product of their magnitudes, giving the *scalarity condition*

$$|\boldsymbol{E} \cdot \boldsymbol{J}^*| = |\boldsymbol{E}|\,|\boldsymbol{J}|\,. \tag{3.34}$$

All the above conditions must hold locally everywhere on the surface; in accordance with the cell-based spatial discretization scheme, they will be enforced in the average sense over each triangular cell. In particular, the local power (3.30) for each cell is defined as the integral of the power density over the domain of the cell,

$$\tilde{p}_i = \langle\, \boldsymbol{E}\,, \mathbb{I}_{\mathcal{S}_i} \boldsymbol{J}^* \,\rangle = \iint\limits_{\mathcal{S}_i} \boldsymbol{E} \cdot \boldsymbol{J}^* \,\mathrm{d}S, \tag{3.35}$$

where

$$\mathbb{I}_{\mathcal{D}}(\boldsymbol{r}) = \begin{cases} 1, & \text{if } \boldsymbol{r} \in \mathcal{D} \\ 0, & \text{elsewhere} \end{cases} \tag{3.36}$$

is the indicator function of domain $\mathcal{D}$.

With the above stipulations, the conditions of passivity and losslessness (“act”), of the reactance bounds (“rct”), and of scalarity (“scal”) result in a cost function that is the sum of three contribution over the total number of triangular cells N_c:

$$f_\mathrm{rlz}(\mathsf{I}) = w_\mathrm{act} \sum_{i=1}^{N_\mathrm{c}} \rho_i^\mathrm{act}(\mathsf{I}) + w_\mathrm{rct} \sum_{i=1}^{N_\mathrm{c}} \rho_i^\mathrm{rct}(\mathsf{I}) + w_\mathrm{scal} \sum_{i=1}^{N_\mathrm{c}} \rho_i^\mathrm{scal}(\mathsf{I}). \tag{3.37}$$

The weights w_act, w_rct and w_scal have to be assigned a priori, like in all optimization problems of multi-objective nature. The cell-wise terms are defined as follows:

$$\rho_i^\mathrm{act}(\mathsf{I}) = P_i^{\,2}(\mathsf{I}), \tag{3.38}$$

$$\rho_i^\mathrm{rct}(\mathsf{I}) = \mathrm{r}^2\big(X_\mathrm{L}\mathcal{J}_i(\mathsf{I}) - Q_i(\mathsf{I})\big) + \mathrm{r}^2\big(Q_i(\mathsf{I}) - X_\mathrm{U}\mathcal{J}_i(\mathsf{I})\big), \tag{3.39}$$

$$\rho_i^\mathrm{scal}(\mathsf{I}) = \mathcal{E}_i(\mathsf{I})\,\mathcal{J}_i(\mathsf{I}) - \big(P_i^{\,2}(\mathsf{I}) + Q_i^{\,2}(\mathsf{I})\big)\,, \tag{3.40}$$

where the individual terms are conveniently written in the form (3.29):

$$\begin{aligned} P_i(\mathsf{I}) &= \mathrm{Re} \iint\limits_{\mathcal{S}_i} \boldsymbol{E} \cdot \boldsymbol{J}^* \,\mathrm{d}S = \mathrm{Re}\,(\mathsf{I}^\mathsf{H}\boldsymbol{\Gamma}_i\mathsf{V}) \\ &= \mathrm{Re}\,\big(\mathsf{I}^\mathsf{H}(\boldsymbol{\Gamma}_i\boldsymbol{\mathsf{K}})\mathsf{I} + \mathsf{I}^\mathsf{H}(\boldsymbol{\Gamma}_i\mathsf{V}'_\mathrm{inc})\big), \end{aligned} \tag{3.41}$$

$$\begin{aligned} Q_i(\mathsf{I}) &= \mathrm{Im} \iint\limits_{\mathcal{S}_i} \boldsymbol{E} \cdot \boldsymbol{J}^* \,\mathrm{d}S = \mathrm{Im}\,(\mathsf{I}^\mathsf{H}\boldsymbol{\Gamma}_i\mathsf{V}) \\ &= \mathrm{Im}\,\big(\mathsf{I}^\mathsf{H}(\boldsymbol{\Gamma}_i\boldsymbol{\mathsf{K}})\mathsf{I} + \mathsf{I}^\mathsf{H}(\boldsymbol{\Gamma}_i\mathsf{V}'_\mathrm{inc})\big), \end{aligned} \tag{3.42}$$

$$\mathcal{J}_i(\mathsf{I}) = \iint\limits_{\mathcal{S}_i} |\boldsymbol{J}|^2 \,\mathrm{d}S = \mathsf{I}^\mathsf{H}\boldsymbol{\Gamma}_i\mathsf{I}, \tag{3.43}$$

$$\begin{aligned} \mathcal{E}_i(\mathsf{I}) &= \iint\limits_{\mathcal{S}_i} |\boldsymbol{E}|^2 \,\mathrm{d}S = \mathsf{V}^\mathsf{H}\boldsymbol{\Gamma}_i\mathsf{V} \\ &= \mathrm{Re}\,\big(\mathsf{I}^\mathsf{H}(\boldsymbol{\mathsf{K}}^\mathsf{H}\boldsymbol{\Gamma}_i\boldsymbol{\mathsf{K}})\mathsf{I} + 2\mathsf{I}^\mathsf{H}(\boldsymbol{\mathsf{K}}^\mathsf{H}\boldsymbol{\Gamma}_i\mathsf{V}'_\mathrm{inc}) + \mathsf{V}'^\mathsf{H}_\mathrm{inc}\boldsymbol{\Gamma}_i\mathsf{V}'_\mathrm{inc}\big). \end{aligned} \tag{3.44}$$

For convenience of notation, the following quantities have been introduced:

$$\mathsf{V}'_{\text{inc}} = \mathbf{G}^{-1}\mathsf{V}_{\text{inc}}, \tag{3.45}$$

$$\mathbf{K} = \mathbf{G}^{-1}\mathbf{L}, \tag{3.46}$$

$$\mathsf{V} = \mathbf{G}^{-1}(\mathsf{V}_{\text{inc}} + \mathbf{L}\mathsf{I}) = \mathsf{V}'_{\text{inc}} + \mathbf{K}\mathsf{I}. \tag{3.47}$$

Here, $\mathbf{G} \in \mathbb{R}^{N\times N}$ is the Gram matrix of the RWG basis functions,

$$(\mathbf{G})_{mn} = \iint\limits_{\mathcal{S}_{\text{IBC}}} \boldsymbol{\Lambda}_m(\boldsymbol{r}) \cdot \boldsymbol{\Lambda}_n(\boldsymbol{r})\,\mathrm{d}\boldsymbol{r}, \tag{3.48}$$

and the corresponding local Gram matrix $\mathbf{\Gamma}_i \in \mathbb{R}^{N\times N}$ for the i-th cell is defined as

$$(\mathbf{\Gamma}_i)_{mn} = \iint\limits_{\mathcal{S}_i} \boldsymbol{\Lambda}_m(\boldsymbol{r}) \cdot \boldsymbol{\Lambda}_n(\boldsymbol{r})\,\mathrm{d}\boldsymbol{r}. \tag{3.49}$$

At most three RWG basis have their support on a single cell, therefore each matrix $\mathbf{\Gamma}_i$ is extremely sparse, with $O(1)$ non-zero entries.

The computation of the functionals above is always amenable to at most $O(N\log N)$ complexity and $O(N)$ storage. In fact, the product $\mathbf{L}\mathsf{I}$ can be computed with fast factorizations as described in Sec. 2.3.1, and terms of the kind $\mathsf{y} = \mathbf{G}^{-1}\mathsf{x}$ are evaluated directly as solution of the linear system $\mathbf{G}\,\mathsf{y} = \mathsf{x}$; the Gram matrix is $O(N)$ sparse, positive-definite and with $O(1)$ condition number, and therefore the above system can be solved iteratively (e.g., with a conjugate gradient algorithm) in $O(1)$ iterations, thus resulting in $O(N)$ total operations. Lastly, each matrix $\mathbf{\Gamma}_i$, having a constant number of non-zero terms, can be multiplied by a vector in $O(1)$ operations.

In conclusion, the “template” polynomial formula (3.25) encompasses all the terms introduced above. To show this, consider the active power term (3.38), which, using (3.41), can be expressed as

$$q_d = P_d(\mathsf{I}), \quad s_d = P_d(\mathsf{I}), \quad t_d = 0, \qquad d = 1, \dots, N_{\text{c}} \tag{3.50}$$

For the reactance term (3.39), with (3.42) and (3.43), one has

$$\begin{aligned}
&q_d = 0, \qquad s_d = 0, \qquad t_d = X_{\mathrm{L}}\mathcal{J}_d(\mathsf{I}) - Q_d(\mathsf{I}), \qquad d = 1,\dots,N_{\mathrm{c}}\\
&q_d = 0, \qquad s_d = 0, \qquad t_d = Q_d(\mathsf{I}) - X_{\mathrm{U}}\mathcal{J}_d(\mathsf{I}), \qquad d = N_{\mathrm{c}}{+}1,\dots,2N_{\mathrm{c}}
\end{aligned}$$

while, for the scalar term (3.40),

$$\begin{aligned}
&q_d = \mathcal{E}_d(\mathsf{I}), \qquad s_d = \mathcal{J}_d(\mathsf{I}), \qquad t_d = 0, \qquad d = 1,\dots,N_{\mathrm{c}}\\
&q_d = -P_d(\mathsf{I}), \qquad s_d = P_d(\mathsf{I}), \qquad t_d = 0, \qquad d = N_{\mathrm{c}}{+}1,\dots,2N_{\mathrm{c}}\\
&q_d = -Q_d(\mathsf{I}), \qquad s_d = Q_d(\mathsf{I}), \qquad t_d = 0, \qquad d = 2N_{\mathrm{c}}{+}1,\dots,3N_{\mathrm{c}}.
\end{aligned}$$

3.4.2 Enforcement of field specifications

The fact that the unknown current is associated with a given incident field (thus with a known source power) allows to define bounds on the maximum achievable radiated power. This is in contrast to most pattern synthesis problems, where the source amplitude is not intrinsically bounded. In turns, this permits to transform the maximization of the radiated power into the minimization of the difference with respect to its theoretical maximum.

The power P_{inc} is associated with the (given) incident field $\boldsymbol{E}_{\mathrm{inc}}$; it is then natural and practically relevant to normalize the radiated field in terms of *realized gain* [46],

$$G_{\mathrm{r}}(\hat{\boldsymbol{r}},\mathsf{I}) = \frac{|\boldsymbol{E}(\hat{\boldsymbol{r}},\mathsf{I})|^2/\eta_0}{P_{\mathrm{inc}}/4\pi}, \tag{3.51}$$

where η_0 is the free-space impedance, and $\boldsymbol{E}(\hat{\boldsymbol{r}},\mathsf{I})$ is the far field radiated by a given current, with the normalization of Sec. 2.3. This quantity takes into account the reflection of power at the input of the antenna, as the denominator considers the *incident power*, i.e., the power that the source would provide if the antenna has a perfect input matching. Hence, the specification mask in (3.6) will be given by

$$M(\hat{\boldsymbol{r}},\mathsf{I}) = \frac{\eta_0}{4\pi}P_{\mathrm{inc}}\,G_{\mathrm{r}}(\hat{\boldsymbol{r}},\mathsf{I}). \tag{3.52}$$

This allows to directly account for possible anomalous reflection due to bandgap (typical in 1D leaky wave structures) in this automatic design; otherwise said, the present design process also indirectly optimizes reflection of the source field by the metasurface.

The radiated field requirements in (3.10), (3.13)–(3.14) are all expressed as inequalities; using the approach described above, they can be cast directly in terms of functionals to be minimized employing the sampling and the expression of the radiation operator described in Sec. 2.3. The reference level F_{ref} in (3.8) is made explicit as

$$F_{\mathrm{ref}}(\mathsf{I}) = \frac{1}{\Omega_0}\sum_{j\in\Omega_0} F_j^{\mathrm{co}}(\mathsf{I})\Delta\Omega_j \approx \frac{1}{N_0}\sum_{j\in\Omega_0} F_j^{\mathrm{co}}(\mathsf{I}), \tag{3.53}$$

where the shorthand notation $F_j^{\mathrm{co}}(\mathsf{I}) = F^{\mathrm{co}}(\hat{\boldsymbol{r}}_j, \mathsf{I})$ is used. Maximization of the reference level in (3.9) is obtained as a minimization of the difference between the desired lower bound M_0 and the main lobe (average) value $F_{\mathrm{ref}}(\mathsf{I})$,

$$M_0 - F_{\mathrm{ref}}(\mathsf{I}) \leq 0, \tag{3.54}$$

and the related functional is immediately found to be

$$\rho_{\mathrm{ref}} = \mathrm{r}^2\big(M_0 - F_{\mathrm{ref}}(\mathsf{I})\big). \tag{3.55}$$

With the above expressions the mask bounding values result in

$$M_{\mathrm{U/L},j}^{\mathrm{co}}(\mathsf{I}) = \mu_{\mathrm{U/L}}^{\mathrm{co}}(\boldsymbol{r}_j)\, F_{\mathrm{ref}}(\mathsf{I}), \tag{3.56}$$

$$M_j^{\mathrm{cx}}(\mathsf{I}) = \sigma^{\mathrm{cx}}(\hat{\boldsymbol{r}}_j)\, F_{\mathrm{ref}}(\mathsf{I}), \tag{3.57}$$

$$M_j^{\mathrm{SL}}(\mathsf{I}) = \sigma^{\mathrm{SL}}(\hat{\boldsymbol{r}}_j)\, F_{\mathrm{ref}}(\mathsf{I}). \tag{3.58}$$

With these, field constraints result in the following functional:

$$f_{\mathrm{rad}}(\mathsf{I}) = \rho_{\mathrm{ref}}(\mathsf{I}) + w_{\mathrm{ML}}\sum_{j\in\mathrm{ML}}\big(\rho_j^{\mathrm{co}}(\mathsf{I}) + \rho_j^{\mathrm{cx}}(\mathsf{I})\big) + w_{\mathrm{SL}}\sum_{j\in\mathrm{SL}}\rho_j^{\mathrm{tot}}(\mathsf{I}), \tag{3.59}$$

where

$$\rho_j^{\mathrm{co}}(\mathsf{I}) = \mathrm{r}^2\big(M_{\mathrm{L},j}^{\mathrm{co}}(\mathsf{I}) - F_j^{\mathrm{co}}(\mathsf{I})\big) + \mathrm{r}^2\big(F_j^{\mathrm{co}}(\mathsf{I}) - M_{\mathrm{U},j}^{\mathrm{co}}(\mathsf{I})\big), \tag{3.60}$$

$$\rho_j^{\mathrm{cx}}(\mathsf{I}) = \mathrm{r}^2\big(F_j^{\mathrm{cx}}(\mathsf{I}) - M_{\mathrm{U},j}^{\mathrm{cx}}(\mathsf{I})\big), \tag{3.61}$$

$$\rho_j^{\mathrm{tot}}(\mathsf{I}) = \mathrm{r}^2\big(F_j^{\mathrm{tot}}(\mathsf{I}) - M_{\mathrm{U},j}^{\mathrm{tot}}(\mathsf{I})\big), \tag{3.62}$$

with again the shorthand notation $F_j^{\mathrm{x,t}} = F^{\mathrm{x,t}}(\hat{\boldsymbol{r}}_j)$ (3.3). The field magnitude for the different polarizations can be evaluated as

$$\begin{aligned} F_j^{\mathrm{co}}(\mathsf{I}) &= \left|\boldsymbol{E}_j(\mathsf{I}) \cdot \hat{\boldsymbol{p}}_j^*\right|^2 = \left|E_j^\theta(\mathsf{I})\,\hat{p}_j^{\theta *} + E_j^\varphi(\mathsf{I})\,\hat{p}_j^{\varphi *}\right|^2 \\ &= \left|E_j^\theta(\mathsf{I})\right|^2 \left|\hat{p}_j^\theta\right|^2 + \left|E_j^\varphi(\mathsf{I})\right|^2 \left|\hat{p}_j^\varphi\right|^2 + 2\,\mathrm{Re}(E_j^\theta(\mathsf{I}) E_j^{\varphi *}(\mathsf{I}) \hat{p}_j^\theta \hat{p}_j^{\varphi *}), \end{aligned} \tag{3.63}$$

$$\begin{aligned} F_j^{\mathrm{cx}}(\mathsf{I}) &= \left|\boldsymbol{E}_j(\mathsf{I}) \cdot \hat{\boldsymbol{q}}_j^*\right|^2 = \left|E_j^\theta(\mathsf{I})\,\hat{q}_j^{\theta *} + E_j^\varphi(\mathsf{I})\,\hat{q}_j^{\varphi *}\right|^2 \\ &= \left|E_j^\theta(\mathsf{I})\right|^2 \left|\hat{q}_j^\theta\right|^2 + \left|E_j^\varphi(\mathsf{I})\right|^2 \left|\hat{q}_j^\varphi\right|^2 + 2\,\mathrm{Re}(E_j^\theta(\mathsf{I}) E_j^{\varphi *}(\mathsf{I}) \hat{q}_j^\theta \hat{q}_j^{\varphi *}), \end{aligned} \tag{3.64}$$

$$F_j^{\mathrm{tot}}(\mathsf{I}) = \left|\boldsymbol{E}_j(\mathsf{I})\right|^2 = \left|E_j^\theta(\mathsf{I})\right|^2 + \left|E_j^\varphi(\mathsf{I})\right|^2, \tag{3.65}$$

where $\hat{\boldsymbol{p}}_j = \hat{\boldsymbol{p}}(\hat{\boldsymbol{r}}_j)$, $\hat{\boldsymbol{q}}_j = \hat{\boldsymbol{q}}(\hat{\boldsymbol{r}}_j)$, and the elements

$$\left|E_j^\theta(\mathsf{I})\right|^2 = \left(\mathsf{E}_\theta(\mathsf{I}) \odot \mathsf{E}_\theta^*(\mathsf{I})\right)_j, \tag{3.66}$$

$$\left|E_j^\varphi(\mathsf{I})\right|^2 = \left(\mathsf{E}_\varphi(\mathsf{I}) \odot \mathsf{E}_\varphi^*(\mathsf{I})\right)_j, \tag{3.67}$$

$$E_j^\theta(\mathsf{I}) E_j^{\varphi *}(\mathsf{I}) = \left(\mathsf{E}_\theta(\mathsf{I}) \odot \mathsf{E}_\varphi^*(\mathsf{I})\right)_j \tag{3.68}$$

may be evaluated exploiting fast matrix-vector product routines for the computation of E_θ and E_φ through (2.30), (2.31). In the above, $\odot$ indicates the element-wise product.

In practical applications, one often seeks to maximize the gain in the main lobe, i.e., without the specification of an absolute lower bound for it. This is simply obtained by setting the lower bound M_0 to a theoretical maximum for the given antenna under consideration, e.g., the one that would be obtained by a constant current and assuming the radiated power equal to the incident one. In the design of pencil beam antennas, the upper bound $M_{\mathrm{U}}^{\mathrm{co}}$ is not present, with related simplification of the ML functional ρ^{co}. In addition, a sensible choice of the averaging ML region Ω_0 allows to use only the functional ρ_{ref}.

3.4.3 Gradient computation

The proposed formulation allows to effectively make use of fast algorithms also for the gradient computation. In particular, the quadratic form of the terms result in linear gradients, and the sum over all terms allows to isolate the computationally intensive parts and drastically reduce the number of matrix-vector products required.

Matrices and vectors introduced in the previous sections are complex. On the other hand, optimization algorithms usually deal with real vectors; in an effort to keep all computations in the complex domain for numerical convenience, the approach proposed in [47] has been followed. The use of the *complex gradient* operator $\tilde{\nabla}$, defined in App. D, significantly simplifies the mathematical derivation. The introduction of this new operator is justified by the fact that, for a real-valued function $f : \mathbb{C}^N \to \mathbb{R}$, $\tilde{\nabla} f$ corresponds to the direction of maximum increase of the function and the condition $\tilde{\nabla} f = 0$ is necessary and sufficient to determine a stationary point for f. In App. D, the mathematical proofs of these statements are detailed.

The required gradients are expressed in complex format by using the properties reported in App. D, yielding

$$\tilde{\nabla} P_i = \frac{1}{2} \left(\boldsymbol{\Gamma}_i \mathsf{V} + \mathbf{K}^{\mathsf{H}} \boldsymbol{\Gamma}_i \mathsf{I} \right), \tag{3.69}$$

$$\tilde{\nabla} Q_i = \frac{1}{2\mathrm{j}} \left(\boldsymbol{\Gamma}_i \mathsf{V} - \mathbf{K}^{\mathsf{H}} \boldsymbol{\Gamma}_i \mathsf{I} \right), \tag{3.70}$$

$$\tilde{\nabla} \mathcal{J}_i = \frac{1}{2} \left(\boldsymbol{\Gamma}_i + \boldsymbol{\Gamma}_i^{\mathsf{H}} \right) \mathsf{I} = \boldsymbol{\Gamma}_i \mathsf{I}, \tag{3.71}$$

$$\tilde{\nabla} \mathcal{E}_i = \mathbf{K}^{\mathsf{H}} \boldsymbol{\Gamma}_i \mathsf{V}, \tag{3.72}$$

where the matrix $\mathbf{K}$ was defined in (3.46), and the products involving its hermitian transpose are computed in the following way:

$$\mathbf{K}^{\mathsf{H}} \mathsf{z} = (\mathbf{G}^{-1} \mathbf{L})^{\mathsf{H}} \mathsf{z} = \mathbf{L}^{\mathsf{H}} \mathbf{G}^{-1} \mathsf{z}, \tag{3.73}$$

having exploited the symmetry of $\mathbf{G}^{-1}$. An important observation is that the EFIO matrix $\mathbf{L}$ is symmetric, i.e., $\mathbf{L}^{\mathsf{T}} = \mathbf{L}$, but not self-adjoint. Thus, matrix-vector products involving its complex transpose are computed as

$$\mathbf{L}^{\mathsf{H}} \mathsf{z} = (\mathbf{L}^{\mathsf{T}} \mathsf{z}^*)^* = (\mathbf{L} \mathsf{z}^*)^*, \tag{3.74}$$

which allows to leverage fast algorithms to multiply $\mathbf{L}$ by a vector. The total gradient is obtained by linearity as a sum of all individual gradients. As an example, the gradient of the ρ_{act} functional is given by

$$\begin{aligned}\tilde{\nabla}\Big[\textstyle\sum_i P_i^2\Big] &= 2\textstyle\sum_i P_i \tilde{\nabla} P_i \\ &= 2\textstyle\sum_i P_i \frac{1}{2}\big(\mathbf{\Gamma}_i \mathsf{V} + \mathbf{K}^{\mathsf{H}}\mathbf{\Gamma}_i \mathsf{I}\big) \\ &= \Big[\textstyle\sum_i P_i \mathbf{\Gamma}_i \mathsf{V}\Big] + \mathbf{K}^{\mathsf{H}}\Big[\textstyle\sum_i P_i \mathbf{\Gamma}_i \mathsf{I}\Big].\end{aligned} \tag{3.75}$$

The interchange of the summation with the operator $\mathbf{K}^{\mathsf{H}}$ is key as it allows to compute the total gradient by requiring only one computationally intensive matrix-vector product. The remaining products, involving extremely sparse matrices $\mathbf{\Gamma}_i$, are computed individually, as their complexity remains negligible with respect to the total one.

The same is true for the inequality terms; in the case of ρ_{rct}, by defining $\Psi_i = Q_i - X\mathscr{J}_i$ and noting that $\frac{\mathrm{d}}{\mathrm{d}x}\mathrm{r}^2(x) = 2\,\mathrm{r}(x)$, one has

$$\begin{aligned}\tilde{\nabla}\Psi_i &= \tilde{\nabla}Q_i - X\tilde{\nabla}\mathscr{J}_i \\ &= \frac{1}{2\mathrm{j}}\left(\mathbf{\Gamma}_i \mathsf{V} - \mathbf{K}^{\mathsf{H}}\mathbf{\Gamma}_i \mathsf{I}\right) - X\mathbf{\Gamma}_i \mathsf{I} \\ &= \frac{1}{2}\big(- \mathrm{j}\mathbf{\Gamma}_i \mathsf{V} + (\mathrm{j}\mathbf{K}^{\mathsf{H}} - 2X)\mathbf{\Gamma}_i \mathsf{I}\big),\end{aligned} \tag{3.76}$$

and so

$$\begin{aligned}\tilde{\nabla}\Big[\textstyle\sum_i \mathrm{r}^2(\Psi_i)\Big] &= 2\textstyle\sum_i \mathrm{r}(\Psi_i)\tilde{\nabla}\Psi_i \\ = -\mathrm{j}\Big[\textstyle\sum_i \mathrm{r}(\Psi_i)\mathbf{\Gamma}_i \mathsf{V}\Big] &+ (\mathrm{j}\mathbf{K}^{\mathsf{H}} - 2X)\Big[\textstyle\sum_i \mathrm{r}(\Psi_i)\mathbf{\Gamma}_i \mathsf{I}\Big],\end{aligned} \tag{3.77}$$

where, again, only one matrix-vector product with $\mathbf{K}^{\mathsf{H}}$ is required. Regarding the functional for the field specifications, the gradients of the field magnitude samples read

$$\begin{aligned}\tilde{\nabla}F_j^{\mathrm{co}} &= \left|\hat{p}_j^{\theta}\right|^2 E_j^{\theta}\,\mathbf{R}_{\theta}^{\mathsf{H}}\mathsf{e}_j + \left|\hat{p}_j^{\varphi}\right|^2 E_j^{\varphi}\,\mathbf{R}_{\varphi}^{\mathsf{H}}\mathsf{e}_j \\ &\quad + \hat{p}_j^{\theta}\hat{p}_j^{\varphi *}E_j^{\theta}\,\mathbf{R}_{\varphi}^{\mathsf{H}}\mathsf{e}_j + \hat{p}_j^{\theta *}\hat{p}_j^{\varphi}E_j^{\varphi}\,\mathbf{R}_{\theta}^{\mathsf{H}}\mathsf{e}_j,\end{aligned} \tag{3.78}$$

$$\begin{aligned}\tilde{\nabla}F_j^{\mathrm{cx}} &= \left|\hat{q}_j^{\theta}\right|^2 E_j^{\theta}\,\mathbf{R}_{\theta}^{\mathsf{H}}\mathsf{e}_j + \left|\hat{q}_j^{\varphi}\right|^2 E_j^{\varphi}\,\mathbf{R}_{\varphi}^{\mathsf{H}}\mathsf{e}_j \\ &\quad + \hat{q}_j^{\theta}\hat{q}_j^{\varphi *}E_j^{\theta}\,\mathbf{R}_{\varphi}^{\mathsf{H}}\mathsf{e}_j + \hat{q}_j^{\theta *}\hat{q}_j^{\varphi}E_j^{\varphi}\,\mathbf{R}_{\theta}^{\mathsf{H}}\mathsf{e}_j,\end{aligned} \tag{3.79}$$

$$\tilde{\nabla}F_j^{\mathrm{tot}} = E_j^{\theta}\,\mathbf{R}_{\theta}^{\mathsf{H}}\mathsf{e}_j + E_j^{\varphi}\,\mathbf{R}_{\varphi}^{\mathsf{H}}\mathsf{e}_j, \tag{3.80}$$

where $(\mathsf{e}_j)_k = \delta_{jk}$. The gradient for the total field term in (3.59) is found in a way similar to what has been shown before. By defining $\Phi_j = F_j^{\text{tot}} - M_{\text{U},i}^{\text{tot}}$, the gradient is expressed as

$$\begin{aligned} \tilde{\nabla}\Phi_j &= \tilde{\nabla}F_j^{\text{tot}} - \tilde{\nabla}M_{\text{U},j}^{\text{tot}} \\ &= \tilde{\nabla}F_j^{\text{tot}} = E_j^{\theta}\,\mathbf{R}_{\theta}^{\mathsf{H}}\mathsf{e}_j + E_j^{\varphi}\,\mathbf{R}_{\varphi}^{\mathsf{H}}\mathsf{e}_j, \end{aligned} \tag{3.81}$$

where the simplifying assumption of absolute masks, i.e., $\tilde{\nabla}M_{\text{U},j}^{\text{tot}} = 0$, has been made to avoid complicate expressions. Employing relative masks does not change the overall complexity, as they are just linear combinations of field samples. Then

$$\begin{aligned} &\tilde{\nabla}\Big[\textstyle\sum_j \mathrm{r}^2(\Phi_j)\Big] = 2\textstyle\sum_j \mathrm{r}(\Phi_j)\tilde{\nabla}\Phi_j \\ &= 2\textstyle\sum_j \mathrm{r}(\Psi_j)\big[E_j^{\theta}\,\mathbf{R}_{\theta}^{\mathsf{H}}\mathsf{e}_j + E_j^{\varphi}\,\mathbf{R}_{\varphi}^{\mathsf{H}}\mathsf{e}_j\big] \\ &= \mathbf{R}_{\theta}^{\mathsf{H}}\Big[2\textstyle\sum_j \mathrm{r}(\Psi_j)E_j^{\theta}\mathsf{e}_j\Big] + \mathbf{R}_{\varphi}^{\mathsf{H}}\Big[2\textstyle\sum_j \mathrm{r}(\Psi_j)E_j^{\varphi}\mathsf{e}_j\Big]. \end{aligned} \tag{3.82}$$

Once again, by rearranging summations and products, the computationally intensive matrix-vector products are done only once per gradient evaluation. The adjoints of the radiation matrices, $\mathbf{R}_{\theta}^{\mathsf{H}}$ and $\mathbf{R}_{\varphi}^{\mathsf{H}}$, are found by considering that the radiation operator (2.32) is symmetric, i.e., $\mathcal{R} = \mathcal{R}^{\mathsf{T}}$, which leads to

$$\begin{aligned} (\mathbf{R}_{\theta}^{\mathsf{H}})_{nj} = (\mathbf{R}_{\theta}^{\mathsf{T}})_{nj}^{*} &= \Big(\boldsymbol{\Lambda}_n \cdot \big(\mathcal{R}^{\mathsf{T}}\hat{\boldsymbol{\theta}}_j\big)\Big)^{*} \\ &= \Big(\boldsymbol{\Lambda}_n \cdot \big(\mathcal{R}\hat{\boldsymbol{\theta}}_j\big)\Big)^{*} \\ &= \boldsymbol{\Lambda}_n \cdot \big(\mathcal{R}\hat{\boldsymbol{\theta}}_j\big)^{*}. \end{aligned} \tag{3.83}$$

In the derivation, the fact that $\boldsymbol{\Lambda}_n^{*} = \boldsymbol{\Lambda}_n$ is used. The same applies to the matrix $\mathbf{R}_{\varphi}^{\mathsf{H}}$, upon substitution of $\hat{\boldsymbol{\theta}}_j$ with $\hat{\boldsymbol{\varphi}}_j$.

3.4.4 Line search

As anticipated, the minimization of the functional $f(\mathsf{I})$ described in previous sections is carried out with a *non-linear conjugate gradient* algorithm [45, p. 121]; this means that the iteration update is of the type

$$\mathsf{I}_{k+1} = \mathsf{I}_k + \alpha_k\,\mathsf{p}_k, \tag{3.84}$$

with $k = 0, \dots, K_{\max}$, where $\alpha_k \in \mathbb{R}$ is to be found so that the functional is minimized, and $\mathsf{p}_k \in \mathbb{C}^N$ is the update direction, which incorporates gradient information,

$$\mathsf{p}_k = \begin{cases} -\tilde{\nabla} f_k, & \text{if } k = 0 \\ -\tilde{\nabla} f_k + \beta_k\, \mathsf{p}_{k-1}, & \text{if } k > 0 \end{cases} \tag{3.85}$$

Different formulas have been proposed in the literature for the parameter $\beta \in \mathbb{R}$. The following are the main ones (expressed with complex gradients),

$$\beta_k^{\mathrm{FR}} = \frac{\|\tilde{\nabla} f_k\|^2}{\|\tilde{\nabla} f_{k-1}\|^2}, \qquad \text{Fletcher-Reeves} \tag{3.86}$$

$$\beta_k^{\mathrm{PR}} = \frac{\mathrm{Re}\left(\tilde{\nabla} f_k^{\mathsf{H}}(\tilde{\nabla} f_k - \tilde{\nabla} f_{k-1})\right)}{\|\tilde{\nabla} f_{k-1}\|^2}, \qquad \text{Polak-Ribière} \tag{3.87}$$

$$\beta_k^{\mathrm{HS}} = \frac{\mathrm{Re}\left(\tilde{\nabla} f_k^{\mathsf{H}}(\tilde{\nabla} f_k - \tilde{\nabla} f_{k-1})\right)}{\mathrm{Re}\left(\mathsf{p}_{k-1}^{\mathsf{H}}(\tilde{\nabla} f_k - \tilde{\nabla} f_{k-1})\right)}, \qquad \text{Hestenes–Stiefel} \tag{3.88}$$

$$\beta_k^{\mathrm{CD}} = -\frac{\|\tilde{\nabla} f_k\|^2}{\mathrm{Re}\left(\mathsf{p}_{k-1}^{\mathsf{H}}\tilde{\nabla} f_{k-1}\right)}, \qquad \text{Conjugate-Descent} \tag{3.89}$$

$$\beta_k^{\mathrm{DY}} = \frac{\|\tilde{\nabla} f_k\|^2}{\mathrm{Re}\left(\mathsf{p}_{k-1}^{\mathsf{H}}(\tilde{\nabla} f_k - \tilde{\nabla} f_{k-1})\right)}, \qquad \text{Dai-Yuan} \tag{3.90}$$

$$\beta_k^{\mathrm{LS}} = \frac{\mathrm{Re}\left(\tilde{\nabla} f_k^{\mathsf{H}}(\tilde{\nabla} f_k - \tilde{\nabla} f_{k-1})\right)}{\mathrm{Re}\left(\mathsf{p}_{k-1}^{\mathsf{H}}\tilde{\nabla} f_{k-1}\right)}. \qquad \text{Liu-Storey} \tag{3.91}$$

They all reduce to the classical conjugate-gradient formula when f is a quadratic function. In practice, the choice depends on the application and may require experimentation.

As seen above, at each step of the minimization process, one updates the solution by looking for the optimum along the chosen direction; this step is known as *line search*, and is formally indicated as the process of finding the optimum step $\alpha^\star$ such that:

$$\alpha^\star = \arg\min_{\alpha \in \mathbb{R}} f(\mathsf{I} + \alpha\, \mathsf{p}). \tag{3.92}$$

Here, and in the following, the dependence of all quantities on the iteration index k has been dropped for clarity. This line optimization is performed at each step of the process, thus its numerical cost is of paramount importance. Both the computation of the cost function evaluated along the search direction $\mathsf{I}+\alpha\,\mathsf{p}$,

$$g(\alpha) = f(\mathsf{I} + \alpha\,\mathsf{p}), \tag{3.93}$$

and the optimization process are greatly expedited by the choice to employ only polynomial functionals of the form (3.25) (see Sec. 3.4).

First of all, the polynomial structure is made explicit for each term, when evaluated in (3.93). The procedure is outlined for the term q_d only, but the same applies for s_d and t_d. Starting from (3.25) evaluated along the direction p, one finds

$$\begin{aligned} q_d(\mathsf{I}+\alpha\,\mathsf{p}) &= \Phi\big((\mathsf{I}+\alpha\,\mathsf{p})^{\mathsf{H}}\mathbf{A}_d(\mathsf{I}+\alpha\,\mathsf{p}) + (\mathsf{I}+\alpha\,\mathsf{p})^{\mathsf{H}}\mathsf{b}_d + c_d\big) \\ &= q_{0d} + \alpha\, q_{1d} + \alpha^2 q_{2d}, \end{aligned} \tag{3.94}$$

where $\Phi = \mathrm{Re}$ or Im. The coefficients of the second order polynomial are given by

$$q_{0d} = \Phi(\mathsf{I}^{\mathsf{H}}\mathbf{A}_d\mathsf{I} + \mathsf{I}^{\mathsf{H}}\mathsf{b}_d + c_d), \tag{3.95}$$

$$q_{1d} = \Phi(\mathsf{I}^{\mathsf{H}}\mathbf{A}_d\mathsf{p} + \mathsf{p}^{\mathsf{H}}\mathbf{A}_d\mathsf{I} + \mathsf{p}^{\mathsf{H}}\mathsf{b}_d), \tag{3.96}$$

$$q_{2d} = \Phi(\mathsf{p}^{\mathsf{H}}\mathbf{A}_d\mathsf{p}), \tag{3.97}$$

where $\mathbf{A}_d$ indicate the matrices appearing in the definition of the objective function terms. By defining the arrays of coefficients

$$\mathsf{q}_0 = [\cdots q_{0d} \cdots]^{\mathsf{T}}, \tag{3.98}$$

$$\mathsf{q}_1 = [\cdots q_{1d} \cdots]^{\mathsf{T}}, \tag{3.99}$$

$$\mathsf{q}_2 = [\cdots q_{2d} \cdots]^{\mathsf{T}}, \tag{3.100}$$

for the polynomials q and, accordingly, for s and t ones, (3.93) can be conveniently expressed as

$$\begin{aligned} g(\alpha) = {} & (\mathsf{q}_0 + \alpha\,\mathsf{q}_1 + \alpha^2\mathsf{q}_2)^{\mathsf{T}}\,(\mathsf{s}_0 + \alpha\,\mathsf{s}_1 + \alpha^2\mathsf{s}_2) \\ & + \mathrm{r}(\mathsf{t}_0 + \alpha\,\mathsf{t}_1 + \alpha^2\mathsf{t}_2)^{\mathsf{T}}\,\mathrm{r}(\mathsf{t}_0 + \alpha\,\mathsf{t}_1 + \alpha^2\mathsf{t}_2). \end{aligned} \tag{3.101}$$

This formulation allows to evaluate the objective function (3.93) for *any* value of α at the cost of computing the matrix-vector products involving $\mathbf{A}_d$ only once, to evaluate $\mathbf{A}_d\mathsf{p}$, as terms $\mathbf{A}_d\mathsf{I}$ are already computed and stored during the evaluation of the objective function.

The polynomial expression (3.94) can be made explicit for the terms appearing in the objective function. Consider the *current magnitude* term defined in (3.43); evaluating it along a direction p results in the following expression:

$$\begin{aligned}\mathcal{J}_i(\mathsf{I}+\alpha\,\mathsf{p}) &= (\mathsf{I}+\alpha\,\mathsf{p})^{\mathsf{H}}\boldsymbol{\Gamma}_i(\mathsf{I}+\alpha\,\mathsf{p})\\ &= \left(\mathsf{I}^{\mathsf{H}}\boldsymbol{\Gamma}_i\mathsf{I}+\alpha\left(\mathsf{I}^{\mathsf{H}}\boldsymbol{\Gamma}_i\mathsf{p}+\mathsf{p}^{\mathsf{H}}\boldsymbol{\Gamma}_i\mathsf{I}\right)+\alpha^2\,\mathsf{p}^{\mathsf{H}}\boldsymbol{\Gamma}_i\mathsf{p}\right)\\ &= \left(\mathsf{I}^{\mathsf{H}}\boldsymbol{\Gamma}_i\mathsf{I}\right)+\alpha\,2\,\mathrm{Re}\left(\mathsf{I}^{\mathsf{H}}\boldsymbol{\Gamma}_i\mathsf{p}\right)+\alpha^2\left(\mathsf{p}^{\mathsf{H}}\boldsymbol{\Gamma}_i\mathsf{p}\right).\end{aligned}\tag{3.102}$$

The same can be done for the active power term (3.41), which gives

$$\begin{aligned}P_i(\mathsf{I}+\alpha\,\mathsf{p}) &= \mathrm{Re}\left((\mathsf{I}+\alpha\,\mathsf{p})^{\mathsf{H}}\boldsymbol{\Gamma}_i(\mathsf{V}+\alpha\,\mathbf{K}\mathsf{p})\right)\\ &= \mathrm{Re}\left(\mathsf{I}^{\mathsf{H}}\boldsymbol{\Gamma}_i\mathsf{V}+\alpha\left(\mathsf{I}^{\mathsf{H}}\boldsymbol{\Gamma}_i\mathbf{K}\mathsf{p}+\mathsf{p}^{\mathsf{H}}\boldsymbol{\Gamma}_i\mathsf{V}\right)+\alpha^2\,\mathsf{p}^{\mathsf{H}}\boldsymbol{\Gamma}_i\mathbf{K}\mathsf{p}\right)\\ &= \mathrm{Re}\left(\mathsf{I}^{\mathsf{H}}\boldsymbol{\Gamma}_i\mathsf{V}\right)+\alpha\ \mathrm{Re}\left(\mathsf{I}^{\mathsf{H}}\boldsymbol{\Gamma}_i\mathbf{K}\mathsf{p}+\mathsf{p}^{\mathsf{H}}\boldsymbol{\Gamma}_i\mathsf{V}\right)+\alpha^2\ \mathrm{Re}\left(\mathsf{p}^{\mathsf{H}}\boldsymbol{\Gamma}_i\mathbf{K}\mathsf{p}\right).\end{aligned}\tag{3.103}$$

As a last example, each of the *field magnitude* terms for the co- or cross-polarization (3.63)–(3.65) can be expressed as

$$\begin{aligned}F_j(\mathsf{I}+\alpha\,\mathsf{p}) &= \Big(\left(\mathsf{E}+\alpha\,\mathbf{R}\mathsf{p}\right)\odot\left(\mathsf{E}+\alpha\,\mathbf{R}\mathsf{p}\right)^*\Big)_j\\ &= \left(\mathsf{E}\odot\mathsf{E}^*\right)_j+\alpha\left(\mathsf{E}\odot(\mathbf{R}\mathsf{p})^*+(\mathbf{R}\mathsf{p})\odot\mathsf{E}^*\right)_j+\alpha^2\left((\mathbf{R}\mathsf{p})\odot(\mathbf{R}\mathsf{p})^*\right)_j\\ &= \left(\mathsf{E}\odot\mathsf{E}^*\right)_j+\alpha\,2\,\mathrm{Re}\left(\mathsf{E}\odot(\mathbf{R}\mathsf{p})^*\right)_j+\alpha^2\left((\mathbf{R}\mathsf{p})\odot(\mathbf{R}\mathsf{p})^*\right)_j.\end{aligned}\tag{3.104}$$

An analytical solution for the minimization of $g(\alpha)$ is important for avoiding scaling issues of the step length, which is known to be a crucial problem of line search procedures [45]. It can be shown by starting with the simplest case of functionals without inequalities (i.e., without ramp functions), that corresponds to a phaseless pattern fitting with no bounds on the reactance values. In this case the objective function $g(\alpha)$ reduces to a fourth-order polynomial and the line search procedure is direct: the derivative $\frac{\mathrm{d}g}{\mathrm{d}\alpha}$ is a third-order polynomial, and its roots may be found in closed form. A closed form solution not only reduces the cost of finding the stationary point, but it also avoids the need to determine the *interval* in which to look for the optimum step length.

In the presence of functions $\mathrm{r}^2(x)$, the objective $g(\alpha)$ is still a fourth-order polynomial, but it is piecewise so (see Fig. 3.6 for a graphical example); because of the continuity of the derivative of $\mathrm{r}^2(x)$, the derivative $\frac{\mathrm{d}g}{\mathrm{d}\alpha}$ is also a piecewise

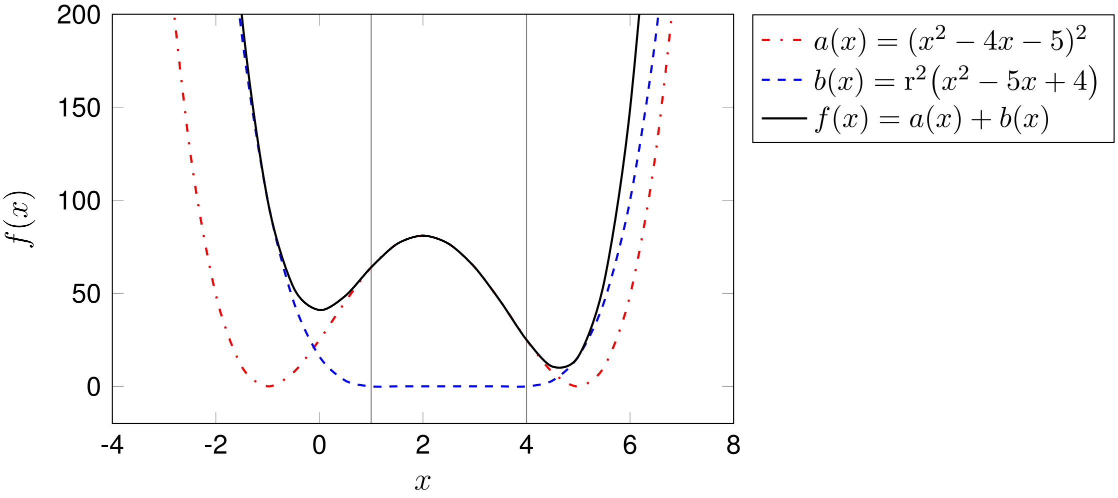

Fig. 3.6 Example of a piecewise fourth-order polynomial function $f(x)$. It is the sum of two terms: $a(x)$ is the square of a second-order polynomial, while $b(x)$ is obtained by applying the squared ramp to a second-order polynomial. Vertical lines identify the intervals where the function has a fixed polynomial behaviour.

continuous polynomial, and the determination of its roots can be done with an iterative process that again does not require to estimate the interval in which to look for a solution. The devised iterative algorithm for the line search is described in the form of a pseudo-code in Algorithm 3. It can be described as follows: note that for a generic function $\phi(x)$,

$$\mathrm{r}(\phi(x)) = \mathrm{u}(\phi(x))\,\phi(x), \tag{3.105}$$

where $\mathrm{u}(x)$ is the unit step function; hence, the non-linear (rectifying) behavior of a ramp can be represented as an on/off switch. Then, consider the ramp-less "switched" version $g^{\mathrm{s}}(\alpha; \mathsf{u})$ of (3.101) in which all terms of the kind $\mathrm{r}(t_d(\alpha))$ are replaced by $u_d\, t_d(\alpha)$, with $u_d = \mathrm{u}(t_d(\alpha)) \in \{0, 1\}$ and where $\mathsf{u} = [u_1, ..., u_{N_\mathrm{s}}]$ is the switch pattern vector (N_s is the number of switches, i.e., of ramp terms). For any given pattern of switch states, the function $g^{\mathrm{s}}(\alpha; \mathsf{u})$ is always a fourth-order polynomial whose minimum point is computed in closed form as anticipated above. One starts by computing the switch pattern for $\alpha = 0$, which yields u_0, and finds the minimum $\alpha_0^\star$ of $g^{\mathrm{s}}(\alpha; \mathsf{u}_0)$. With this new value of α, one now evaluates the switches again, which results in the pattern u_1, and the determination of the minimum point is repeated for $g^{\mathrm{s}}(\alpha; \mathsf{u}_1)$, yielding $\alpha_1^\star$. The process is iterated until the switch pattern remains unchanged, i.e., $\mathsf{u}_n = \mathsf{u}_{n-1}$: at that point, $g^{\mathrm{s}}(\alpha; \mathsf{u}_n) = g(\alpha)$, and $\alpha_n^\star = \alpha^\star$ is the sought-for minimum point. The algorithm usually converges in much less than N_s iterations.

Algorithm 3 Algorithm for the line minimization of functionals of type (3.101) containing inequality terms. The procedure minpoly4 finds the minimum point of the 4th order polynomial defined by coefficients $a_0, \dots, a_4$ by computing the stationary points in closed-form and evaluating the polynomial in all such points to find the global minimum.

```
procedure LineSearch($\mathsf{q}_0, \mathsf{q}_1, \mathsf{q}_2, \mathsf{s}_0, \mathsf{s}_1, \mathsf{s}_2, \mathsf{t}_0, \mathsf{t}_1, \mathsf{t}_2$)
    $b_0 \leftarrow \mathsf{q}_0^\mathsf{T}\mathsf{s}_0$
    $b_1 \leftarrow \mathsf{q}_1^\mathsf{T}\mathsf{s}_0 + \mathsf{q}_0^\mathsf{T}\mathsf{s}_1$
    $b_2 \leftarrow \mathsf{q}_2^\mathsf{T}\mathsf{s}_0 + \mathsf{q}_1^\mathsf{T}\mathsf{s}_1 + \mathsf{q}_0^\mathsf{T}\mathsf{s}_2$
    $b_3 \leftarrow \mathsf{q}_1^\mathsf{T}\mathsf{s}_2 + \mathsf{q}_2^\mathsf{T}\mathsf{s}_1$
    $b_4 \leftarrow \mathsf{q}_2^\mathsf{T}\mathsf{s}_2$
    $\mathsf{u} \leftarrow \mathrm{u}(\mathsf{s}_0)$
    repeat
        $\mathsf{t}_0' \leftarrow \mathsf{u} \odot \mathsf{t}_0$
        $\mathsf{t}_1' \leftarrow \mathsf{u} \odot \mathsf{t}_1$
        $\mathsf{t}_2' \leftarrow \mathsf{u} \odot \mathsf{t}_2$
        $a_0 \leftarrow b_0 + \mathsf{t}_0'^\mathsf{T}\mathsf{t}_0'$
        $a_1 \leftarrow b_1 + 2\,\mathsf{t}_1'^\mathsf{T}\mathsf{t}_0'$
        $a_2 \leftarrow b_2 + 2\,\mathsf{t}_2'^\mathsf{T}\mathsf{t}_0' + \mathsf{t}_1'^\mathsf{T}\mathsf{t}_1'$
        $a_3 \leftarrow b_3 + 2\,\mathsf{t}_2'^\mathsf{T}\mathsf{t}_1'$
        $a_4 \leftarrow b_4 + \mathsf{t}_2'^\mathsf{T}\mathsf{t}_2'$
        $\alpha \leftarrow \mathrm{minpoly4}(a_0, a_1, a_2, a_3, a_4)$
        $\mathsf{u}_\mathrm{old} \leftarrow \mathsf{u}$
        $\mathsf{t} \leftarrow \mathsf{t}_0 + \alpha\,\mathsf{t}_1 + \alpha^2\mathsf{t}_2$
        $\mathsf{u} \leftarrow \mathrm{u}(\mathsf{t})$
    until $\mathsf{u} = \mathsf{u}_\mathrm{old}$
    return $\alpha$
end procedure
```

3.4.5 Complexity analysis

As anticipated in the introduction to the chapter, a benefit of the proposed formulation is the potential for low numerical complexity, when the relevant matrix-vector products are computed using fast algorithm. Table 3.2 summarizes the complexity of all matrix-vector operations; the total count includes all operations needed for the evaluation of the objective function, of its gradient, and for the line-search.

Table 3.2 Summary of the matrix-vector operations needed for each iteration, with their respective complexity and total number of occurrences. All operations are considered in complex format, and $\mathsf{a} \in \mathbb{C}^N$ is a generic array.

Operation	Complexity	Count
$\mathsf{L}\mathsf{a}$	$O(N \log N)$	5
$\mathsf{R}\mathsf{a}$	$O(N_\mathrm{f} \log N)$	3
$\mathsf{G}^{-1}\mathsf{a}$	$O(N)$	5
$\mathsf{\Gamma}_i\, \mathsf{a}$	$O(1)$	$6N_\mathrm{c}$

Given that the number of sampling points in the far field, N_f, is largely independent of the number of unknowns N, and the number of cells N_c is approximately proportional to N, the total asymptotic complexity (neglecting multiplicative constants) results in

$$O(N \log N) + O(\log N) + O(N) + NO(1) = O(N \log N).$$

In this estimation, vector-vector operations have been omitted since their complexity is negligible with respect to matrix-vector ones.

3.5 Impedance computation

Once the optimum current coefficients $\mathsf{I}^\star$ have been obtained with the process described in the previous section, the corresponding total electric field is also known, and the sought impedance $Z(\boldsymbol{r})$ can be obtained via (2.25) and the definition of Z (2.27).

In order to formulate an equation for the impedance spatial distribution $Z(\boldsymbol{r})$, one must start with its representation in terms of L assigned basis functions $\psi_\ell(\boldsymbol{r})$,

$$Z(\boldsymbol{r}) = \sum_{\ell=1}^{L} z_\ell \, \psi_\ell(\boldsymbol{r}), \tag{3.106}$$

where the array $\mathsf{z} \in \mathbb{C}^L$ collects the expansion coefficients. Note that this step—including the choice of the impedance basis functions—is completely independent from the solution of the optimization process described above, and any post-processing to it. Indeed, more than one representations of $Z(\boldsymbol{r})$ and ensuing impedance reconstructions could be done for ensuring a stable result. Inserting (3.106) into (2.27), the IBC matrix Z can be expressed as

$$(\mathsf{Z})_{mn} = \sum_{\ell=1}^{L} z_\ell \, g^{\ell}_{mn}, \qquad g^{\ell}_{mn} = \langle \, \boldsymbol{\Lambda}_m \, , \psi_\ell \, \boldsymbol{\Lambda}_n \, \rangle, \tag{3.107}$$

and after some elaboration one finds

$$\mathsf{Z}\mathsf{I}^\star = \mathsf{C}\mathsf{z}, \tag{3.108}$$

where $\mathsf{C}(\mathsf{I}^\star) \in \mathbb{C}^{N\times L}$ is defined as

$$(\mathsf{C})_{m\ell} = \sum_{n=1}^{N} g^{\ell}_{mn} I^\star_n. \tag{3.109}$$

Consistency with the discretized EFIE-IBC (2.25) requires

$$\mathsf{C}\mathsf{z} = \mathsf{V}_{\text{tot}}, \tag{3.110}$$

with the total electric field $\mathsf{V}_{\text{tot}} = \mathsf{V}_{\text{inc}} + \mathsf{L}\mathsf{I}^\star$, so that

$$\mathsf{z}^\star = \underset{\mathsf{z}\,\in\,\mathbb{C}^L}{\arg\min} \, \|\mathsf{C}\mathsf{z} - \mathsf{V}_{\text{tot}}\|^2 \,, \tag{3.111}$$

which corresponds to a linear least-squares minimization problem that can be solved with standard techniques. Even when the optimization converges with a low residual value, it is unlikely that the PL condition (3.1) and the bounds on the reactance value (3.2) are verified for every cell. For this reason, the least-squares problem is complemented with these two conditions explicitly, ensuring that the final impedance profile is compliant. The optimization problem becomes

$$\begin{aligned} &\min_{\mathsf{z}\,\in\,\mathbb{C}^L} \, \|\mathsf{C}\mathsf{z} - \mathsf{V}_{\text{tot}}\|^2 \\ \text{s.t.} \quad &\operatorname{Re} z_\ell = 0, \qquad\qquad \forall \ell = 1, \ldots, L \\ &X_{\text{L}} \leq \operatorname{Im} z_\ell \leq X_{\text{U}}, \quad \forall \ell = 1, \ldots, L \end{aligned} \tag{3.112}$$

which is a convex problem that can be efficiently solved with available specialized softwares, e.g., CVX [48].

Of course, one can choose to test (3.110) with a different set of P testing functions $\boldsymbol{\tau}_p$, and the related linear system is obtained by premultiplying both sides of (3.110) by the change of basis matrix $\mathbf{BG}^{-1}$,

$$\mathbf{BG}^{-1}\mathbf{C}\mathsf{z} = \mathbf{BG}^{-1}\mathsf{V}_{\mathrm{tot}}, \tag{3.113}$$

where

$$(\mathbf{B})_{pm} = \langle\, \boldsymbol{\tau}_p \,, \boldsymbol{\Lambda}_m \,\rangle. \tag{3.114}$$

The inverse of the Gram matrix $\mathbf{G}$ (3.48) is needed since the RWG basis functions are not orthonormal. The least-squares problem becomes

$$\mathsf{z}^{\star} = \operatorname*{arg\,min}_{\mathsf{z}\in\mathbb{C}^L} \left\|\mathbf{BG}^{-1}(\mathbf{C}\mathsf{z} - \mathsf{V}_{\mathrm{tot}})\right\|^2, \tag{3.115}$$

which is the general formulation for finding an impedance profile which minimizes the error in the EFIE-IBC equation, with arbitrary basis and testing functions.

In the following, the impedance is expanded as a linear combination of piece-wise constant basis functions

$$\psi_\ell(\boldsymbol{r}) = \mathbb{I}_\ell(\boldsymbol{r}) = \begin{cases} 1, & \text{for } \boldsymbol{r} \in \mathcal{S}_\ell \\ 0, & \text{elsewhere} \end{cases} \tag{3.116}$$

with $L = N_{\mathrm{c}}$ and the shorthand notation $\mathbb{I}_\ell = \mathbb{I}_{\mathcal{S}_\ell}$ is used. A relevant case of the minimization problem (3.115) is that in which the testing functions are chosen equal to the conjugate of the current over each individual cell:

$$\boldsymbol{\tau}_p(\boldsymbol{r}) = \mathbb{I}_p(\boldsymbol{r})\boldsymbol{J}^*(\boldsymbol{r}) = \begin{cases} \boldsymbol{J}^*(\boldsymbol{r}), & \text{for } \boldsymbol{r} \in \mathcal{S}_p \\ \mathbf{0}, & \text{elsewhere} \end{cases} \tag{3.117}$$

where $\boldsymbol{J} = \sum_n I_n \boldsymbol{\Lambda}_n(\boldsymbol{r})$ and $P = N_{\mathrm{c}}$. In this case, the system (3.113) is diagonal and square,

$$(\mathbf{C}')_{pp}\, z_p = (\mathsf{V}'_{\mathrm{tot}})_p, \quad p = 1, \dots, N_{\mathrm{c}} \tag{3.118}$$

where $\mathbf{C}' = \mathbf{BG}^{-1}\mathbf{C}$ and $\mathsf{V}'_{\mathrm{tot}} = \mathbf{BG}^{-1}\mathsf{V}_{\mathrm{tot}}$. The solution is easily found to be

$$z_p = \frac{(\mathsf{V}'_{\mathrm{tot}})_p}{(\mathbf{C}')_{pp}} = \frac{\langle\, \boldsymbol{E} \,, \mathbb{I}_p \boldsymbol{J}^* \,\rangle}{\langle\, \mathbb{I}_p \boldsymbol{J} \,, \mathbb{I}_p \boldsymbol{J}^* \,\rangle} = \frac{\mathsf{I}^{\mathsf{H}}\boldsymbol{\Gamma}_p\mathbf{G}^{-1}\mathsf{V}_{\mathrm{tot}}}{\mathsf{I}^{\mathsf{H}}\boldsymbol{\Gamma}_p\mathsf{I}}, \quad p = 1, \dots, N_{\mathrm{c}}. \tag{3.119}$$

In this case, conditions (3.1) and (3.2) can be directly enforced by neglecting the real part of the computed impedance, and clipping the reactance value if it is outside the prescribed bounds. Eq. (3.119) can be given a variational interpretation: beginning with the least-squares minimization of the error in the defining EFIE-IBC equation,

$$\mathsf{z}^{\star} = \underset{\mathsf{z}\,\in\,\mathbb{C}^{L}}{\arg\min} \left\|\boldsymbol{E} - Z(\mathsf{z})\boldsymbol{J}\right\|^{2}, \tag{3.120}$$

where the impedance $Z(\boldsymbol{r})$ is expanded with piece-wise constant basis functions (3.116). The cells $\mathcal{S}_i$ have non overlapping support, so that, for a function $\boldsymbol{f}(\boldsymbol{r})$,

$$\left\|\boldsymbol{f}\right\|^{2} = \sum_{i=1}^{N_{\mathrm{c}}} \left\|\mathbb{I}_i \boldsymbol{f}\right\|^{2}. \tag{3.121}$$

Moreover, given the choice of pulse basis functions (3.116), a single z_i is involved in each cell, which simplifies the minimization instance (3.120) into a system of decoupled cell-wise minimization problems:

$$z_i^{\star} = \underset{z_i\,\in\,\mathbb{C}}{\arg\min} \left\|\mathbb{I}_i(\boldsymbol{E} - z_i\boldsymbol{J})\right\|^{2}, \quad \forall i = 1, ..., N_{\mathrm{c}}. \tag{3.122}$$

The optimum $z_i^{\star}$ for each coefficient is found by looking at the stationary point of (3.122) with respect to the real and imaginary parts of $z_i = z_i' + \mathrm{j}z_i''$. The error functional can be expressed as

$$\begin{aligned} \left\|\mathbb{I}_i(\boldsymbol{E} - z_i\boldsymbol{J})\right\|^{2} &= \langle\, \boldsymbol{E} - z_i\boldsymbol{J} \,, \mathbb{I}_i(\boldsymbol{E}_{\mathrm{tan}}^{*} - z_i^{*}\boldsymbol{J}^{*})\,\rangle \\ &= \left\|\mathbb{I}_i\boldsymbol{E}\right\|^{2} - 2z_i' \,\mathrm{Re}\langle\, \boldsymbol{E} \,, \mathbb{I}_i\boldsymbol{J}^{*}\,\rangle \\ &\quad - 2z_i''\,\mathrm{Im}\langle\, \boldsymbol{E} \,, \mathbb{I}_i\boldsymbol{J}^{*}\,\rangle + (z_i'^{2} + z_i''^{2}) \left\|\mathbb{I}_i\boldsymbol{J}\right\|^{2}, \end{aligned} \tag{3.123}$$

and the partial derivatives with respect to the real and imaginary parts of the impedance are given by

$$\frac{\partial}{\partial z_i'} \left\|\mathbb{I}_i(\boldsymbol{E} - z_i\boldsymbol{J})\right\|^{2} = -2\,\mathrm{Re}\langle\, \boldsymbol{E} \,, \mathbb{I}_i\boldsymbol{J}^{*}\,\rangle + 2z_i' \left\|\mathbb{I}_i\boldsymbol{J}\right\|^{2}, \tag{3.124}$$

$$\frac{\partial}{\partial z_i''} \left\|\mathbb{I}_i(\boldsymbol{E} - z_i\boldsymbol{J})\right\|^{2} = -2\,\mathrm{Im}\langle\, \boldsymbol{E} \,, \mathbb{I}_i\boldsymbol{J}^{*}\,\rangle + 2z_i'' \left\|\mathbb{I}_i\boldsymbol{J}\right\|^{2}. \tag{3.125}$$

Setting both derivatives to zero yields

$$z_i'^{\star} = \frac{\mathrm{Re}\langle\, \boldsymbol{E}\,, \mathbb{I}_i \boldsymbol{J}^*\,\rangle}{\|\mathbb{I}_i \boldsymbol{J}\|^2}, \tag{3.126}$$

$$z_i''^{\star} = \frac{\mathrm{Im}\langle\, \boldsymbol{E}\,, \mathbb{I}_i \boldsymbol{J}^*\,\rangle}{\|\mathbb{I}_i \boldsymbol{J}\|^2}. \tag{3.127}$$

Putting all together, the final expression is identical to (3.119):

$$z_i^{\star} = z_i'^{\star} + \mathrm{j} z_i''^{\star} = \frac{\langle\, \boldsymbol{E}\,, \mathbb{I}_i \boldsymbol{J}^*\,\rangle}{\|\mathbb{I}_i \boldsymbol{J}\|^2} = \frac{\mathsf{I}^{\mathsf{H}} \boldsymbol{\Gamma}_i \mathbf{G}^{-1} \mathsf{V}_{\mathrm{tot}}}{\mathsf{I}^{\mathsf{H}} \boldsymbol{\Gamma}_i \mathsf{I}}. \tag{3.128}$$

This stationary point does indeed correspond to a minimum, as follows from the evaluation of the Hessian matrix,

$$\mathbf{H} = \begin{bmatrix} 2\,\|\mathbb{I}_i \boldsymbol{J}\|^2 & 0 \\ 0 & 2\,\|\mathbb{I}_i \boldsymbol{J}\|^2 \end{bmatrix}, \tag{3.129}$$

which is positive definite.

3.5.1 Impedance regularization

In computing the impedance values by the method outlined in the previous section, sensitivity may arise, as the computation involves the ratio of the electric field $\boldsymbol{E}$ and the current $\boldsymbol{J}$. Different combinations of limiting cases are possible: when $\boldsymbol{E}$ in (2.18) is zero and the current $\boldsymbol{J}$ is not, the surface corresponds to a PEC boundary condition (equivalent to $Z = 0$). When the current $\boldsymbol{J}$ is zero and the field $\boldsymbol{E}$ is not, it coincides with an open circuit condition ($Z = \infty$), which implies that there is *no* IBC there (i.e., only the dieletric substrate). This last condition can be easily implemented numerically by removing the corresponding degrees of freedom from the discretization. Finally, when both the field and the current are zero, the impedance is not defined and thus will be obtained by interpolating nearby values. All these cases are summarized in Tab. 3.3.

Table 3.3 Summary of all possible cases in the reconstruction of impedance values.

	$\lvert\boldsymbol{J}\rvert = 0$	$\lvert\boldsymbol{J}\rvert \neq 0$
$\lvert\boldsymbol{E}\rvert = 0$	undefined	$Z = 0$
$\lvert\boldsymbol{E}\rvert \neq 0$	open circuit	$Z = \boldsymbol{E}/\boldsymbol{J}$

In practice, this regularization step is done by setting thresholds τ_I and τ_V for the current and field values, which define how small the quantities must be in order to be considered negligible. The whole process is described in algorithmic form in Algorithm 4.

Algorithm 4 Impedance profile computation

```
Input: $\mathsf{I}, \mathsf{V} = \mathbf{G}^{-1}\mathsf{V}_{\mathrm{tot}}, \tau_I, \tau_V$
Output: $\mathsf{z}$
  for $i = 1, \ldots, N_{\mathrm{c}}$ do
      $|I|_i \leftarrow \mathsf{I}^{\mathsf{H}}\boldsymbol{\Gamma}_i\mathsf{I}$
      $|V|_i \leftarrow \mathsf{V}^{\mathsf{H}}\boldsymbol{\Gamma}_i\mathsf{V}$
      if $|I|_i < \tau_I$ then
          if $|V|_i < \tau_V$ then                                ▷ Don't care
              Interpolate $z_i$ from nearby values
          else                                                    ▷ Open circuit
              Remove cell from mesh
          end if
      else
          $z_i = \dfrac{\mathsf{I}^{\mathsf{H}}\boldsymbol{\Gamma}_i\mathsf{V}}{\mathsf{I}^{\mathsf{H}}\boldsymbol{\Gamma}_i\mathsf{I}}$
      end if
  end for
```

Sensitivity may still be present in the impedance computation due to the current at the denominator of (3.119), or in the subsequent solution of the forward problem because current and impedance appear as a product in (2.29). Handling the above limiting cases avoids most of the problems, but more sophisticated regularization processes may be necessary to yield smoother profiles.

Chapter 4

Numerical results

This chapter presents a series of design cases obtained using the presented method. Preliminarily, the setup is illustrated: the background medium and the source (incident) field are defined, the optimization parameters are listed and the validation procedure is explained. Then, designs for different combinations of geometries and field specifications are shown and, for each of them, the current and impedance profile, along with the realized gain patterns, are reported.

4.1 Setup

Background medium In all cases, the considered supporting structure is a single-layer grounded dielectric slab with $\varepsilon_\mathrm{r} = 3$ and height $h = 0.76\,\mathrm{mm}$ (see Fig. 3.2b for reference); the dielectric layer and the ground plane extend infinitely in the x-y plane. This approximation is commonly used in the design of printed antennas and is needed for the use of fast numerical methods, introduced in Sec. 2.3.1. The design frequency is $32\,\mathrm{GHz}$.

Source field The source field is generated by a (short) centered vertical dipole, and approximated with its asymptotic form as a TM_0 cylindrical surface wave (as in, e.g., [28]). The analytic expression of this field can be obtained by a TE/TM decomposition and matching of the boundary conditions at the ground plane and at the air-dielectric interface. The resulting tangential electric field of the TM_0 surface wave mode is

$$\left[\boldsymbol{E}_{\mathrm{inc}}(\rho,\varphi)\right]_{\tan} = E_0\,\mathrm{H}_1^{(2)}(\beta_{\mathrm{sw}}\rho)\hat{\boldsymbol{\rho}}, \tag{4.1}$$

where E_0 is the amplitude constant, chosen such that the incident power is normalized to $1\,\mathrm{W}$ (see App. A.4), $\mathrm{H}_1^{(2)}$ is the Hankel function of the second kind of order 1 and the propagation constant β_{sw} is the solution of the dispersion equation

$$\begin{cases} \alpha_z\,\varepsilon_{\mathrm{r}} = \beta_z \tan(\beta_z h) \\ \alpha_z = \sqrt{\beta_{\mathrm{sw}}^2 - k_0^2} \\ \beta_z = \sqrt{k_0^2\varepsilon_{\mathrm{r}} - \beta_{\mathrm{sw}}^2} \end{cases} \tag{4.2}$$

where β_z is the transverse propagation constant in the dielectric, and α_z is the transverse attenuation constant in air.

Impedance constraints In the following, the requirement is for the impedance to be *scalar*, with explicit enforcement through the term introduced in Sec. 3.4.1. Moreover, the allowed reactance is capacitive-only (which greatly simplifies the design of unit cells by means of printed patches), with values in the range from $-600\,\Omega$ to $-100\,\Omega$, as dictated by physical and numerical motivations (see Sec. 2.3.2).

Field specifications The field specifications are enforced by sampling the field on a regular grid of 40×40 points in the u-v space, as shown in Fig. 4.1a. The mask requirements are consequently defined on the same grid (Fig. 4.1b). The choice of a u-v grid, instead of a spherical one, is motivated by the fact that a spherical grid has an higher density of sampling points near the broadside direction, and this would cause a bias in the cost functional for the field. The adopted grid guarantees that the considered points are (more) uniformly distributed on the spherical upper surface. All reported examples incorporate the requirement of gain maximization in the main beam. This is achieved by considering a value of M_0 (Sec. 3.4.2) equal to the field magnitude that would be radiated by an antenna with 100% efficiency in the main beam region, which corresponds to a physical upper limit for the antenna. The co-polarization region Ω_{ML} is set to the desired $3\,\mathrm{dB}$ beam-width and, trivially, its relative level is $\mu_{\mathrm{L}}^{\mathrm{co}} = -3\,\mathrm{dB}$ with respect to F_{ref}.

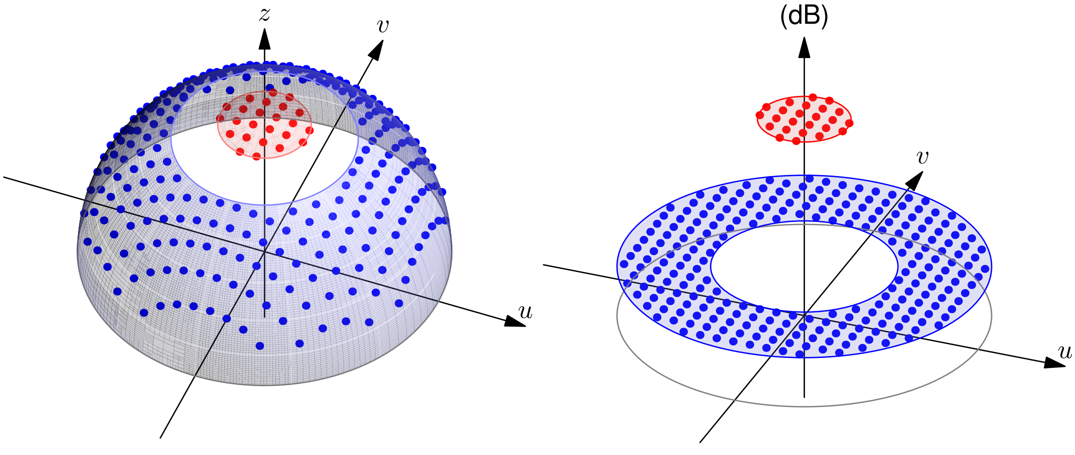

(a) (b)

Fig. 4.1 Example of a pattern mask with Ω_{ML} (red) and Ω_{SL} (blue): (a) sample on a regular u-v grid represented on the upper half hemisphere, (b) mask levels for the same samples.

Optimization parameters The weights for the various components of the objective function were set by experimentation. The values are reported in Table 4.1 for all the presented designs; since each component has a different normalization, this reflects in a variation of the order of magnitude for the weights. The algorithm was stopped on stagnation, and the number of iterations was in all cases limited to 500.

Validation It is important to recall that the optimization process avoids the solution of the forward problem (2.29); this fact can be used to verify the consistency and stability of the obtained impedance profile. The procedure, outlined in Fig. 4.2, is the following: from the optimized current $\mathsf{I}^{\star}$, the impedance profile $Z(\boldsymbol{r})$ is determined by computing the values for each cell with (3.128), keeping only its imaginary part, and applying the regularization procedure in Sec. 3.5.1, where thresholds for currents and fields have been set to 3% of their maximum value. Next, a new current is computed by solving the forward problem (2.29) for this impedance profile and the specified source field. All the radiation patterns shown in this chapter have been obtained this way; hence, the results take into account a possible efficiency reduction due to the impedance reconstruction process. In order to assess the effect of the impedance computation step, the co-polar component of the field radiated by the optimized current will also be reported.

Table 4.1 Weights for the components of the objective function.

Antenna	Pattern	w_{act}	w_{rct}	w_{scal}	w_{ML}	w_{SL}
circular, $6\lambda_0$	pencil, circ. pol.	1	0.1	1	10^{-15}	10^{-15}
	pencil, lin. pol.	1	0.5	1	10^{-16}	10^{-16}
	squinted, lin. pol.	1	0.1	1	10^{-12}	10^{-12}
circular, $10\lambda_0$	pencil, circ. pol.	1	0.1	1	10^{-15}	10^{-15}
	pencil, lin. pol.	1	0.1	1	10^{-15}	10^{-15}
	flat-top, lin. pol.	1	0.1	1	10^{-15}	10^{-15}
elliptical	pencil, circ. pol.	1	0.01	0.1	10^{-15}	10^{-15}
symmetric strip	pencil, lin. pol.	1	10^{-3}	10^{-3}	10^{-16}	10^{-16}

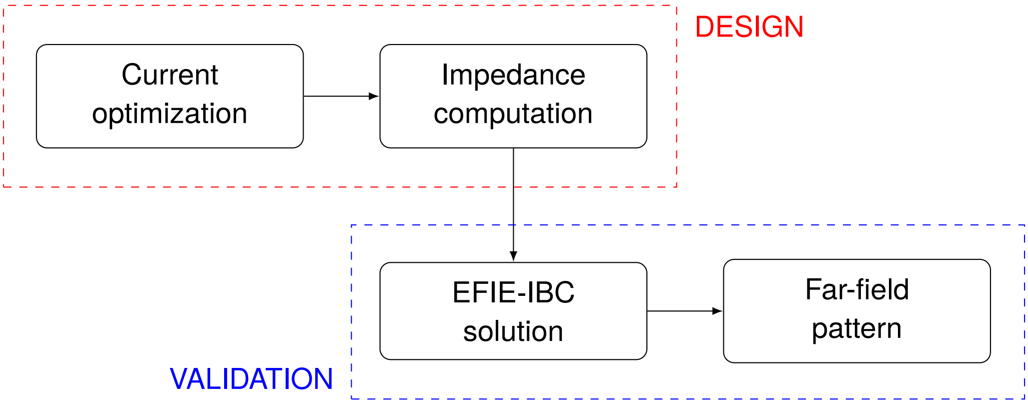

Fig. 4.2 Flowchart of the design and validation process.

Radiation performance In the following, radiation results will be given in terms of the realized gain, as explained in Sec. 3.4.2; losses in the conductors and the dielectric substrate are not considered. The post-processing of results also includes the computation of the total radiated power, P_{rad}; the *total radiation efficiency* $e_0 = P_{\text{rad}}/P_{\text{inc}} \leq 1$ allows to compute also the directivity (which will be larger or equal to the realized gain). The aperture efficiency, defined as

$$e_{\text{ap}} = \frac{A_{\text{eff}}}{A_{\text{phy}}}, \quad \text{where } A_{\text{eff}} = D_{\text{max}}\,\frac{\lambda_0^2}{4\pi}, \tag{4.3}$$

will also be reported in the relevant cases (e.g., for pencil beam antennas); A_{phy} is the physical aperture area, while A_{eff} is the effective one and D_{max} is the maximum directivity. Each far field pattern is shown along with the corresponding mask specifications. Consistent with the example in Fig. 3.4, green lines represent the main lobe co-polarization mask, red lines correspond to the cross-polarization mask and blue lines to the side lobe masks. The dotted line identifies the reference level for each case, and the arrows denote relative quantities.

4.2 Circular Metasurface

As the first application, the design method has been applied to the case of a circular metasurface antenna. This shape was chosen for its practical relevance and prevalence in the literature. As common, the metasurface has a hole in the center to host the feed.

Two geometries are considered: a medium-sized antenna with a diameter $D = 6\lambda_0$ ($\lambda_0 = c/f$), shown in Fig. 4.3a, and a large one with a diameter $D = 10\lambda_0$ (Fig. 4.3b). The former involves $N_{\text{c}} = 16\,206$ degrees of freedom for the impedance, with $N = 24\,046$ RWG basis functions, while the latter has $N_{\text{c}} = 23\,616$ and $N = 35\,241$.

The current is initialized to an everywhere $\hat{\boldsymbol{y}}$-directed current with a raised-cosine radial profile with roll-off toward the inner and outer edges (Fig. 4.4). This current radiates *broadside* with *linear polarization*, and is (obviously) not realizable with a passive lossless metasurface. It will be used as the starting current even when seeking to design a squinted beam and/or for circular polarization, as this will allow to assess the robustness of the algorithm.

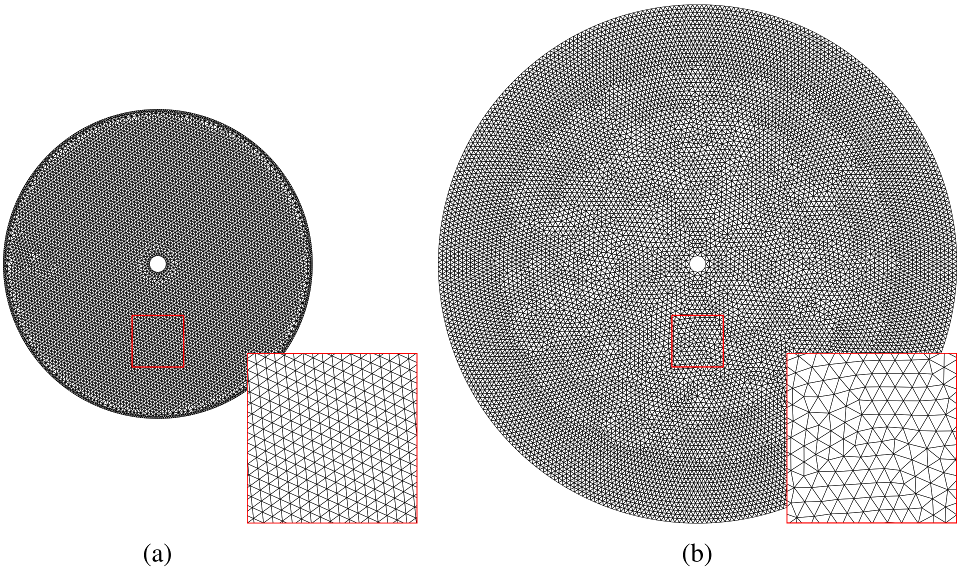
(a) (b)

Fig. 4.3 Surface mesh for the circular metasurface antenna: (a) medium-sized antenna with $D = 6\lambda_0$; (b) large antenna with $D = 10\lambda_0$. The two figures are drawn to scale.

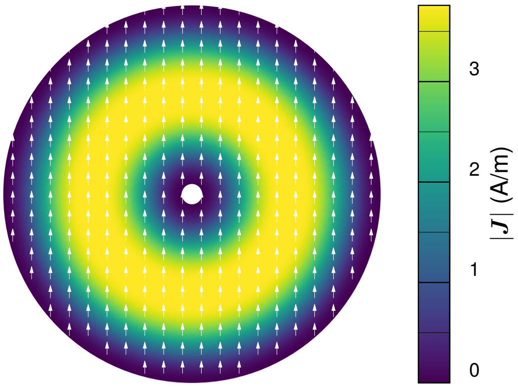

Fig. 4.4 Initial current for the design of circular metasurfaces. Arrows represent the direction of the current.

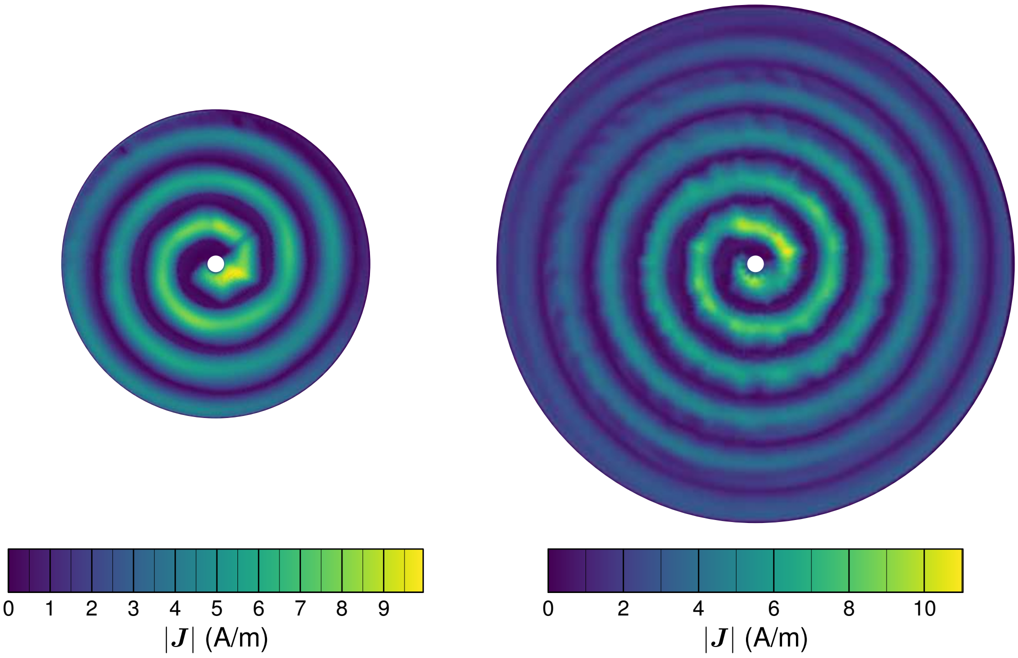

(a) (b)

Fig. 4.5 Pencil beam with circular polarization: optimized surface current magnitude for (a) $D = 6\lambda_0$ (b) $D = 10\lambda_0$.

4.2.1 Pencil beam, circular polarization

The first field specification for the circular antenna is a pencil beam pattern with circular polarization, as this is one of the most researched configurations. For both antenna sizes, the reference level has been considered as the field value in the broadside direction, i.e., $F_{\text{ref}} = F(\theta = 0°)$, but all other specifications differ between the two. In particular, for the antenna with $D = 6\lambda_0$, the main lobe region Ω_{ML} goes from $\theta = -5°$ to $5°$, with a cross-pol relative level $\sigma_{\text{cx}} = -15\,\text{dB}$, while the side lobes mask Ω_{SL} starts from $\theta = 20°$, with a required relative level of $\sigma_{\text{SL}} = -20\,\text{dB}$. The output of the optimization is the current in Fig. 4.5a, and the corresponding impedance is shown in Fig. 4.6a. Here, and in the following, white areas in the impedance plot correspond to the absence of IBC. Fig. 4.7a shows the requirement masks (with azimuthal symmetry) along with the obtained pattern in the plane cut $\varphi = 90°$. A 3D view of the same pattern in the u-v plane is given in Fig. 4.7b. In this case, the realized gain is of $19\,\text{dB}$, with a directivity of $21\,\text{dB}$ and an aperture efficiency of 37%.

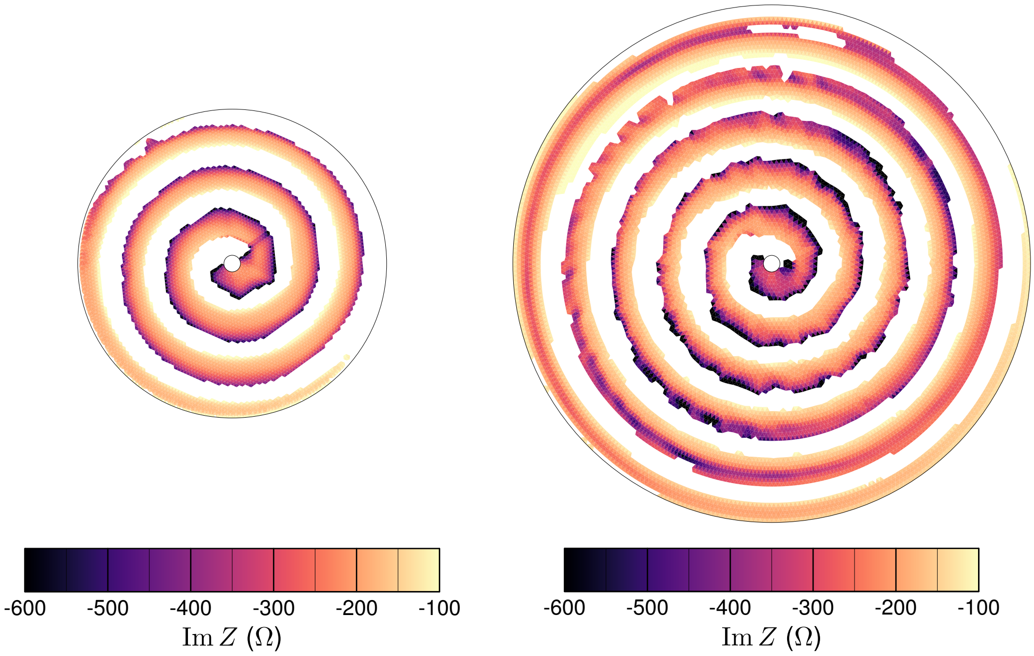

(a) (b)

Fig. 4.6 Pencil beam with circular polarization: resulting surface reactance for (a) $D = 6\lambda_0$ (b) $D = 10\lambda_0$.

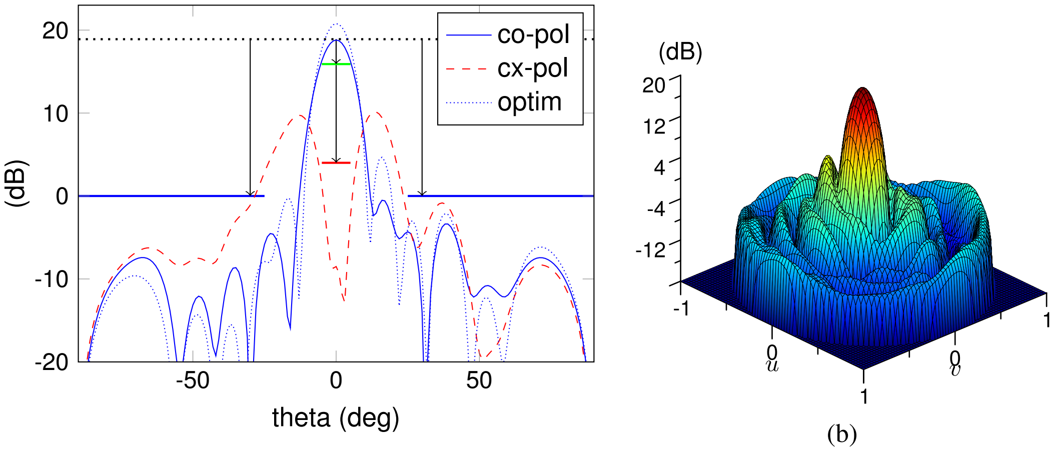

(a) (b)

Fig. 4.7 Pencil beam pattern with circular polarization, antenna with $D = 6\lambda_0$: (a)mask requirements and realized gain in the plane cut $\varphi = 90°$, (b) realized gain in the u-v plane.

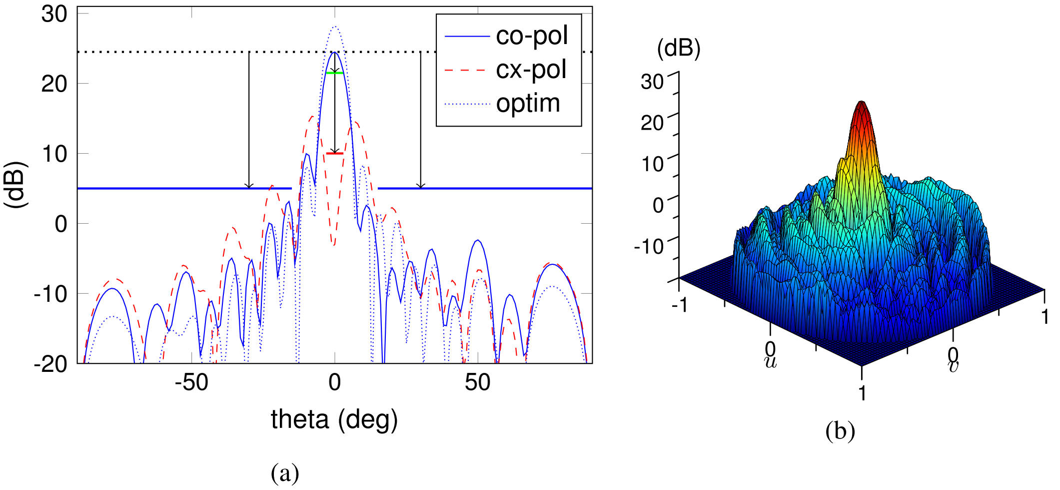

(a)

(b)

Fig. 4.8 Pencil beam pattern with circular polarization, antenna with for $D = 10\lambda_0$: (a) mask requirements and realized gain in the plane cut $\varphi = 90°$, (b) realized gain in the u-v plane.

For the same case of circular polarization, the large antenna with $D = 10\lambda_0$ has been designed with the following specifications: the main lobe region Ω_{ML} goes from $\theta = -3°$ to $3°$, with $\sigma_{\text{cx}} = -15\,\text{dB}$, while the side lobes requirements go from $\theta = 15°$, with $\sigma_{\text{SL}} = -20\,\text{dB}$. The optimized current and the impedance are shown in Figs. 4.5b and 4.6b, respectively. The resulting radiation pattern are given in Fig. 4.8a and 4.8b. The achieved realized gain is of $24.5\,\text{dB}$, with a directivity of $25.5\,\text{dB}$ and a resulting aperture efficiency of 35%.

As it can be noted, in both cases the current shows some “streaks” that can be attributed to the absence of any regularization (as anticipated in Sec. 3.5.1). As a consequence, the impedance profile shows some jigsaw (which would be anyway smoothed out in the unit cell layout process); however, this does not impact on radiation and overall performances.

It is remarkable that the proposed optimization algorithm reaches the same spiral shape that was devised in [7] based on analytical considerations; the proposed algorithm employs no assumption, and actually reaches this spiral shape and circular polarization starting from a constant current with linear polarization. The achieved directivity of $\approx 20\,\text{dB}$ for the medium-sized antenna compares well with the case in [7], that also employed a scalar impedance for the design of a spiral modulated metasurface antenna with a diameter of $7.3\lambda_0$ (here it is $6\lambda_0$).

4.2.2 Pencil beam, linear polarization

In the next case, the specifications are for a broadside radiation with linear polarization, which is less usual for the considered type of antenna. The reference level is still equal to the field magnitude value in the broadside direction, as it was for the previous case. The main lobe region Ω_{ML} for the medium-sized antenna extends from $\theta = -5°$ to $5°$, with side lobe masks Ω_{SL} from $\theta = 20°$, as for the circular polarization case. The required relative levels are $\sigma_{\mathrm{cx}} = \sigma_{\mathrm{SL}} = -20\,\mathrm{dB}$.

The optimized current in is Fig. 4.9, and the resulting reactance in Fig. 4.10. As in the case of circular polarization, there are "streaks" of limited entity in the current, attributed to absence of smoothing regularization. The (axi-symmetric) mask specifications are indicated in Fig. 4.11a along with the obtained radiated field. In this case the directivity is $20.9\,\mathrm{dB}$, while the realized gain is $14.8\,\mathrm{dB}$. The aperture efficiency is 35%.

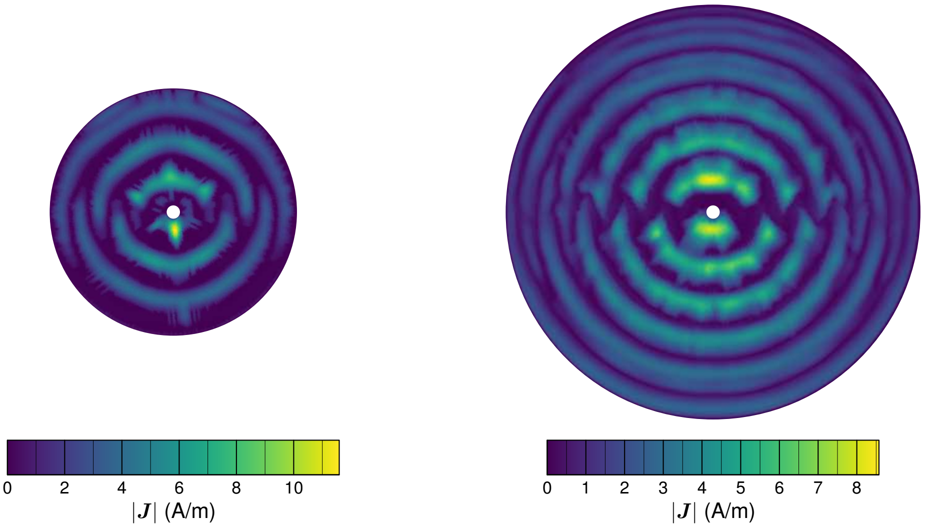

(a)

(b)

Fig. 4.9 Pencil beam with linear polarization: optimized surface current magnitude for (a) antenna with $D = 6\lambda_0$, (b) antenna with $D = 10\lambda_0$.

The pattern requirements for the large antenna are as follows: Ω_{ML} from $\theta = -3°$ to $3°$, Ω_{SL} from $\theta = 20°$, with $\sigma_{\mathrm{cx}} = \sigma_{\mathrm{SL}} = -20\,\mathrm{dB}$. The results are reported in Figs. 4.9b, 4.10b and 4.12b. As it can be seen, the impedance pattern remains as in the medium-sized case. The directivity reaches $26\,\mathrm{dB}$, with a corresponding realized gain of $23.2\,\mathrm{dB}$ and aperture efficiency of 40%. Side-lobe performance

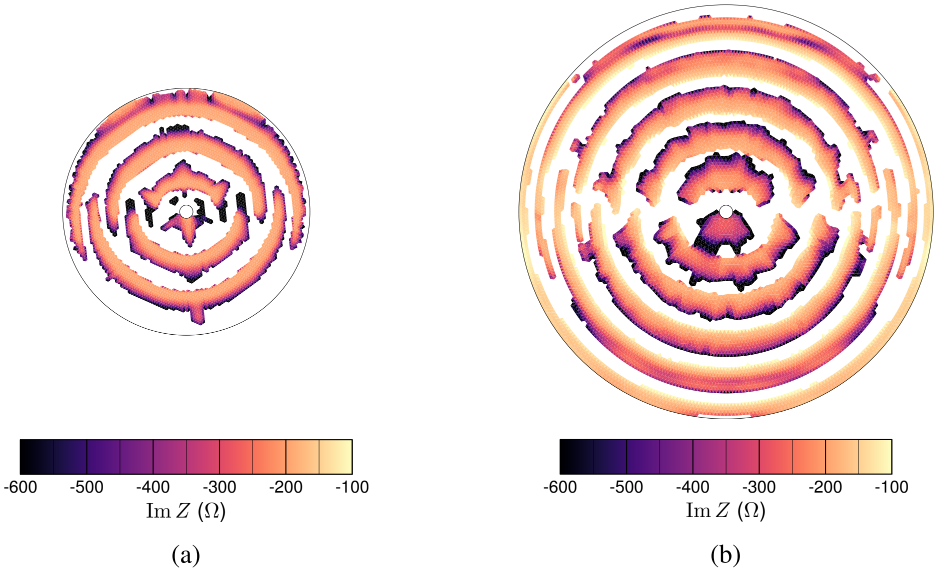

Fig. 4.10 Pencil beam with linear polarization: resulting surface reactance for (a) antenna with $D = 6\lambda_0$, (b) antenna with $D = 10\lambda_0$.

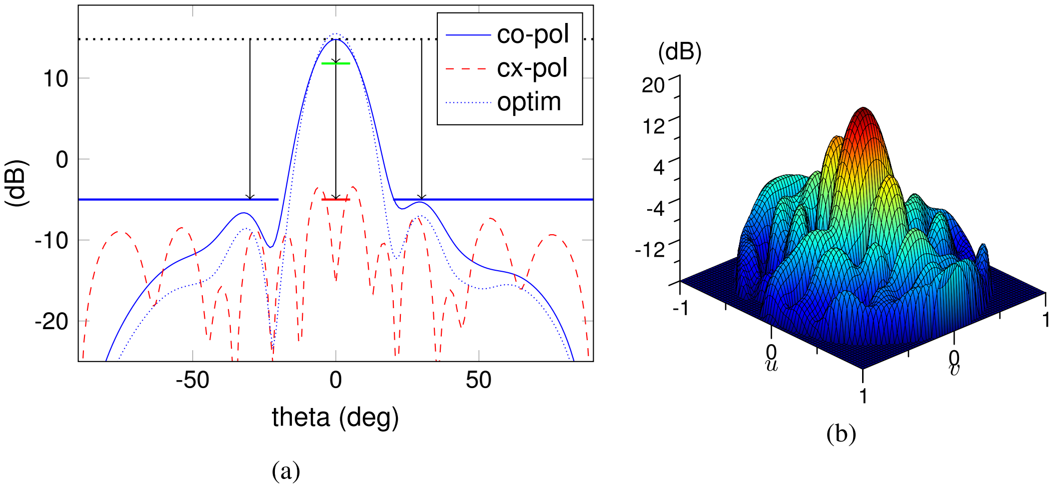

Fig. 4.11 Pencil beam pattern with linear polarization, antenna with $D = 6\lambda_0$: (a) mask requirements and realized gain in the plane cut $\varphi = 90°$, (b) realized gain in the u-v plane.

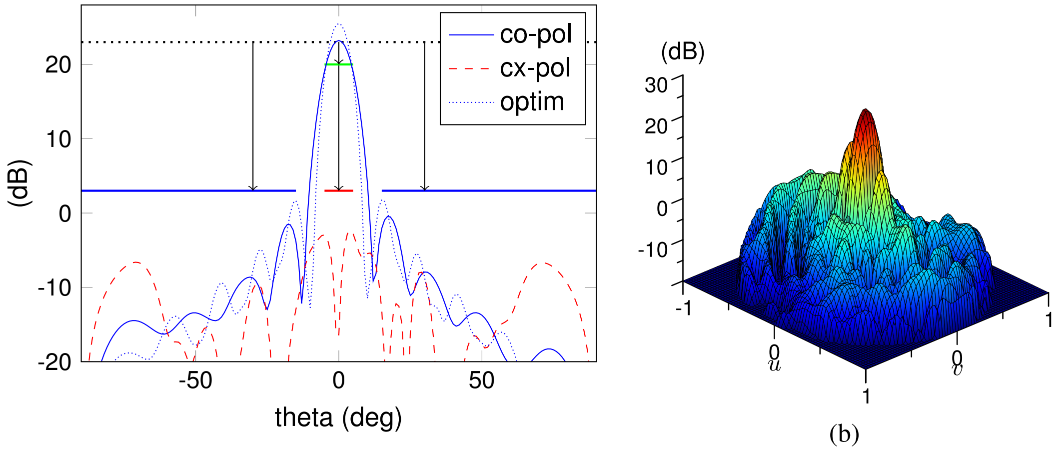

(a)

(b)

Fig. 4.12 Pencil beam pattern with linear polarization, antenna with $D = 10\lambda_0$: (a) mask requirements and realized gain in the plane cut $\varphi = 90°$, (b) realized gain in the u-v plane.

appear different in the E- and H-plane, and worse in the E-plane than for the circular polarization case: the difference can be attributed to the scalar impedance employed here.

Attempting to draw a comparison between these results and published ones is not easy, as most of the center-fed, broadside-radiating, linearly polarized metasurface antennas available in the literature have a predefined impedance pattern (e.g., [49]), as opposed to the "free-shape" impedance optimization used here. The impedance profile bears a resemblance with the one in [50], where it was obtained with holographic techniques. Similar to the circular polarization case, it is remarkable that the automated design recovers a shape determined on the basis of analytical wave-based considerations.

4.2.3 Squinted beam, linear polarization

The next considered configuration is a squinted beam pattern pointing at an angle $\theta_0 = 30°$, for the antenna with $D = 6\lambda_0$. In this case, the field specifications are not axially-symmetric: the reference level is $F_{\mathrm{ref}} = F(\theta = 30°, \varphi = 0°)$, the main lobe region Ω_{ML} extends $5°$ from both sides of the pointing direction, i.e., from $\theta = 25°$ to $35°$ in the plane $\varphi = 0°$, and the sidelobes constraints start $15°$ outside the main beam region in all directions. The required cross-pol and sidelobes relative levels are $\sigma_{\mathrm{cx}} = \sigma_{\mathrm{SL}} = -15\,\mathrm{dB}$.

The optimized current and impedance are illustrated in Figs. 4.13a and 4.13b, respectively. The resulting pattern and mask specifications are shown for the plane cut $\varphi = 90°$ (Fig. 4.14a) and with a top view of the u-v plane (Fig. 4.14b). The directivity is $18\,\mathrm{dB}$ and the realized gain is $14\,\mathrm{dB}$. It is important to recall that this squinted beam has been obtained with a starting current that radiates broadside.

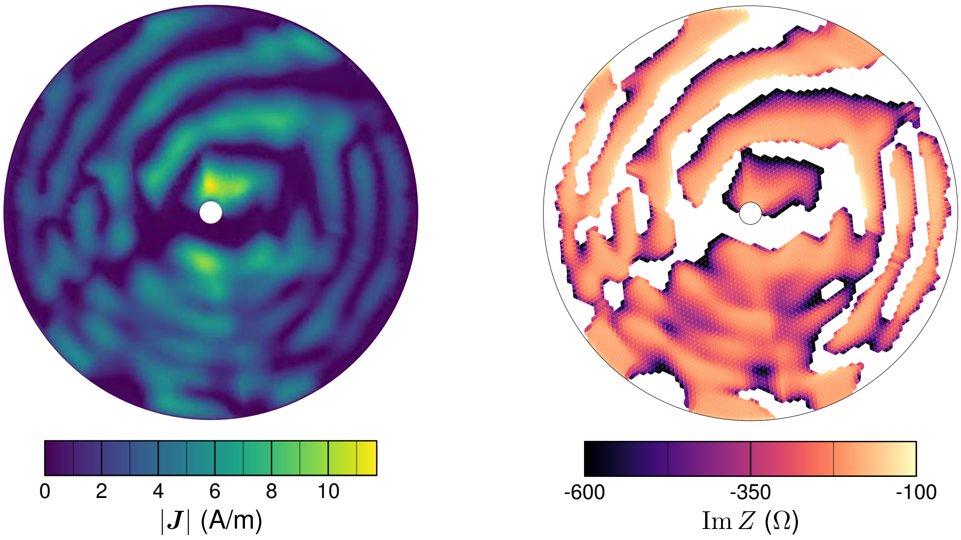

(a)

(b)

Fig. 4.13 Squinted beam pattern with linear polarization, antenna with $D = 6\lambda_0$: (a) optimized surface current magnitude, (b) resulting surface reactance.

4.2.4 Square flat-top, linear polarization

The last example for the circular metasurface involves a shaped-beam design for the antenna with $D = 10\lambda_0$. In particular, the aim is to obtain a square flat-top beam pattern (square in the u-v plane). The mask specifications are defined in the u-v coordinates: the main lobe region is defined by the square region $\Omega_{\mathrm{ML}} = [-0.15, 0.15] \times [-0.15, 0.15]$. The reference level in this case is given by the average of the field magnitude over the main lobe region, i.e., $F_{\mathrm{ref}} = (\sum_{j\in\mathrm{ML}} F_j)/N_{\mathrm{ML}}$. The maximum admissible ripple in the main beam region is $2\,\mathrm{dB}$, which implies $\mu_{\mathrm{L}}^{\mathrm{co}} = -1\,\mathrm{dB}$ and $\mu_{\mathrm{U}}^{\mathrm{co}} = 1\,\mathrm{dB}$. Cross-pol and side lobes relative levels are both required to be $\sigma_{\mathrm{cx}} = \sigma_{\mathrm{SL}} = -15\,\mathrm{dB}$.

Fig. 4.15a shows the optimized current magnitude, while Fig. 4.15b reports the computed impedance. The resulting pattern and mask specifications are shown in

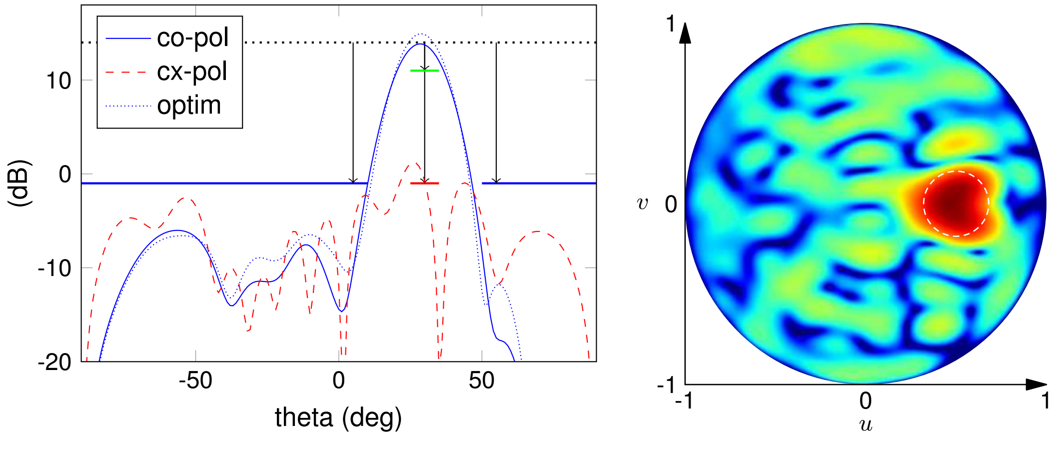

(a)

(b)

Fig. 4.14 Squinted beam pattern with linear polarization, antenna with $D = 6\lambda_0$: (a) mask requirements and realized gain in the plane cut $\varphi = 0°$, (b) top view of the pattern in the u-v plane.

Fig. 4.16a for the plane cut $\varphi = 90°$, and in Fig. 4.16b with a top view of the u-v plane with the main beam region highlighted. The average directivity over the main beam is $15\,\mathrm{dB}$ and the realized gain is $13\,\mathrm{dB}$.

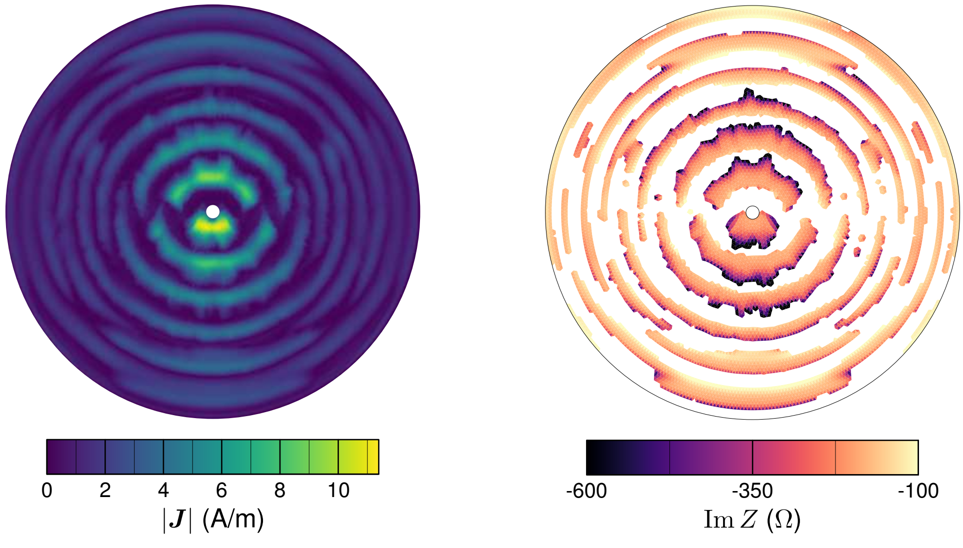

(a)

(b)

Fig. 4.15 Flat-top pattern with linear polarization, antenna with $D = 10\lambda_0$: (a) optimized surface current magnitude, (b) resulting surface reactance.

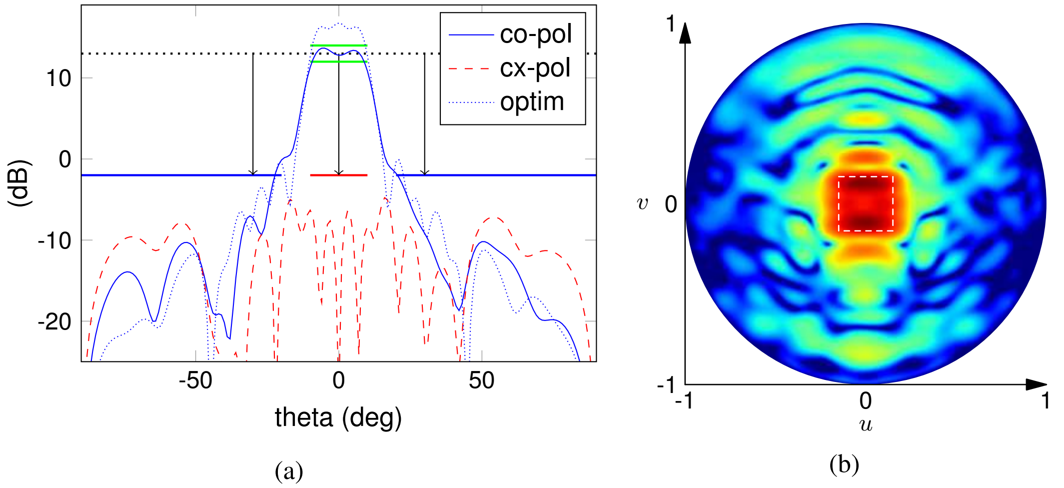

(a)

(b)

Fig. 4.16 Flat-top pattern with linear polarization, antenna with $D = 10\lambda_0$: (a) mask requirements and realized gain in the plane cut $\varphi = 90°$, (b) top view of the pattern in the u-v plane.

4.3 Elliptical Metasurface

The design is not limited to circular shapes. Another relevant class of metasurface antenna is constituted by elliptical ones [20]. The considered ellipse has a major axis $a = 7.4\lambda_0$ and a minor axis $b = 4.5\lambda_0$. The source is the same as for the circular case.

The chosen field specifications are for a pencil beam with circular polarization and axially symmetrical field mask: the reference level is $F_{\text{ref}} = F(\theta = 0°)$, the main lobe region Ω_{ML} extends from $\theta = -3°$ to $3°$, with side lobe masks Ω_{SL} from $\theta = 15°$. The required relative levels are $\sigma_{\text{cx}} = \sigma_{\text{SL}} = -15\,\text{dB}$.

The optimized current and impedance are illustrated in Figs. 4.17a and 4.17b, respectively. The resulting pattern and mask specifications are shown for the plane cut $\varphi = 90°$ (Fig. 4.18a) and with a 3D view of the u-v plane (Fig. 4.18b). The achieved directivity is $21.5\,\text{dB}$ and the realized gain is $19.8\,\text{dB}$, with an aperture efficiency of 26%. It is interesting to note that the impedance and current patterns resemble those of the circular metasurface, except that they are clipped to the ellipse boundary. This suggests that the shape of the surface has a relatively little influence on the impedance and current patterns, as these are mainly connected to the interaction with the incident field and to the desired radiation. This could also explain the lower directivity and decreased efficiency, compared to the circular case, as a circular polarization is most

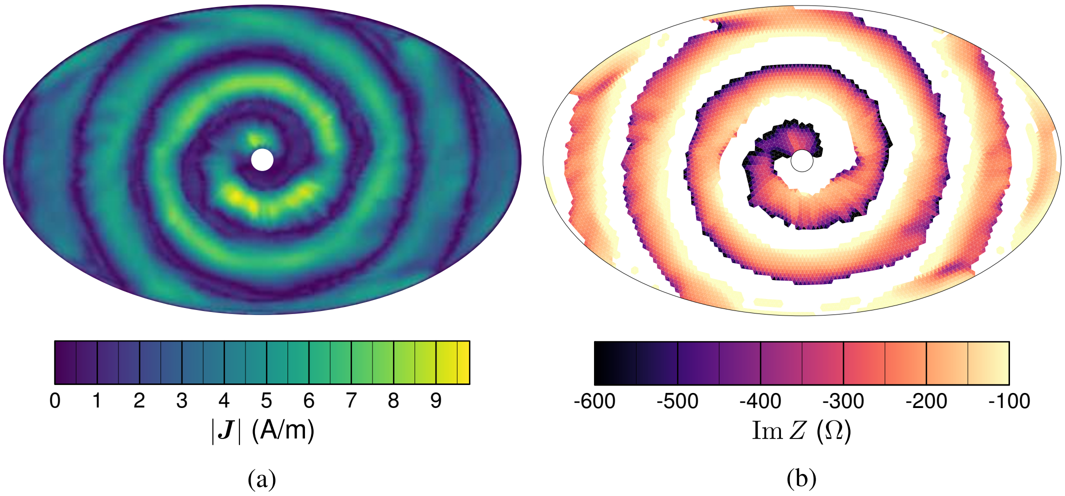

(a)

(b)

Fig. 4.17 Elliptical antenna with circular polarization: (a) optimized surface current magnitude, (b) resulting surface reactance.

effectively radiated by a surface that extends equally in all directions, having the same "symmetry" of the incident field.

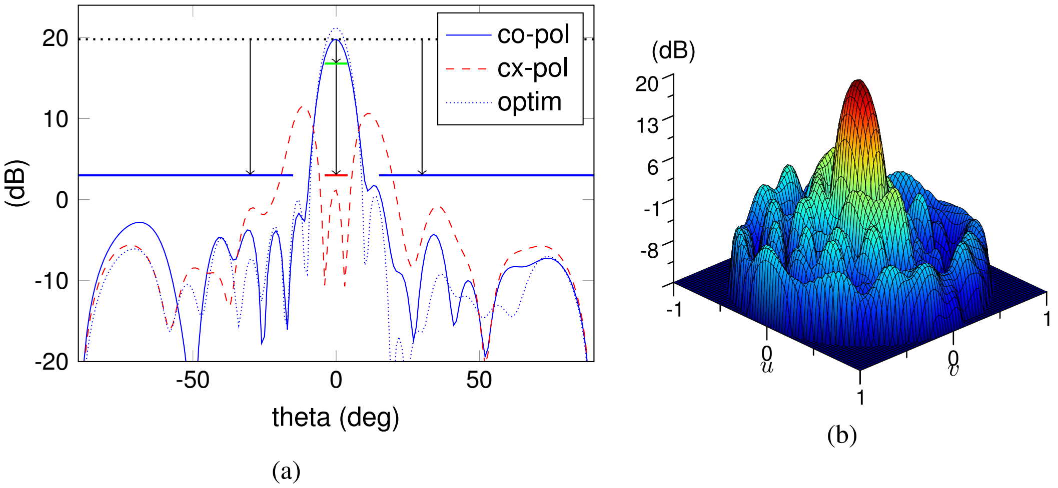

(a)

(b)

Fig. 4.18 Elliptical antenna with circular polarization: (a) mask requirements and realized gain in the plane cut $\varphi = 0°$, (b) 3D of the pattern in the u-v plane.

4.4 Symmetric Strip Antenna

To demonstrate the flexibility of the proposed method, it has been applied to design the impedance profile for a completely different geometry with respect to the rounded shapes considered so far: a symmetric strip antenna. The antenna is constituted by two symmetric strips of length of $5\lambda_0$ that extend on both sides of the center feed, with a width of $\lambda_0/4$; the employed triangular mesh has $N = 5\,948$ and $N_\mathrm{c} = 4\,148$ (see Fig. 4.19). For this case, the initial current was chosen as a constant current tapered toward the outer edges, polarized along the $\hat{\boldsymbol{x}}$ direction.

The target pattern has a broadside radiation, with $F_\mathrm{ref} = F(\theta = 0°)$, a main lobe Ω_ML that extends from $\theta = -3°$ to $3°$, and sidelobes region Ω_SL beginning at $\theta = 10°$. For this desing, $\sigma_\mathrm{cx} = \sigma_\mathrm{SL} = -15\,\mathrm{dB}$. The pattern requirements have been enforced only on the plane $\varphi = 0°$, with $\theta = [-90°, 90°]$, the reason being that the antenna has a sub-wavelength size in the transverse direction, therefore it radiates a predictable cosine-like pattern in the orthogonal plane which does not require control. The weight of the f_rad component has been adjusted accordingly, reaching a balance between the different optimization terms.

The final optimized current is shown in Fig. 4.20a. The corresponding resulting impedance, displayed in Fig. 4.20b, alternates areas with a sawtooth-like behaviour and open circuit sections (see Fig. 4.20c for a cut view along the x axis). Given the geometry of the strip antenna and its radiation pattern, one can draw similarities with broadside radiating 1D leaky-wave antennas [51, 52]. However, the present work is full-wave, and does not rely on analytical expansions for the fields typical of leaky-wave analysis.

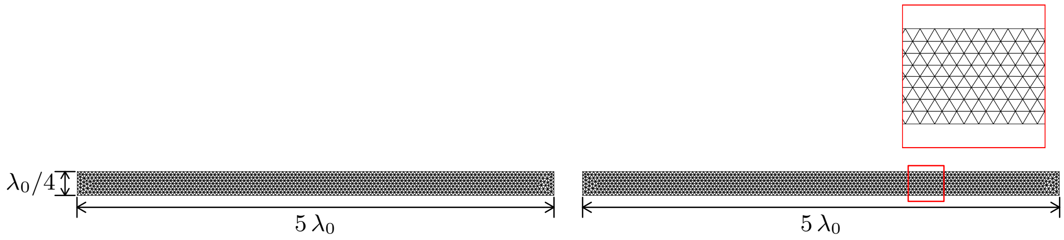

Fig. 4.19 Mesh for the symmetric strip antenna. The source is placed in the gap between the two strips.

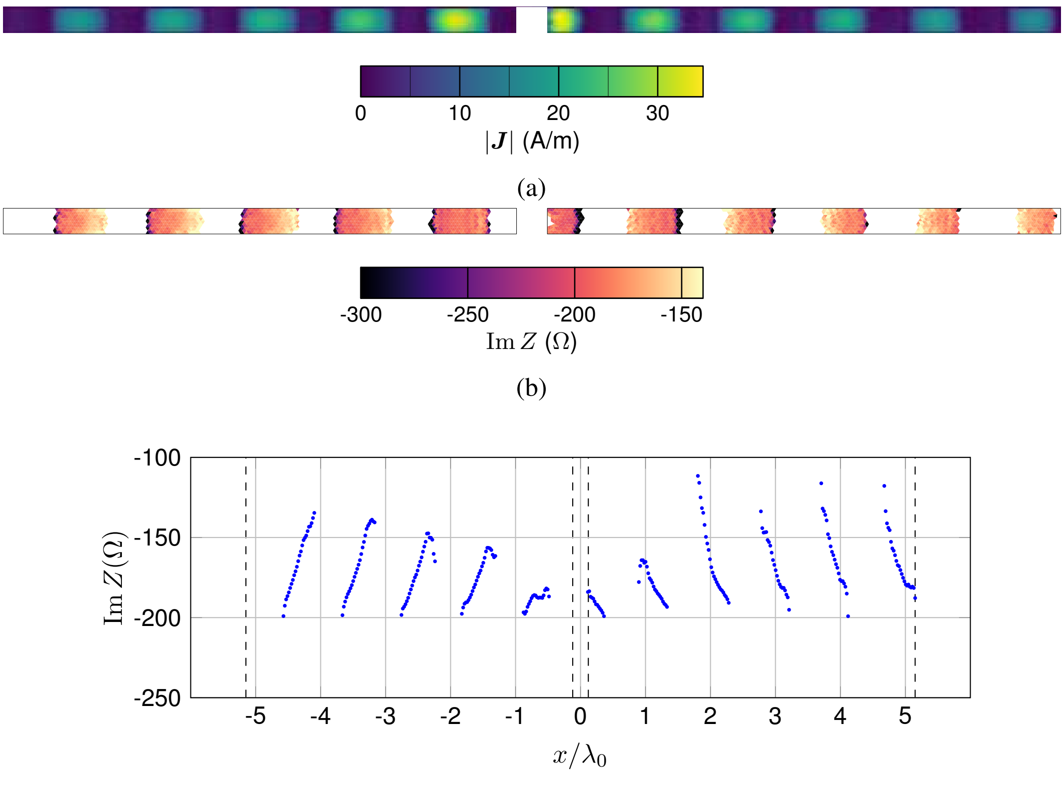

(a)

(b)

(c)

Fig. 4.20 Symmetric strip antenna: (a) optimized surface current, (b) resulting surface reactance, (c) cut view of the impedance profile along the x axis (vertical lines represent the surface bounds).

The relevant plane cut pattern is shown in Fig. 4.21a, along with the mask requirements; as can be seen from Fig. 4.21b, the top view of the pattern in the u-v space confirms the behaviour of the radiation in the transverse plane. The achieved realized gain is equal to $13.1\,\mathrm{dB}$, with a directivity of $15.8\,\mathrm{dB}$. It must be observed that the power of the incident field refers to an unrestricted cylindrical source, with only a portion thereof intercepted by the thin strip metasurface; hence, the realized gain may be significantly lower than the one actually observed in the case of a finite-size dieletric substrate. Furthermore, the obtained total efficiency indicates that the optimization has avoided bandstop effects, possibly present in leaky-wave-based designs, that are associated with higher reflection coefficients.

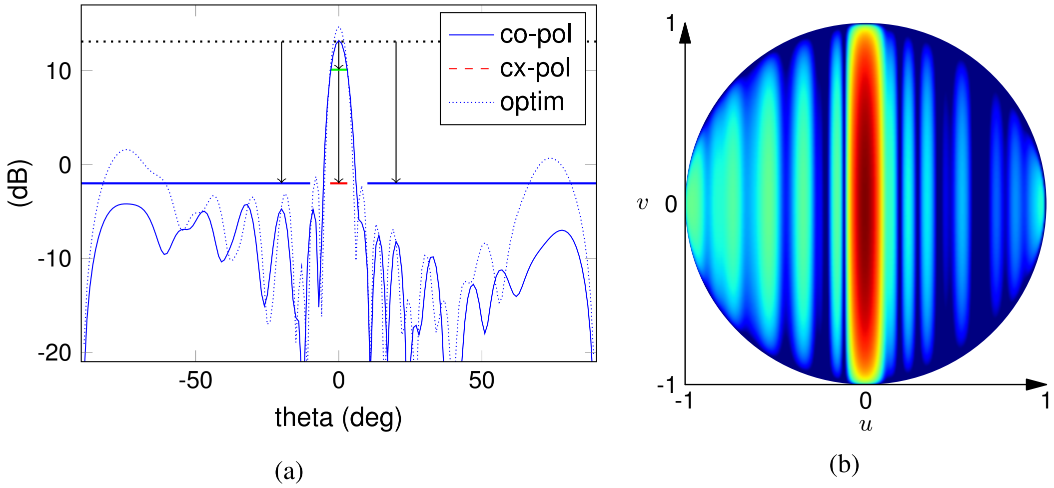

(a)

(b)

Fig. 4.21 Symmetric strip antenna: (a) mask requirements and realized gain in the plane cut $\varphi = 0°$, (b) top view of the pattern in the u-v plane.

4.5 Analysis

In all cases, the presented method resulted in satisfactory designs, yielding realizable impedance distributions and radiation patterns compliant with the mask-type specifications. Rather different field specifications were considered, and no symmetries have been enforced (which can still be easily done, reducing the computational cost), showing a substantial symmetry preservation with respect to the incident field.

Of particular relevance is the fact that all results have been obtained without any a-priori information, and *all* designs for the circular metasurface have been obtained from the *same starting current*, regardless of desired polarization and beam direction. Although a proof of optimimality could not be provided, the presented results appear as a practical confirmation of stability and flexibility. The discrepancies observed between the optimized and the final radiation fields can be mostly attributed to the algorithm employed for the impedance computation. This means that the results can be improved, without modifying the current optimization step, by considering more sophisticated approaches to obtain the impedance.

From the computational and memory point of view, the design instances ran on a Desktop PC with Intel Core i7 processor and $16\,\mathrm{GB}$ RAM; memory occupation at all times was within $4\,\mathrm{GB}$ for the largest case of circular antenna with $D = 10\lambda_0$. The total time required for each design varied as a consequence of the different number of iterations needed to reach convergence; as a reference measure, the time that each iteration of the non-linear conjugate gradient took ranges from $3\,\mathrm{s}$ for the strip antenna, up to $10\,\mathrm{s}$ for the design of the large circular antenna. Considering an average of 500 iterations, this results in a total optimization time of less than $1.5\,\mathrm{h}$ in the worst case. Of course, this does not take into account the time spent on finding the right balance of the weighting coefficients which, nevertheless, is moderate compared to the total one.

Chapter 5

Conclusions

In this dissertation, a novel approach for the design of 3D metasurface antennas has been presented, which is fully automated and computationally efficient. The metasurface is modelled as a layer of equivalent impedance boundary condition (IBC), which defines its macroscopic behaviour, allowing to effectively handle the desing of electrically large metasurface antennas.

The proposed method aims at the macroscopic design of the equivalent surface impedance distribution, by requiring it to be physically realizable (i.e., passive and lossless, with reactance within practical limits), and that the resulting radiated field obeys the specifications, when excited by a given incident field. The implementation of the individual unit cells can be carried out, once the impedance distribution is known, by means of tested methods available in the literature.

The metasurface design is formulated as an electromagnetic scattering problem based on an Electric Field Integral Equation, where the only unknown is the (equivalent) electric current flowing on the metasurface. The numerical discretization is based on a triangular mesh of the surface and the expansion of the current in RWG basis functions. The optimization process employs only this equivalent current, and avoids the solution of the forward problem at each iteration, greatly reducing the computational load per iteration. A non-linear conjugate gradient algorithm is employed for the minimization task. The objective function has a polynomial formulation that incorporates inequality constraints through the use of squared ramp functions, and it has been demonstrated that it can be cast in a form that allows the use of fast matrix-vector product routines for the relevant electromagnetic operators, i.e., the scattering and radiation ones. Moreover, the line search procedure is carried out in an iterative way trough the closed form minimization of fourth-order polynomials, without requiring a priori assumptions on the search interval. The impedance distribution is obtained only at the end of the current synthesis, and independently from it, through the numerical solution of the IBC equation, computed by expanding the impedance with arbitrary basis functions.

The presented application examples concentrated on low-profile metasurface antennas with on-surface feed: the considered shapes were circular and elliptical surfaces, and a symmetric strip structure. Field specifications included pencil and shaped beam patterns, both broadside and squinted, and for both circular and linear polarizations. Owing to the satisfactory results, the flexibility of the approach has been verified, together with its stability and independence of the solution from the choice of the initial current.

Several improvements and extensions are foreseen based upon the work presented in this thesis. First of all, the full design cycle includes the unit cell design. Therefore, the obtained impedance profiles will be implemented by an appropriate layout of unit cells, allowing full-wave simulations to be carried out in order to verify the robustness of the modelling. After that, prototyping and testing will be the last step toward the practical use of the proposed method. From the algorithmic point of view, a generalization to tensor impedances is of relevance for the design of anisotropic metasurface antennas, allowing a finer control of polarization. This extension represents a necessary step toward the design of multi-beam antennas, where the same metasurface radiates different prescribed fields, when illuminated by different incident fields. Finally, current and impedance postprocessing, including smoothing and filtering, will be investigated in future developments.

Appendix A

Power balance for metasurface antennas

A.1 Power density absorbed by a surface

In order to define the energetic properties of a metasurface, the expression of the absorbed power density for a general surface $\mathcal{S}$ is needed. To this aim, Poynting's theorem is applied to an arbitrary volume $\mathcal{V}$ that crosses this surface, giving

$$\begin{aligned}\tilde{P} &= P_{\mathrm{diss}} + \mathrm{j}2\omega(W_{\mathrm{m}} - W_{\mathrm{e}}) \\ &= \iiint\limits_{\mathcal{V}} \tilde{p}\ \mathrm{d}V = \oiint\limits_{\partial\mathcal{V}} \boldsymbol{S}\cdot\hat{\boldsymbol{n}}\,\mathrm{d}S,\end{aligned} \tag{A.1}$$

where P_{diss} is the total dissipated power, W_{e} and W_{m} are the electric and magnetic stored energies, respectively, and $\tilde{p}$ is the absorbed (volume) power density. The surface integral involves the Poynting vector $\boldsymbol{S} = \boldsymbol{E}\times\boldsymbol{H}^*$ and the normal unit vector $\hat{\boldsymbol{n}}$ is directed inside the volume, as dictated by the "load" convention. The boundary $\partial\mathcal{V}$ is given by the union of three disjoint surfaces: $\mathcal{S}_+$ and $\mathcal{S}_-$ are on the opposite sides of $\mathcal{S}$, while $\mathcal{S}_{\mathrm{side}}$ is the surface that joins the two sides across $\mathcal{S}$. With this partition of the bounding surface, the surface integral can be written as

$$\tilde{P} = \iint\limits_{\mathcal{S}_+} \boldsymbol{S}\cdot\hat{\boldsymbol{n}}\,\mathrm{d}S + \iint\limits_{\mathcal{S}_-} \boldsymbol{S}\cdot\hat{\boldsymbol{n}}\,\mathrm{d}S + \iint\limits_{\mathcal{S}_{\mathrm{side}}} \boldsymbol{S}\cdot\hat{\boldsymbol{n}}\,\mathrm{d}S. \tag{A.2}$$

In the limit where $\mathcal{S}_+$ and $\mathcal{S}_-$ tend to $\mathcal{S}$ from the two sides, the volume integral collapses into a surface integral over $\mathcal{S}$ and the contribution of the integral over $\mathcal{S}_{\text{side}}$ vanishes. The normal unit vectors on both sides have opposite directions, i.e., $\hat{\boldsymbol{n}}|_{\mathcal{S}_-} = -\hat{\boldsymbol{n}}|_{\mathcal{S}_+} \equiv \hat{\boldsymbol{n}}$, and the expression for the total surface power (A.1) reduces to

$$\lim_{\substack{\mathcal{S}_+\to\mathcal{S}\\ \mathcal{S}_-\to\mathcal{S}}} \tilde{P} = \iint\limits_{\mathcal{S}} \tilde{p}\,\mathrm{d}S = -\iint\limits_{\mathcal{S}} (\boldsymbol{S}_+ - \boldsymbol{S}_-)\cdot\hat{\boldsymbol{n}}\,\mathrm{d}S. \tag{A.3}$$

By restricting the analysis to the case where the surface introduces discontinuities in the magnetic field only (as is the case for a metasurface that imposes an Impedance Boundary Condition of the type (2.1)), it follows that $\boldsymbol{E}_+ = \boldsymbol{E}_- = \boldsymbol{E}$ and the final expression reads

$$\begin{aligned}\tilde{P} &= \iint_{\mathcal{S}} \tilde{p}\,\mathrm{d}S = -\iint_{\mathcal{S}} \boldsymbol{E}\times(\boldsymbol{H}_+ - \boldsymbol{H}_-)^*\cdot\hat{\boldsymbol{n}}\,\mathrm{d}S\\ &= \iint_{\mathcal{S}} \boldsymbol{E}\cdot[\hat{\boldsymbol{n}}\times(\boldsymbol{H}_+ - \boldsymbol{H}_-)^*]\,\mathrm{d}S\\ &= \iint_{\mathcal{S}} \boldsymbol{E}\cdot\boldsymbol{J}^*\,\mathrm{d}S,\end{aligned} \tag{A.4}$$

where the definition (2.15) for the equivalent surface current has been used. Since the surface $\mathcal{S}$ is arbitrary, the equality of the integrands in (A.4) must hold point-wise. The definition of the surface absorbed power density is therefore given by

$$\tilde{p} = \boldsymbol{E}\cdot[\hat{\boldsymbol{n}}\times(\boldsymbol{H}_+ - \boldsymbol{H}_-)^*] = \boldsymbol{E}\cdot\boldsymbol{J}^*. \tag{A.5}$$

A.2 Power balance for radiation scattered by a surface

In the following, the aim is to investigate the power balance in the case of scattering of an incident field by a generic surface. Consider a volume $\mathcal{V}$, which contains source currents $\boldsymbol{J}_{\text{src}}$ and $\boldsymbol{M}_{\text{src}}$, and a passive scatterer (Fig. A.1). Consistent with the integral equation approach, the scatterer, enclosed by volume $\mathcal{V}_{\text{sc}}$, is replaced with equivalent currents $\boldsymbol{J}_{\text{eq}}$ and $\boldsymbol{M}_{\text{eq}}$ on the boundary surface $\partial\mathcal{V}_{\text{sc}}$. Applying Poynting's theorem to the volume $\mathcal{V}$ results in

$$\tilde{P}_{\text{src}} = \tilde{P}_{\text{sc}} + \tilde{P}_{\text{out}} + \mathrm{j}2\omega\,(W_{\text{m}} - W_{\text{e}}), \tag{A.6}$$

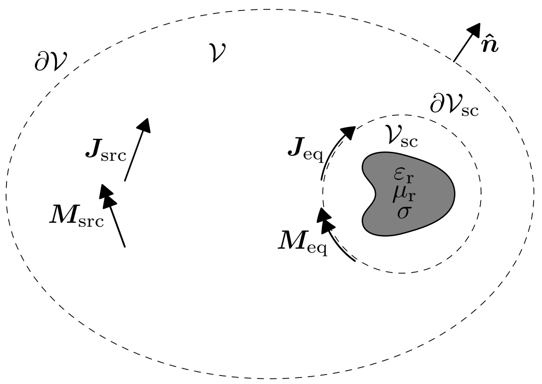

Fig. A.1 Depiction of the scattering problem for the computation of the power balance.

where

$$\tilde{P}_{\mathrm{src}} = -\iiint\limits_{\mathcal{V}} (\boldsymbol{E}\cdot\boldsymbol{J}_{\mathrm{src}}^{*} + \boldsymbol{H}^{*}\cdot\boldsymbol{M}_{\mathrm{src}})\,\mathrm{d}V, \tag{A.7}$$

$$\tilde{P}_{\mathrm{sc}} = \oiint\limits_{\partial\mathcal{V}_{\mathrm{sc}}} (\boldsymbol{E}_{\mathrm{avg}}\cdot\boldsymbol{J}_{\mathrm{eq}}^{*} + \boldsymbol{H}_{\mathrm{avg}}^{*}\cdot\boldsymbol{M}_{\mathrm{eq}})\,\mathrm{d}S, \tag{A.8}$$

$$\tilde{P}_{\mathrm{out}} = \oiint\limits_{\partial\mathcal{V}} (\boldsymbol{E}\times\boldsymbol{H}^{*})\cdot\hat{\boldsymbol{n}}\,\mathrm{d}S, \tag{A.9}$$

$$W_{\mathrm{e}} = \frac{1}{2}\iiint\limits_{\mathcal{V}} \varepsilon\,|\boldsymbol{E}|^{2}\,\mathrm{d}V, \tag{A.10}$$

$$W_{\mathrm{m}} = \frac{1}{2}\iiint\limits_{\mathcal{V}} \mu\,|\boldsymbol{H}|^{2}\,\mathrm{d}V. \tag{A.11}$$

Here, P_{src} is the power supplied by source currents, P_{sc} is the power absorbed (the real part corresponds to dissipated power) by the scatterer, P_{out} is the power radiated outside volume $\mathcal{V}$ ($\hat{\boldsymbol{n}}$ is the outward unit normal vector), and W_{e} and W_{m} are the electric and magnetic stored energies. The average fields in (A.8) are defined as

$$\boldsymbol{E}_{\mathrm{avg}} = \frac{1}{2}\big(\boldsymbol{E}_{+} + \boldsymbol{E}_{-}\big), \tag{A.12}$$

$$\boldsymbol{H}_{\mathrm{avg}} = \frac{1}{2}\big(\boldsymbol{H}_{+} + \boldsymbol{H}_{-}\big), \tag{A.13}$$

where subscripts $+$ and $-$ refer to the field on each side of the surface. They are needed as the equivalent currents on $\partial\mathcal{V}_{\mathrm{sc}}$ create a discontinuity in the electric and magnetic fields.

In the analysis of the field scattered by an object, the total field outside the scatterer can be obtained as the superposition of the incident and scattered fields,

$$\begin{aligned}\boldsymbol{E} &= \boldsymbol{E}_{\text{inc}} + \boldsymbol{E}_{\text{sc}},\\ \boldsymbol{H} &= \boldsymbol{H}_{\text{inc}} + \boldsymbol{H}_{\text{sc}},\end{aligned}$$

where the incident field is the one radiated by source currents $\boldsymbol{J}_{\text{src}}$ and $\boldsymbol{M}_{\text{src}}$ in absence of the scatterer, while the scattered field is due to equivalent currents $\boldsymbol{J}_{\text{eq}}$ and $\boldsymbol{M}_{\text{eq}}$ which represent the effect of the scatterer. The latter are obtained as the solution of an integral equation.

Therefore, two source-field couples can be identified, which are both individual solutions to Maxwell's equations in the background medium (in absence of the scatterer):

$$(\boldsymbol{J}_{\text{src}}\,, \boldsymbol{M}_{\text{src}}) \longrightarrow (\boldsymbol{E}_{\text{inc}}\,, \boldsymbol{H}_{\text{inc}}), \tag{A.14}$$

$$(\boldsymbol{J}_{\text{eq}}\,, \boldsymbol{M}_{\text{eq}}) \longrightarrow (\boldsymbol{E}_{\text{sc}}\,, \boldsymbol{H}_{\text{sc}}). \tag{A.15}$$

The sum of the two is the solution of the scattering problem,

$$(\boldsymbol{J}_{\text{src}} + \boldsymbol{J}_{\text{eq}}\,, \boldsymbol{M}_{\text{src}} + \boldsymbol{M}_{\text{eq}}) \longrightarrow (\boldsymbol{E}\,, \boldsymbol{H}). \tag{A.16}$$

With this decomposition, Poynting's theorem can be formulated for each set of sources independently, then for the sum of the two. In what follows, the analysis is restricted to the active power, i.e., the real part of the complex power, as it is the most relevant one for the evaluation of efficiency. The imaginary part, related to the storage of energy, is linked to the resonant behaviour of the scatterer and will not be discussed further.

Sources $(\boldsymbol{J}_{\text{src}}\,, \boldsymbol{M}_{\text{src}})$ For the source currents alone, the real part of Poynting's theorem reads

$$\begin{aligned}P_{\text{inc}} &= -\operatorname{Re}\iiint_{\mathcal{V}} (\boldsymbol{E}_{\text{inc}} \cdot \boldsymbol{J}^{*}_{\text{src}} + \boldsymbol{H}^{*}_{\text{inc}} \cdot \boldsymbol{M}_{\text{src}})\,\mathrm{d}V\\ &= \operatorname{Re}\oint\!\!\!\oint_{\partial\mathcal{V}} (\boldsymbol{E}_{\text{inc}} \times \boldsymbol{H}^{*}_{\text{inc}}) \cdot \hat{\boldsymbol{n}}\,\mathrm{d}S \geq 0.\end{aligned} \tag{A.17}$$

Sources $(\boldsymbol{J}_{\mathrm{eq}}\,,\boldsymbol{M}_{\mathrm{eq}})$ The equivalent currents radiate a field equal to $\boldsymbol{E}_{\mathrm{sc}}$ outside volume $\mathcal{V}_{\mathrm{sc}}$, and a field that cancels the incident field inside, i.e., $-\boldsymbol{E}_{\mathrm{inc}}$, inside. The fields are discontinuous at the boundary $\partial\mathcal{V}_{\mathrm{sc}}$, and their averages are equal to

$$\boldsymbol{E}_{\mathrm{avg}} = \frac{1}{2}\big(\boldsymbol{E}_{\mathrm{sc}} - \boldsymbol{E}_{\mathrm{inc}}\big), \tag{A.18}$$

$$\boldsymbol{H}_{\mathrm{avg}} = \frac{1}{2}\big(\boldsymbol{H}_{\mathrm{sc}} - \boldsymbol{H}_{\mathrm{inc}}\big). \tag{A.19}$$

Therefore, the real part of Poynting's theorem is formulated as

$$\begin{aligned} P_{\mathrm{eq}} &= \mathrm{Re} \iint_{\partial\mathcal{V}_{\mathrm{sc}}} \frac{1}{2}\big((\boldsymbol{E}_{\mathrm{sc}} - \boldsymbol{E}_{\mathrm{inc}}) \cdot \boldsymbol{J}^*_{\mathrm{eq}} + (\boldsymbol{H}_{\mathrm{sc}} - \boldsymbol{H}_{\mathrm{inc}})^* \cdot \boldsymbol{M}_{\mathrm{eq}}\big)\,\mathrm{d}V \\ &= \frac{1}{2}\,\mathrm{Re} \iint_{\partial\mathcal{V}_{\mathrm{sc}}} \big(\boldsymbol{E}_{\mathrm{sc}} \cdot \boldsymbol{J}^*_{\mathrm{eq}} - \boldsymbol{E}_{\mathrm{inc}} \cdot \boldsymbol{J}^*_{\mathrm{eq}} + \boldsymbol{H}^*_{\mathrm{sc}} \cdot \boldsymbol{M}_{\mathrm{eq}} - \boldsymbol{H}^*_{\mathrm{inc}} \cdot \boldsymbol{M}_{\mathrm{eq}}\big)\,\mathrm{d}V \\ &= -\,\mathrm{Re} \oiint_{\partial\mathcal{V}} (\boldsymbol{E}_{\mathrm{sc}} \times \boldsymbol{H}^*_{\mathrm{sc}}) \cdot \hat{\boldsymbol{n}}\,\mathrm{d}S \;\leq 0. \end{aligned} \tag{A.20}$$

In this case, the absorbed power is negative, as suggested by the fact that, in this case, the source currents are equivalent ones and do not correspond to a physical setting.

Sources $(\boldsymbol{J}_{\mathrm{src}} + \boldsymbol{J}_{\mathrm{eq}}\,,\boldsymbol{M}_{\mathrm{src}} + \boldsymbol{M}_{\mathrm{eq}})$ In this case, the left hand side of Poynting's theorem P_{src} can be written as the sum of two terms,

$$P_{\mathrm{src}} = P_{\mathrm{inc}} - P_{\mathrm{refl}}, \tag{A.21}$$

where P_{inc} has been defined in (A.17), and

$$P_{\mathrm{refl}} = -\,\mathrm{Re} \iiint_{\mathcal{V}} (\boldsymbol{E}_{\mathrm{sc}} \cdot \boldsymbol{J}^*_{\mathrm{src}} + \boldsymbol{H}^*_{\mathrm{sc}} \cdot \boldsymbol{M}_{\mathrm{src}})\,\mathrm{d}V. \tag{A.22}$$

The term P_{inc}, being the physical power delivered by source currents in absence of scattering, must be non-negative. The reflected power P_{refl}, instead, is given by the product of a current with the field radiated by another set of sources, and as such it does not represent a physical power. Therefore, it can be positive or negative. However, for the currents $\boldsymbol{J}_{\mathrm{eq}}$, $\boldsymbol{M}_{\mathrm{eq}}$ to represent physical scattering by a passive object, they must obey

$$0 \leq P_{\mathrm{src}} \leq P_{\mathrm{inc}} \quad \longrightarrow \quad 0 \leq P_{\mathrm{refl}} \leq P_{\mathrm{inc}}. \tag{A.23}$$

In this case, the average fields on the equivalent source layer are

$$\boldsymbol{E}_{\mathrm{avg}} = \frac{1}{2}\big(\boldsymbol{E} + \boldsymbol{0}\big) = \frac{1}{2}\big(\boldsymbol{E}_{\mathrm{inc}} + \boldsymbol{E}_{\mathrm{sc}}\big), \tag{A.24}$$

$$\boldsymbol{H}_{\mathrm{avg}} = \frac{1}{2}\big(\boldsymbol{H} + \boldsymbol{0}\big) = \frac{1}{2}\big(\boldsymbol{H}_{\mathrm{inc}} + \boldsymbol{H}_{\mathrm{sc}}\big). \tag{A.25}$$

The right hand side of Poynting's theorem can then be written as $P_{\mathrm{sc}} + P_{\mathrm{out}}$, where

$$\begin{aligned} P_{\mathrm{sc}} &= \mathrm{Re} \oiint_{\partial\mathcal{V}_{\mathrm{sc}}} \frac{1}{2}\big((\boldsymbol{E}_{\mathrm{sc}} + \boldsymbol{E}_{\mathrm{inc}}) \cdot \boldsymbol{J}_{\mathrm{eq}}^{*} + (\boldsymbol{H}_{\mathrm{sc}} + \boldsymbol{H}_{\mathrm{inc}})^{*} \cdot \boldsymbol{M}_{\mathrm{eq}}\big)\,\mathrm{d}V \\ &= \mathrm{Re}\,\frac{1}{2} \oiint_{\partial\mathcal{V}_{\mathrm{sc}}} \big(\boldsymbol{E}_{\mathrm{sc}} \cdot \boldsymbol{J}_{\mathrm{eq}}^{*} + \boldsymbol{E}_{\mathrm{inc}} \cdot \boldsymbol{J}_{\mathrm{eq}}^{*} + \boldsymbol{H}_{\mathrm{sc}}^{*} \cdot \boldsymbol{M}_{\mathrm{eq}} + \boldsymbol{H}_{\mathrm{inc}}^{*} \cdot \boldsymbol{M}_{\mathrm{eq}}\big)\,\mathrm{d}V \\ &= P_{\mathrm{eq}} + \mathrm{Re} \oiint_{\partial\mathcal{V}_{\mathrm{sc}}} \big(\boldsymbol{E}_{\mathrm{inc}} \cdot \boldsymbol{J}_{\mathrm{eq}}^{*} + \boldsymbol{H}_{\mathrm{inc}}^{*} \cdot \boldsymbol{M}_{\mathrm{eq}}\big)\,\mathrm{d}V, \end{aligned} \tag{A.26}$$

$$\begin{aligned} P_{\mathrm{out}} &= \mathrm{Re} \iint_{\partial\mathcal{V}} \big((\boldsymbol{E}_{\mathrm{sc}} + \boldsymbol{E}_{\mathrm{inc}}) \times (\boldsymbol{H}_{\mathrm{sc}} + \boldsymbol{H}_{\mathrm{inc}})^{*}\big) \cdot \hat{\boldsymbol{n}}\,\mathrm{d}S \\ &= \mathrm{Re} \iint_{\partial\mathcal{V}} \big(\boldsymbol{E}_{\mathrm{sc}} \times \boldsymbol{H}_{\mathrm{sc}}^{*} + \boldsymbol{E}_{\mathrm{sc}} \times \boldsymbol{H}_{\mathrm{inc}}^{*} + \boldsymbol{E}_{\mathrm{inc}} \times \boldsymbol{H}_{\mathrm{sc}}^{*} + \boldsymbol{E}_{\mathrm{inc}} \times \boldsymbol{H}_{\mathrm{inc}}^{*}\big) \cdot \hat{\boldsymbol{n}}\,\mathrm{d}S \\ &= P_{\mathrm{inc}} - P_{\mathrm{eq}} + \mathrm{Re} \iint_{\partial\mathcal{V}} \big(\boldsymbol{E}_{\mathrm{sc}} \times \boldsymbol{H}_{\mathrm{inc}}^{*} + \boldsymbol{E}_{\mathrm{inc}} \times \boldsymbol{H}_{\mathrm{sc}}^{*}\big) \cdot \hat{\boldsymbol{n}}\,\mathrm{d}S. \end{aligned} \tag{A.27}$$

In conclusion, Poynting's theorem can be expressed using the newly defined quantities:

$$\begin{aligned} P_{\mathrm{inc}} - P_{\mathrm{refl}} = P_{\mathrm{eq}} &+ \mathrm{Re} \oiint_{\partial\mathcal{V}_{\mathrm{sc}}} \big(\boldsymbol{E}_{\mathrm{inc}} \cdot \boldsymbol{J}_{\mathrm{eq}}^{*} + \boldsymbol{H}_{\mathrm{inc}}^{*} \cdot \boldsymbol{M}_{\mathrm{eq}}\big)\,\mathrm{d}V \\ &+ P_{\mathrm{inc}} - P_{\mathrm{eq}} + \mathrm{Re} \oiint_{\partial\mathcal{V}} \big(\boldsymbol{E}_{\mathrm{sc}} \times \boldsymbol{H}_{\mathrm{inc}}^{*} + \boldsymbol{E}_{\mathrm{inc}} \times \boldsymbol{H}_{\mathrm{sc}}^{*}\big) \cdot \hat{\boldsymbol{n}}\,\mathrm{d}S. \end{aligned} \tag{A.28}$$

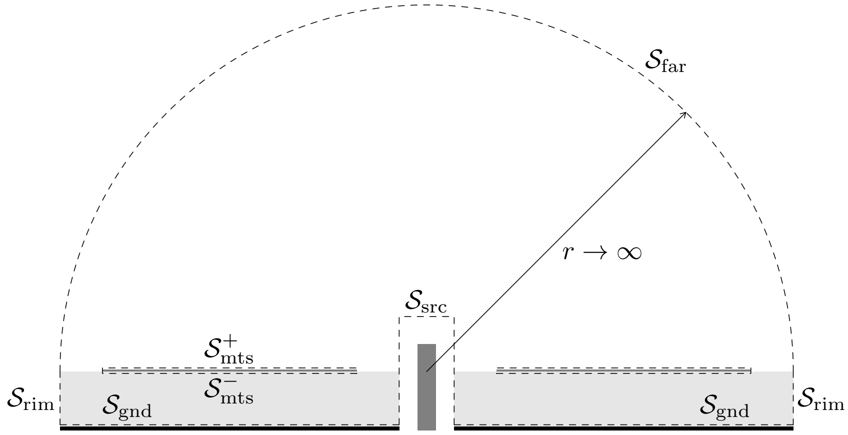

Fig. A.2 Illustration of the surfaces involved in the formulation of Poynting's theorem for a single-layer metasurface.

In this way, the reflected power can be alternatively written as

$$\begin{aligned} P_{\mathrm{refl}} = &-\mathrm{Re} \oint\!\!\oint_{\partial\mathcal{V}_{\mathrm{sc}}} \left(\boldsymbol{E}_{\mathrm{inc}} \cdot \boldsymbol{J}^{*}_{\mathrm{eq}} + \boldsymbol{H}^{*}_{\mathrm{inc}} \cdot \boldsymbol{M}_{\mathrm{eq}}\right) \mathrm{d}V \\ &-\mathrm{Re} \oint\!\!\oint_{\partial\mathcal{V}} \left(\boldsymbol{E}_{\mathrm{sc}} \times \boldsymbol{H}^{*}_{\mathrm{inc}} + \boldsymbol{E}_{\mathrm{inc}} \times \boldsymbol{H}^{*}_{\mathrm{sc}}\right) \cdot \hat{\boldsymbol{n}}\, \mathrm{d}S. \end{aligned} \tag{A.29}$$

A.3 Single-layer Metasurface

The derivation of the previous section will now be specialized to the case of a single-layer metasurface. Poynting's theorem is applied to the volume in Fig. A.2, bounded by the closed surface $\partial\mathcal{V} = \mathcal{S}_{\mathrm{far}} \cup \mathcal{S}_{\mathrm{rim}} \cup \mathcal{S}_{\mathrm{gnd}}$, where: $\mathcal{S}_{\mathrm{far}}$ encloses the upper half sphere, with a radius that tends to $+\infty$, $\mathcal{S}_{\mathrm{rim}}$ encircles the outer border of the dielectric substrate, and $\mathcal{S}_{\mathrm{gnd}}$ covers the lower ground plane. Sources $\boldsymbol{J}_{\mathrm{src}}$ and $\boldsymbol{M}_{\mathrm{src}}$ are enclosed by the surface $\mathcal{S}_{\mathrm{src}}$. The scattering element, i.e., the metasurface layer where equivalent electric currents $\boldsymbol{J}$ flow, is surrounded by $\partial\mathcal{V}_{\mathrm{sc}} = \mathcal{S}_{\mathrm{mts}}$, that can be further subdivided into an upper surface $\mathcal{S}^{+}_{\mathrm{mts}}$ and lower one $\mathcal{S}^{-}_{\mathrm{mts}}$.

Specializing the general formula (A.6) to this case, the different power contributions can be written as

$$P_{\mathrm{out}} = P_{\mathrm{far}} + P_{\mathrm{rim}} + P_{\mathrm{gnd}}, \tag{A.30}$$

$$P_{\mathrm{sc}} = P_{\mathrm{mts}}. \tag{A.31}$$

With this, Poynting's theorem is written as

$$P_{\mathrm{src}} = P_{\mathrm{far}} + P_{\mathrm{rim}} + P_{\mathrm{gnd}} + P_{\mathrm{mts}}. \tag{A.32}$$

Each term is given by an integral over the respective part of the surface,

$$P_{\mathrm{src}} = \mathrm{Re} \iint\limits_{S_{\mathrm{src}}} \left(\boldsymbol{E}_{\mathrm{avg}} \cdot \boldsymbol{J}^*_{\mathrm{src}} + \boldsymbol{H}^*_{\mathrm{avg}} \cdot \boldsymbol{M}_{\mathrm{src}} \right) \mathrm{d}S, \tag{A.33}$$

$$P_{\mathrm{far}} = \mathrm{Re} \iint\limits_{S_{\mathrm{far}}} \left(\boldsymbol{E} \times \boldsymbol{H}^* \right) \cdot \hat{\boldsymbol{r}} \, \mathrm{d}S = \iint\limits_{S_{\mathrm{far}}} \frac{|\boldsymbol{E}|^2}{\eta} \, \mathrm{d}S, \tag{A.34}$$

$$P_{\mathrm{rim}} = \mathrm{Re} \iint\limits_{S_{\mathrm{rim}}} \left(\boldsymbol{E} \times \boldsymbol{H}^* \right) \cdot \hat{\boldsymbol{\rho}} \, \mathrm{d}S, \tag{A.35}$$

$$P_{\mathrm{gnd}} = \mathrm{Re} \iint\limits_{S_{\mathrm{gnd}}} \left(\boldsymbol{E} \times \boldsymbol{H}^* \right) \cdot (-\hat{\boldsymbol{z}}) \, \mathrm{d}S = \mathrm{Re} \iint\limits_{S_{\mathrm{gnd}}} \left(\hat{\boldsymbol{z}} \times \boldsymbol{E} \right) \cdot \boldsymbol{H}^* \, \mathrm{d}S = 0, \tag{A.36}$$

$$\begin{aligned} P_{\mathrm{mts}} &= \mathrm{Re} \left[\iint\limits_{S^+_{\mathrm{mts}}} \left(\boldsymbol{E} \times \boldsymbol{H}^* \right) \cdot (-\hat{\boldsymbol{z}}) \, \mathrm{d}S + \iint\limits_{S^-_{\mathrm{mts}}} \left(\boldsymbol{E} \times \boldsymbol{H}^* \right) \cdot \hat{\boldsymbol{z}} \, \mathrm{d}S \right] \\ &= \mathrm{Re} \iint\limits_{S_{\mathrm{mts}}} \boldsymbol{E} \cdot \left(\hat{\boldsymbol{z}} \times \left(\boldsymbol{H}_+ - \boldsymbol{H}_- \right)^* \right) \mathrm{d}S = \mathrm{Re} \iint\limits_{S_{\mathrm{mts}}} \boldsymbol{E} \cdot \boldsymbol{J}^* \, \mathrm{d}S. \end{aligned} \tag{A.37}$$

It is useful to derive additional quantities for analyzing the power balance. The *incident power* is given by

$$P_{\mathrm{inc}} = \mathrm{Re} \iint\limits_{S_{\mathrm{src}}} \left(\boldsymbol{E}_{\mathrm{inc}} \times \boldsymbol{H}^*_{\mathrm{inc}} \right) \cdot \hat{\boldsymbol{\rho}} \, \mathrm{d}S, \tag{A.38}$$

and the *radiated power* is

$$P_{\mathrm{rad}} = P_{\mathrm{far}} = \iint\limits_{S_{\mathrm{far}}} \frac{|\boldsymbol{E}|^2}{\eta} \, \mathrm{d}S. \tag{A.39}$$

Lastly, the *reflected power* can be written as

$$
\begin{aligned}
P_{\mathrm{refl}} = &- \mathrm{Re} \iint_{\mathcal{S}_{\mathrm{mts}}} \boldsymbol{E}_{\mathrm{inc}} \cdot \boldsymbol{J}^{*} \, \mathrm{d}V \\
&- \mathrm{Re} \iint_{\mathcal{S}_{\mathrm{far}}} \left(\boldsymbol{E}_{\mathrm{sc}} \times \boldsymbol{H}^{*}_{\mathrm{inc}} + \boldsymbol{E}_{\mathrm{inc}} \times \boldsymbol{H}^{*}_{\mathrm{sc}} \right) \cdot \hat{\boldsymbol{r}} \, \mathrm{d}S \\
&- \mathrm{Re} \iint_{\mathcal{S}_{\mathrm{rim}}} \left(\boldsymbol{E}_{\mathrm{sc}} \times \boldsymbol{H}^{*}_{\mathrm{inc}} + \boldsymbol{E}_{\mathrm{inc}} \times \boldsymbol{H}^{*}_{\mathrm{sc}} \right) \cdot \hat{\boldsymbol{\rho}} \, \mathrm{d}S.
\end{aligned}
\tag{A.40}
$$

These quantities are functions of the incident field and of the equivalent current, without the need for an explicit expression of the source currents. This is useful whenever the incident field is known, but the related sources are difficult to find (e.g., for an incident plane wave). The *radiation efficiency* is defined as

$$
e_{\mathrm{rad}} = \frac{P_{\mathrm{rad}}}{P_{\mathrm{src}}} = \frac{P_{\mathrm{rad}}}{P_{\mathrm{inc}} - P_{\mathrm{refl}}}, \tag{A.41}
$$

while the *total efficiency* is given by

$$
e_0 = \frac{P_{\mathrm{rad}}}{P_{\mathrm{inc}}}. \tag{A.42}
$$

A.4 Surface wave incident power

Being able to find the power delivered by the source (incident) field is key in the evaluation of efficiency. The most practical case of on-surface feed is constituted by a vertical pin at the center of the metasurface, connected through a coaxial aperture in the ground plane. The radiated spectrum is composed of guided waves and free space radiating waves. The usual assumption is to neglect the radiating waves and assume a purely fundamental, TM_0 mode propagation. In most cases, this approximation is good enough for the design.

The TM_0 surface wave mode is a valid solution of Maxwell's equations on a dielectric slab, outside of a cylindrical region of radius R_{src} which encloses all sources. The incident power is given by the integral of the Poynting's vector on this cylindrical surface (A.38),

$$P_{\mathrm{inc}} = \mathrm{Re} \iint\limits_{\mathcal{S}_{\mathrm{src}}} \boldsymbol{E}_{\mathrm{inc}} \times \boldsymbol{H}^*_{\mathrm{inc}} \cdot \hat{\boldsymbol{\rho}}\, \mathrm{d}S = -\,\mathrm{Re} \int\limits_0^{2\pi} \int\limits_0^{+\infty} E_z H^*_\varphi\, R_{\mathrm{src}}\, \mathrm{d}\varphi\, \mathrm{d}z, \tag{A.43}$$

where the relevant components of the electric and magnetic fields are given by

$$E_z(\rho, z) = \begin{cases} E_0\, \dfrac{\beta_{\mathrm{sw}}}{\alpha_z}\, \mathrm{H}_0^{(2)}(\beta_{\mathrm{sw}}\rho)\, \mathrm{e}^{-\alpha_z z}, & z > 0 \\ E_0\, \dfrac{\beta_{\mathrm{sw}}}{\varepsilon_{\mathrm{r}}\alpha_z} \mathrm{H}_0^{(2)}(\beta_{\mathrm{sw}}\rho)\, \left[\cos(\beta_z z) - \gamma \sin(\beta_z z)\right], & -h < z < 0 \end{cases} \tag{A.44}$$

$$H_\varphi(\rho, z) = \begin{cases} E_0\, \dfrac{\mathrm{j}\omega\varepsilon_0}{\alpha_z}\, \mathrm{H}_1^{(2)}(\beta_{\mathrm{sw}}\rho)\, \mathrm{e}^{-\alpha_z z}, & z > 0 \\ E_0\, \dfrac{\mathrm{j}\omega\varepsilon_0}{\alpha_z}\, \mathrm{H}_1^{(2)}(\beta_{\mathrm{sw}}\rho)\, \left[\cos(\beta_z z) - \gamma \sin(\beta_z z)\right], & -h < z < 0 \end{cases} \tag{A.45}$$

with $\gamma = \tan(\beta_z h)$, and $\mathrm{H}_0^{(2)}$, $\mathrm{H}_1^{(2)}$ are Hankel functions of the second kind of order 0 and 1, respectively, and the propagation constants β_{sw}, β_z, and α_z are given by the solution of (4.2). Substituting (A.44), (A.45) into (A.43), after carrying out the integration one finds

$$P_{\mathrm{inc}} = |E_0|^2\, \omega\varepsilon_0\, \left[\frac{\varepsilon_{\mathrm{r}}}{(\beta_z)^2}\, \frac{1}{\sin^2(\beta_z h)}\, \left(h + \frac{\sin(2\beta_z h)}{2\beta_z}\right) + \frac{1}{(\alpha_z)^3}\right]. \tag{A.46}$$

This is also the maximum amount of active power that the source can supply.

Appendix B

Passivity and losslessness condition for tensor impedance

In this appendix, the requirement for a tensor impedance to be passive and lossless (PL) will be derived rigorously. In particular, it will be demonstrated that the most general form of a PL tensor impedance is the following:

$$\overline{\overline{\boldsymbol{Z}}} = \mathrm{j}X_I\overline{\overline{\boldsymbol{I}}} + R_N\overline{\overline{\boldsymbol{N}}} + \mathrm{j}X_K\overline{\overline{\boldsymbol{K}}} + \mathrm{j}X_L\overline{\overline{\boldsymbol{L}}}, \tag{B.1}$$

where X_I, R_N, X_K and X_L are real values. By substituting the expansion (2.7) in (2.8), and using definitions (2.3)–(2.6) for the basis dyadics, the complex power density can be written as

$$\begin{aligned} \tilde{p} =& \left(\overline{\overline{\boldsymbol{Z}}} \cdot \boldsymbol{J}\right) \cdot \boldsymbol{J}^* = \\ =& \left[\left(Z_I\overline{\overline{\boldsymbol{I}}} + Z_N\overline{\overline{\boldsymbol{N}}} + Z_K\overline{\overline{\boldsymbol{K}}} + Z_L\overline{\overline{\boldsymbol{L}}}\right) \cdot \boldsymbol{J}\right] \cdot \boldsymbol{J}^* = \\ =& Z_I\left(\overline{\overline{\boldsymbol{I}}} \cdot \boldsymbol{J}\right) \cdot \boldsymbol{J}^* + Z_N\left(\overline{\overline{\boldsymbol{N}}} \cdot \boldsymbol{J}\right) \cdot \boldsymbol{J}^* \\ &+ Z_K\left(\overline{\overline{\boldsymbol{K}}} \cdot \boldsymbol{J}\right) \cdot \boldsymbol{J}^* + Z_L\left(\overline{\overline{\boldsymbol{L}}} \cdot \boldsymbol{J}\right) \cdot \boldsymbol{J}^*, \end{aligned} \tag{B.2}$$

and the PL condition requires $\operatorname{Re}\tilde{p} = 0$.

First, it will be shown that (B.1) is necessary for the impedance to be passive and lossless. Considering that the PL condition must hold for *any* current $\boldsymbol{J}$, the demonstration starts by applying it to the particular case $\boldsymbol{J} = J_0\hat{\boldsymbol{u}}$, with J_0 an arbitrary complex constant, obtaining

$$\begin{aligned}0 =& \operatorname{Re}\big[Z_I\big(J_0\hat{\boldsymbol{u}}\big)\cdot J_0^*\hat{\boldsymbol{u}} + Z_N\big(J_0\hat{\boldsymbol{v}}\big)\cdot J_0^*\hat{\boldsymbol{u}}\\ &\quad + Z_K\big(J_0\hat{\boldsymbol{u}}\big)\cdot J_0^*\hat{\boldsymbol{u}} + Z_L\big(J_0\hat{\boldsymbol{v}}\big)\cdot J_0^*\hat{\boldsymbol{u}}\big]\\ =& \operatorname{Re}\big[Z_I\,|J_0|^2 + Z_K\,|J_0|^2\big]\\ =& (\operatorname{Re}Z_I + \operatorname{Re}Z_K)\,|J_0|^2\,,\end{aligned} \tag{B.3}$$

where the unit vectors $\hat{\boldsymbol{u}}$ and $\hat{\boldsymbol{v}}$ are orthogonal, therefore $\hat{\boldsymbol{u}}\cdot\hat{\boldsymbol{v}} = 0$. Taking into account the arbitrariness of J_0, (B.3) implies

$$\operatorname{Re}Z_I = -\operatorname{Re}Z_K. \tag{B.4}$$

At the same time, applying the PL condition to the case $\boldsymbol{J} = J_0\hat{\boldsymbol{v}}$ yields

$$\begin{aligned}0 =& \operatorname{Re}\big[Z_I\big(J_0\hat{\boldsymbol{v}}\big)\cdot J_0^*\hat{\boldsymbol{v}} + Z_N\big(-J_0\hat{\boldsymbol{u}}\big)\cdot J_0^*\hat{\boldsymbol{v}}\\ &\quad + Z_K\big(-J_0\hat{\boldsymbol{v}}\big)\cdot J_0^*\hat{\boldsymbol{v}} + Z_L\big(J_0\hat{\boldsymbol{u}}\big)\cdot J_0^*\hat{\boldsymbol{v}}\big]\\ =& \operatorname{Re}\big[Z_I\,|J_0|^2 - Z_K\,|J_0|^2\big]\\ =& (\operatorname{Re}Z_I - \operatorname{Re}Z_K)\,|J_0|^2\,,\end{aligned} \tag{B.5}$$

which is fulfilled only when

$$\operatorname{Re}Z_I = \operatorname{Re}Z_K. \tag{B.6}$$

Conditions (B.4) and (B.6) are both verified if and only if

$$\operatorname{Re}Z_I = \operatorname{Re}Z_K = 0. \tag{B.7}$$

Another relevant case is that for which $\boldsymbol{J} = J_0\hat{\boldsymbol{u}} + J_0\hat{\boldsymbol{v}}$, resulting in the following condition:

$$\begin{aligned}0 =& \operatorname{Re}\big[Z_I\big(J_0\hat{\boldsymbol{u}} + J_0\hat{\boldsymbol{v}}\big)\cdot\big(J_0^*\hat{\boldsymbol{u}} + J_0^*\hat{\boldsymbol{v}}\big) + Z_N\big(J_0\hat{\boldsymbol{v}} - J_0\hat{\boldsymbol{u}}\big)\cdot\big(J_0^*\hat{\boldsymbol{u}} + J_0^*\hat{\boldsymbol{v}}\big)\\ &\quad + Z_K\big(J_0\hat{\boldsymbol{u}} - J_0\hat{\boldsymbol{v}}\big)\cdot\big(J_0^*\hat{\boldsymbol{u}} + J_0^*\hat{\boldsymbol{v}}\big) + Z_L\big(J_0\hat{\boldsymbol{v}} + J_0\hat{\boldsymbol{u}}\big)\cdot\big(J_0^*\hat{\boldsymbol{u}} + J_0^*\hat{\boldsymbol{v}}\big)\big]\\ =& \operatorname{Re}\big[Z_I\,2\,|J_0|^2 + Z_N\big(|J_0|^2 - |J_0|^2\big) + Z_K\big(|J_0|^2 - |J_0|^2\big) + Z_L\,2\,|J_0|^2\big]\\ =& (\operatorname{Re}Z_I + \operatorname{Re}Z_L)\,2\,|J_0|^2\,,\end{aligned} \tag{B.8}$$

which, by considering the already established requirement $\operatorname{Re} Z_I = 0$, reduces to

$$\operatorname{Re} Z_L = 0. \tag{B.9}$$

Finally, looking at the PL condition for $\boldsymbol{J} = J_0\hat{\boldsymbol{u}} + J_0^*\hat{\boldsymbol{v}}$ gives

$$\begin{aligned}
0 =& \operatorname{Re}\big[Z_I\big(J_0\hat{\boldsymbol{u}} + J_0^*\hat{\boldsymbol{v}}\big)\cdot\big(J_0^*\hat{\boldsymbol{u}} + J_0\hat{\boldsymbol{v}}\big) + Z_N\big(J_0\hat{\boldsymbol{v}} - J_0^*\hat{\boldsymbol{u}}\big)\cdot\big(J_0^*\hat{\boldsymbol{u}} + J_0\hat{\boldsymbol{v}}\big) \\
&\quad + Z_K\big(J_0\hat{\boldsymbol{u}} - J_0^*\hat{\boldsymbol{v}}\big)\cdot\big(J_0^*\hat{\boldsymbol{u}} + J_0\hat{\boldsymbol{v}}\big) + Z_L\big(J_0\hat{\boldsymbol{v}} + J_0^*\hat{\boldsymbol{u}}\big)\cdot\big(J_0^*\hat{\boldsymbol{u}} + J_0\hat{\boldsymbol{v}}\big)\big] \\
=& \operatorname{Re}\big[Z_I\,2\,|J_0|^2 + Z_N\big({J_0}^2 - ({J_0}^2)^*\big) + Z_K\big(\,|J_0|^2 - |J_0|^2\,\big) + Z_L\big({J_0}^2 + ({J_0}^2)^*\big)\big] \\
=& \operatorname{Re}\big[Z_I\,2\,|J_0|^2 + Z_N\,2\mathrm{j}\operatorname{Im}({J_0}^2) + Z_L\,2\operatorname{Re}({J_0}^2)\big] \\
=& \operatorname{Re} Z_I\,2\,|J_0|^2 - \operatorname{Im} Z_N\,2\operatorname{Im}({J_0}^2) + \operatorname{Re} Z_L\,2\operatorname{Re}({J_0}^2).
\end{aligned} \tag{B.10}$$

According to (B.7) and (B.9), $\operatorname{Re} Z_I = \operatorname{Re} Z_L = 0$, and the last condition follows:

$$\operatorname{Im} Z_N = 0. \tag{B.11}$$

Therefore, the demonstration of the necessity of (B.1) is complete; it remains to be demonstrated that it is also sufficient to ensure passivity and absence of losses. Substituting a general value for the current, $\boldsymbol{J} = J_u\hat{\boldsymbol{u}} + J_v\hat{\boldsymbol{v}}$, the active power density can be written as

$$\begin{aligned}
\operatorname{Re}\tilde{p} =& \operatorname{Re}\Big\{\Big[\Big(\mathrm{j}X_I\overline{\overline{\boldsymbol{I}}} + R_N\overline{\overline{\boldsymbol{N}}} + \mathrm{j}X_K\overline{\overline{\boldsymbol{K}}} + \mathrm{j}X_L\overline{\overline{\boldsymbol{L}}}\Big)\cdot\big(J_u\hat{\boldsymbol{u}} + J_v\hat{\boldsymbol{v}}\big)\Big]\cdot\big(J_u^*\hat{\boldsymbol{u}} + J_v^*\hat{\boldsymbol{v}}\big)\Big\} \\
=& \operatorname{Re}\Big[\mathrm{j}X_I\big(J_u\hat{\boldsymbol{u}} + J_v\hat{\boldsymbol{v}}\big)\cdot\big(J_u^*\hat{\boldsymbol{u}} + J_v^*\hat{\boldsymbol{v}}\big) + R_N\big(J_u\hat{\boldsymbol{v}} - J_v\hat{\boldsymbol{u}}\big)\cdot\big(J_u^*\hat{\boldsymbol{u}} + J_v^*\hat{\boldsymbol{v}}\big) \\
&\quad + \mathrm{j}X_K\big(J_u\hat{\boldsymbol{u}} - J_v\hat{\boldsymbol{v}}\big)\cdot\big(J_u^*\hat{\boldsymbol{u}} + J_v^*\hat{\boldsymbol{v}}\big) + \mathrm{j}X_L\big(J_u\hat{\boldsymbol{v}} + J_v\hat{\boldsymbol{u}}\big)\cdot\big(J_u^*\hat{\boldsymbol{u}} + J_v^*\hat{\boldsymbol{v}}\big)\Big] \\
=& \operatorname{Re}\Big[\mathrm{j}X_I\big(\,|J_u|^2 + |J_v|^2\,\big) + R_N\big(J_uJ_v^* - J_u^*J_v\big) \\
&\quad + \mathrm{j}X_K\big(\,|J_u|^2 - |J_v|^2\,\big) + \mathrm{j}X_L\big(J_uJ_v^* + J_u^*J_v\big)\Big] \\
=& \operatorname{Re}\Big[\mathrm{j}X_I\big(\,|J_u|^2 + |J_v|^2\,\big) + R_N 2\mathrm{j}\operatorname{Im}(J_uJ_v^*) \\
&\quad + \mathrm{j}X_K\big(\,|J_u|^2 - |J_v|^2\,\big) + \mathrm{j}X_L 2\operatorname{Re}(J_uJ_v^*)\Big] \\
=& \,0,
\end{aligned} \tag{B.12}$$

for *any* value of J_u and J_v. This concludes the demonstration.

Appendix C

Far-field computation for single-layer metasurface

The ability to compute the far field radiated by currents in a multi-layer medium is fundamental in the analysis of metasurface antennas. This appendix reports the steps required for the computation of fields radiated by surface electric currents flowing on a grounded dielectric substrate, as needed for single-layer metasurfaces. Since the background medium is translationally invariant, it is useful to employ a spectral representation of the electric field in the transverse plane:

$$\boldsymbol{E}(\boldsymbol{\rho}, z) = \frac{1}{(2\pi)^2} \iint_{-\infty}^{+\infty} \tilde{\boldsymbol{E}}(\boldsymbol{k}_\rho; z)\, \mathrm{e}^{-\mathrm{j}\boldsymbol{k}_\rho \cdot \boldsymbol{\rho}}\, \mathrm{d}^2\boldsymbol{k}_\rho, \tag{C.1}$$

where $\boldsymbol{\rho} = x\hat{\boldsymbol{x}} + y\hat{\boldsymbol{y}}$. The antenna can be analyzed as an infinite aperture at the plane $z = z_0$, i.e., at the air-dielectric interface, which allows to express the spectral electric field everywhere as a function of the aperture field $\boldsymbol{E}^{\mathrm{a}}(\boldsymbol{\rho}) = \boldsymbol{E}(\boldsymbol{\rho}, z_0)$,

$$\tilde{\boldsymbol{E}}(\boldsymbol{k}_\rho; z) = \tilde{\boldsymbol{E}}^{\mathrm{a}}(\boldsymbol{k}_\rho)\, \mathrm{e}^{-\mathrm{j}k_z(z-z_0)}, \qquad \tilde{\boldsymbol{E}}^{\mathrm{a}}(\boldsymbol{k}_\rho) = \tilde{\boldsymbol{E}}(\boldsymbol{k}_\rho; z_0), \tag{C.2}$$

where the spectral electric field at the aperture is defined as

$$\tilde{\boldsymbol{E}}^{\mathrm{a}}(\boldsymbol{k}_\rho) = \iint_{-\infty}^{+\infty} \boldsymbol{E}^{\mathrm{a}}(\boldsymbol{\rho})\, \mathrm{e}^{\mathrm{j}\boldsymbol{k}_\rho \cdot \boldsymbol{\rho}}\, \mathrm{d}^2\boldsymbol{\rho}. \tag{C.3}$$

The objective is to compute the electric field in the upper half-space, i.e., for $0 \leq \theta < \pi/2$. For a given observation direction, identified by the spherical angles (θ, ϕ), the spectral integral (C.1) is amenable to an asymptotic approximation. By using the *stationary phase* method, the stationary point $\boldsymbol{k}^\star$ is found to be

$$\begin{aligned} \boldsymbol{k}^\star &= k_0 \left(\sin\theta \cos\phi \,\hat{\boldsymbol{x}} + \sin\theta \sin\phi \,\hat{\boldsymbol{y}} + \cos\theta \,\hat{\boldsymbol{z}}\right) \\ &= k_0 \left(\sin\theta \,\hat{\boldsymbol{\rho}} + \cos\theta \,\hat{\boldsymbol{z}}\right) \\ &= k_0 \,\hat{\boldsymbol{r}}. \end{aligned} \tag{C.4}$$

It is worth noting that this stationary point is in the same direction of the observation point. After some lengthy calculation, the integral (C.1) simplifies to

$$\boldsymbol{E}^{\text{far}} \approx \text{j}k_0 \frac{\text{e}^{-\text{j}k_0 r}}{2\pi r} \,\text{e}^{\text{j}k_z^\star z_0} \cos\theta \,\tilde{\boldsymbol{E}}^{\text{a}}(\boldsymbol{k}_\rho^\star). \tag{C.5}$$

Finally, the magnetic field in the far region is easily derived from the electric field,

$$\boldsymbol{H}^{\text{far}} = \frac{1}{\eta_0} \,\hat{\boldsymbol{r}} \times \boldsymbol{E}^{\text{far}}, \tag{C.6}$$

with $\eta_0 = \sqrt{\mu_0/\varepsilon_0}$ the free space impedance.

The transverse quantities are naturally expressed in the cylindrical coordinate system, while the far field is usually given in spherical coordinates. Starting from the spectral electric field in the cylindrical coordinate system, $\tilde{\boldsymbol{E}} = \tilde{E}_\rho \,\hat{\boldsymbol{\rho}} + \tilde{E}_\phi \,\hat{\boldsymbol{\phi}} + \tilde{E}_z \,\hat{\boldsymbol{z}}$, the spherical components can be written as

$$\begin{cases} \tilde{E}_r = \tilde{E}_\rho \sin\theta + \tilde{E}_z \cos\theta \\ \tilde{E}_\theta = \tilde{E}_\rho \cos\theta - \tilde{E}_z \sin\theta \\ \tilde{E}_\phi = \tilde{E}_\phi \end{cases} \tag{C.7}$$

By requiring that the spectral field satisfies Maxwell's equations in a homogeneous medium,

$$\nabla \cdot \boldsymbol{E} = 0 \qquad \longrightarrow \qquad \tilde{\boldsymbol{E}} \cdot \boldsymbol{k} = 0. \tag{C.8}$$

At the stationary point, by substituting (C.4) in (C.8), one finds

$$k_0 \left(\tilde{E}_\rho \sin\theta + \tilde{E}_z \cos\theta \right) = 0 \tag{C.9}$$

$$\longrightarrow \quad \tilde{E}_z = -\frac{\sin\theta}{\cos\theta}\, \tilde{E}_\rho. \tag{C.10}$$

With (C.10), (C.7) can be rewritten as

$$\begin{cases} \tilde{E}_r = 0 \\ \tilde{E}_\theta = \dfrac{\tilde{E}_\rho}{\cos\theta} \\ \tilde{E}_\phi = \tilde{E}_\phi \end{cases} \tag{C.11}$$

Finally, the electric far field (C.5) can be expressed as a function of the cylindrical components of the aperture field. The spherical components of the far field, $\boldsymbol{E}^{\mathrm{far}} = E_\theta^{\mathrm{far}} \hat{\boldsymbol{\theta}} + E_\phi^{\mathrm{far}} \hat{\boldsymbol{\phi}}$, are found by substituting (C.11) inside (C.5),

$$E_\theta^{\mathrm{far}} = \mathrm{j}k_0 \frac{\mathrm{e}^{-\mathrm{j}k_0 r}}{2\pi r}\, \mathrm{e}^{\mathrm{j}k_z^\star z_0}\, \tilde{E}_\rho^{\mathrm{a}}(\boldsymbol{k}_\rho^\star), \tag{C.12}$$

$$E_\phi^{\mathrm{far}} = \mathrm{j}k_0 \frac{\mathrm{e}^{-\mathrm{j}k_0 r}}{2\pi r}\, \mathrm{e}^{\mathrm{j}k_z^\star z_0} \cos\theta\, \tilde{E}_\phi^{\mathrm{a}}(\boldsymbol{k}_\rho^\star), \tag{C.13}$$

Until now, the expression for the far field has been given in terms of the spectral electric field. There remains to express it as a function of the source current. For this, the transversal fields are decomposed in TE and TM modes [34]. For the stationary phase point $\boldsymbol{k}^\star$, the transverse spectral basis $(\hat{\boldsymbol{k}}_\rho^\star, \hat{\boldsymbol{z}} \times \hat{\boldsymbol{k}}_\rho^\star)$ coincides with that of the spatial observation direction $(\hat{\boldsymbol{\rho}}, \hat{\boldsymbol{\phi}})$, which allows to write

$$\tilde{E}_\rho^{\mathrm{a}}(\boldsymbol{k}_\rho^\star) = V^{\mathrm{TM}}(\boldsymbol{k}_\rho^\star; z_0), \tag{C.14}$$

$$\tilde{E}_\phi^{\mathrm{a}}(\boldsymbol{k}_\rho^\star) = V^{\mathrm{TE}}(\boldsymbol{k}_\rho^\star; z_0), \tag{C.15}$$

where V^{TE} and V^{TM} are the TE and TM longitudinal transmission line voltages, respectively. For the case of surface currents residing on the plane $z = z_0$, $\boldsymbol{J} = \boldsymbol{J}_{\mathrm{s}}(\boldsymbol{\rho})\, \delta(z - z_0)$, the expression of these voltages reduces to

$$V^{\mathrm{TM}}(\boldsymbol{k}_\rho^\star; z_0) = -g^{\mathrm{TM}}(\boldsymbol{k}_\rho^\star)\, \hat{\boldsymbol{\rho}} \cdot \tilde{\boldsymbol{J}}_{\mathrm{s}}(\boldsymbol{k}_\rho^\star), \tag{C.16}$$

$$V^{\mathrm{TE}}(\boldsymbol{k}_\rho^\star; z_0) = -g^{\mathrm{TE}}(\boldsymbol{k}_\rho^\star)\, \hat{\boldsymbol{\phi}} \cdot \tilde{\boldsymbol{J}}_{\mathrm{s}}(\boldsymbol{k}_\rho^\star), \tag{C.17}$$

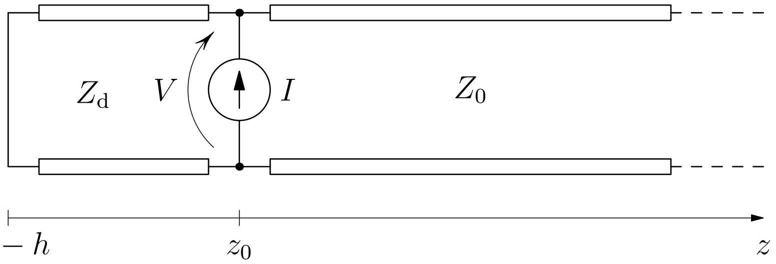

Fig. C.1 Equivalent transmission line for a grounded dielectric substrate. Sources are confined at $z = z_0$.

where g^TE and g^TM are the transmission line transfer functions. The spectral surface current is defined as

$$\tilde{\boldsymbol{J}}_\mathrm{s}(\boldsymbol{k}_\rho^\star) = \iint\limits_{-\infty}^{+\infty} \boldsymbol{J}_\mathrm{s}(\boldsymbol{\rho}')\,\mathrm{e}^{\mathrm{j}\boldsymbol{k}_\rho^\star\cdot\boldsymbol{\rho}'}\,\mathrm{d}^2\boldsymbol{\rho}'. \tag{C.18}$$

With these definitions, the final expression for the far electric field is given by

$$\boldsymbol{E}^\mathrm{far} \approx -\mathrm{j}k_0 \frac{\mathrm{e}^{-\mathrm{j}k_0 r}}{2\pi r}\,\mathrm{e}^{\mathrm{j}k_z^\star z_0}\left[g^\mathrm{TM}(\boldsymbol{k}_\rho^\star)\hat{\boldsymbol{\theta}}\hat{\boldsymbol{\rho}} + \cos\phi\, g^\mathrm{TE}(\boldsymbol{k}_\rho^\star)\hat{\boldsymbol{\phi}}\hat{\boldsymbol{\phi}}\right]\cdot\tilde{\boldsymbol{J}}_\mathrm{s}(\boldsymbol{k}_\rho^\star). \tag{C.19}$$

Equivalent Transmission Line Green's function

For the case of a single layer metasurface, the equivalent transmission line problem is the one in Fig. C.1, where all the quantities depend on the transverse wavevector $\boldsymbol{k}_\rho$. The distinction between TE and TM cases will be made explicit when needed. The impedances for the two cases are written in terms of the longitudinal wavevectors as

$$Z_0^\mathrm{TE} = \frac{\omega\mu_0}{k_{0z}}, \qquad Z_\mathrm{d}^\mathrm{TE} = \frac{\omega\mu_0}{k_{\mathrm{d}z}}, \tag{C.20}$$

$$Z_0^\mathrm{TM} = \frac{k_{0z}}{\omega\varepsilon_0}, \qquad Z_\mathrm{d}^\mathrm{TM} = \frac{k_{\mathrm{d}z}}{\omega\varepsilon_0\varepsilon_\mathrm{r}}, \tag{C.21}$$

where

$$k_{0z} = \sqrt{{k_0}^2 - |\boldsymbol{k}_\rho|^2}, \tag{C.22}$$

$$k_{\mathrm{d}z} = \sqrt{\varepsilon_\mathrm{r}{k_0}^2 - |\boldsymbol{k}_\rho|^2}. \tag{C.23}$$

By considering that a shorted transmission line segment of length h has an equivalent

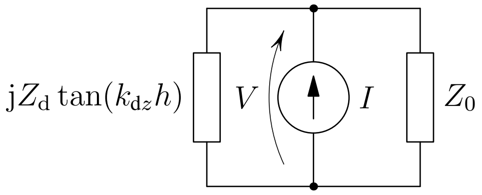

Fig. C.2 Simplified circuit for finding the transmission line transfer function.

input impedance of $\mathrm{j}Z_\mathrm{d}\tan(k_{\mathrm{d}z}h)$, and that an infinite length transmission line has an input impedance equal to its characteristic one, the problem reduces to that in Fig. C.2. The transfer functions are then easily computed as the parallel of the two equivalent impedances on the two sides,

$$g(\boldsymbol{k}_\rho) = \frac{V}{I} = \frac{\mathrm{j}Z_0 Z_\mathrm{d}\tan(k_{\mathrm{d}z}h)}{Z_0 + \mathrm{j}Z_\mathrm{d}\tan(k_{\mathrm{d}z}h)} = \frac{\mathrm{j}Z_\mathrm{d}\tan(k_{\mathrm{d}z}h)}{1 + \mathrm{j}(Z_\mathrm{d}/Z_0)\tan(k_{\mathrm{d}z}h)}. \tag{C.24}$$

Appendix D

Complex gradient

The need for a complex gradient operator arises naturally in the optimization of functions involving complex variables. Although it is always possible to express a function of complex variables as a function of the real and imaginary parts separately, this usually complicates analytical derivations. Motivated by this, in [47] a *complex gradient* operator is defined in such a way that it retains all the properties of the "classical" one that are relevant for optimization problems. This appendix summarizes the main properties and theorems, which have been used extensively in the present work.

Consider a complex vector $\mathsf{z} = \mathsf{z}' + \mathrm{j}\mathsf{z}'' \in \mathbb{C}^N$ and a function $f(\mathsf{z}) : \mathbb{C}^N \to \mathbb{C}$. The complex gradient operator is defined as

$$\tilde{\nabla} f(\mathsf{z}) \equiv \frac{1}{2}\big(\nabla' f(\mathsf{z}', \mathsf{z}'') + \mathrm{j}\nabla'' f(\mathsf{z}', \mathsf{z}'')\big), \tag{D.1}$$

where $f(\mathsf{z}', \mathsf{z}'')$ is considered a function of the real and imaginary parts of z separately, and ∇', ∇'' are (real) gradient operators acting on the real and imaginary part, respectively. A few relevant properties that follow from (D.1) are listed:

$$\tilde{\nabla}(c\, f(\mathsf{z})) = c\, \tilde{\nabla} f(\mathsf{z}), \tag{D.2a}$$

$$\tilde{\nabla}(f(\mathsf{z})g(\mathsf{z})) = f(\mathsf{z})\tilde{\nabla} g(\mathsf{z}) + g(\mathsf{z})\tilde{\nabla} f(\mathsf{z}), \tag{D.2b}$$

$$\tilde{\nabla}(h(f(\mathsf{z}))) = \left(\frac{\tilde{\partial} h^*}{\partial f}\right)^{*} \tilde{\nabla} f(\mathsf{z}) + \frac{\tilde{\partial} h}{\partial f} \tilde{\nabla} f^*(\mathsf{z}), \tag{D.2c}$$

where $c \in \mathbb{C}$, $f, g : \mathbb{C}^N \to \mathbb{C}$, and $h : \mathbb{C} \to \mathbb{C}$. Partial derivatives of a function $h(z) : \mathbb{C} \to \mathbb{C}$, $z = z' + \mathrm{j}z''$ are consistently defined as

$$\frac{\tilde{\partial} h}{\partial z} = \frac{1}{2}\left(\frac{\partial h}{\partial z'} + \mathrm{j}\frac{\partial h}{\partial z''}\right). \tag{D.3}$$

By using the definition (D.1) and properties (D.2a)–(D.2c), one can derive the complex gradient for terms that are frequently encountered in the definition of objective functions:

$$\tilde{\nabla}(\mathsf{z}^{\mathsf{H}}\mathsf{a}) = \tilde{\nabla}(\mathsf{a}^{\mathsf{T}}\mathsf{z}^*) = \mathsf{a}, \tag{D.4a}$$

$$\tilde{\nabla}(\mathsf{a}^{\mathsf{H}}\mathsf{z}) = \tilde{\nabla}(\mathsf{z}^{\mathsf{T}}\mathsf{a}) = 0, \tag{D.4b}$$

$$\tilde{\nabla}\,(\mathsf{z}^{\mathsf{H}}\mathbf{M}\mathsf{z}) = \mathbf{M}\mathsf{z}, \tag{D.4c}$$

$$\tilde{\nabla}\,|f(\mathsf{z})|^2 = \tilde{\nabla}(f(\mathsf{z})f^*(\mathsf{z})) = f^*(\mathsf{z})\tilde{\nabla}f(\mathsf{z}) + f(\mathsf{z})\tilde{\nabla}f^*(\mathsf{z}), \tag{D.4d}$$

$$\tilde{\nabla}\,\mathrm{Re}\, f(\mathsf{z}) = \tilde{\nabla}\left(\frac{1}{2}\big(f(\mathsf{z}) + f^*(\mathsf{z})\big)\right) = \frac{1}{2}\big(\tilde{\nabla}f(\mathsf{z}) + \tilde{\nabla}f^*(\mathsf{z})\big), \tag{D.4e}$$

$$\tilde{\nabla}\,\mathrm{Im}\, f(\mathsf{z}) = \tilde{\nabla}\left(\frac{1}{2\mathrm{j}}\big(f(\mathsf{z}) - f^*(\mathsf{z})\big)\right) = \frac{1}{2\mathrm{j}}\big(\tilde{\nabla}f(\mathsf{z}) - \tilde{\nabla}f^*(\mathsf{z})\big), \tag{D.4f}$$

where $\mathsf{a} \in \mathbb{C}^N$ and $\mathbf{M} \in \mathbb{C}^{N\times N}$. The following theorems establish the usefulness of the complex gradient operator in the optimization of functions of complex variables.

Theorem 1. *Let $f : \mathbb{C}^N \to \mathbb{R}$ be a real-valued scalar function whose gradients with respect to the real and imaginary parts exist everywhere. Then, the condition $\tilde{\nabla}f = 0$ is necessary and sufficient to determine a stationary point for f.*

Proof. the function f can be expressed as a real function of the $2N$ variables z'_k and z''_k, hence f is stationary if, and only if, $\partial f/\partial z'_k = 0$, $\partial f/\partial z''_k = 0$ for $k = 1, \ldots, N$. From the definition of the complex gradient one has

$$\frac{\tilde{\partial} f}{\partial z_k} = \frac{1}{2}\left(\frac{\partial f}{\partial z'_k} + \mathrm{j}\frac{\partial h}{\partial z''_k}\right). \tag{D.5}$$

Equating the real and imaginary parts of the equation for the stationary condition, the result is that is verified if, and only if, $\frac{\tilde{\partial} f}{\partial z_k} = 0$ for $k = 1, \ldots, N$, i.e., if and only if $\tilde{\nabla}f = 0$. $\square$

Theorem 2. *Let* $f : \mathbb{C}^N \to \mathbb{R}$ *be a real-valued scalar function whose complex gradient exists in a point* $\mathsf{z}_0 \in \mathbb{C}^N$. *The complex gradient* $\tilde{\nabla} f$ *defines the direction of the maximum rate of change of* f *in a neighbourhood of* z_0.

Proof. For an infinitesimal variable change $\delta\mathsf{z}$, the change in the function value is given by

$$\begin{aligned} \delta f &= f(\mathsf{z}_0 + \delta\mathsf{z}) - f(\mathsf{z}_0) \\ &= (\nabla' f)^{\mathsf{T}} \delta z' + (\nabla'' f)^{\mathsf{T}} \delta z'' = 2\,\mathrm{Re}\left[(\tilde{\nabla} f)^{\mathsf{H}} \delta\mathsf{z}\right]. \end{aligned} \tag{D.6}$$

From Schwarz's inequality, the following holds:

$$\left|\,\mathrm{Re}\left[(\tilde{\nabla} f)^{\mathsf{H}} \delta\mathsf{z}\right]\right| \leq \left|(\tilde{\nabla} f)^{\mathsf{H}} \delta\mathsf{z}\,\right| \leq \left\|\tilde{\nabla} f\right\| \left\|\delta\mathsf{z}\right\|, \tag{D.7}$$

where the norm of a complex array is defined as $\|\mathsf{a}\| = \left(\sum_k |a_k|^2\right)^{\frac{1}{2}}$. Equality only holds when $\delta\mathsf{z} = c\,\tilde{\nabla} f$, where $c \in \mathbb{R}$, i.e., when the increment is in the same direction as the gradient. In this case

$$|\delta f| = 2\,|c|\,\left\|\tilde{\nabla} f\right\|^2. \tag{D.8}$$

□

Notation and Acronyms

Notation	Description
a	Scalar in $\mathbb{R}$ or $\mathbb{C}$
$\boldsymbol{r}$	Position vector in $\mathbb{R}^3$
$\boldsymbol{E}$	Geometric vector in $\mathbb{R}^3$ or $\mathbb{C}^3$
$\hat{\boldsymbol{u}}$	Unit vector in $\mathbb{R}^3$ or $\mathbb{C}^3$
a	1-dimensional array, column vector in $\mathbb{R}^n$ or $\mathbb{C}^n$
$\boldsymbol{\mathsf{A}}$	2-dimensional array, matrix in $\mathbb{R}^{m\times n}$ or $\mathbb{C}^{m\times n}$
$\mathcal{L}$	Linear operator
$(\mathsf{v})_n$, v_n	n-th element of a vector
$(\boldsymbol{\mathsf{A}})_{mn}$, A_{mn}	(m, n) element of a matrix
$\mathrm{Re}\,(z)$, $\mathrm{Im}\,(z)$	Real part, imaginary part
$\lvert z\rvert$, $\lvert\boldsymbol{r}\rvert$	Absolute value, Euclidean norm for geometric vectors
$\lVert\mathsf{a}\rVert$	2-norm for column arrays
z^*, a^*, $\boldsymbol{\mathsf{A}}^*$	Conjugate
a^T, $\boldsymbol{\mathsf{A}}^\mathsf{T}$	Transpose
a^H, $\boldsymbol{\mathsf{A}}^\mathsf{H}$	Hermitian (conjugate) transpose
$\mathcal{L}^\mathsf{T}$	Transpose operator
$\mathcal{L}^\mathsf{H}$	Adjoint operator
$\langle\, \boldsymbol{f}\,, \boldsymbol{g}\,\rangle$	Bilinear product
$\boldsymbol{f}\cdot\boldsymbol{g}$	Dot product
$\boldsymbol{f}\times\boldsymbol{g}$	Cross product
$\mathsf{a}\odot\mathsf{b}$	Element-wise product
$\frac{\mathrm{d}f}{\mathrm{d}x}$, $f'(x)$	Derivative
∇f	Gradient
$\tilde{\nabla} f$	Complex gradient
$\partial\mathcal{V}$	Boundary of a domain

Table 5.1 Common notations

Acronym	Meaning
IBC	Impedance Boundary Condition
MoM	Method of Moments
EFIE	Electric Field Integral Equation
EFIO	Electric Field Integral Operator
SIE	Surface Integral Equation
FF	Far-field
RWG	Rao-Wilton-Glisson
FFT	Fast Fourier Transform
GMRES	Generalized Minimal Residual
PEC	Perfect Electric Conductor
MTS	Metasurface

Table 5.2 Common acronyms

Publications

1. Marcello Zucchi, Giorgio Giordanengo, Marco Righero, Javier Leonardo Araque, and Giuseppe Vecchi. Optimization of a Flat Directive antenna for 2.4 GHz band using Genetic Algorithm. *2019 13th European Conference on Antennas and Propagation (EUCAP)*, Kraków, April 2019.

2. Rossella Gaffoglio, Marcello Zucchi, Giuseppe Vecchi, and Bruno Sacco. A Numerical Analysis of Compact/Wideband Antenna Performance for DTT Reception on Mobile Terminals. *2019 13th European Conference on Antennas and Propagation (EUCAP)*, Kraków, April 2019.

3. Marcello Zucchi, Giorgio Giordanengo, Marco Righero, and Giuseppe Vecchi. First demonstration of machine-designed ultra-flat, low-cost directive antenna. *Scientific Reports*, 10(10506), June 2020.

4. Marcello Zucchi, Francesco Vernì, Marco Righero, and Giuseppe Vecchi. Automated Synthesis of Metasurface Antennas. *2021 15th European Conference on Antennas and Propagation (EuCAP)*, Düsseldorf, March 2021.

5. Rossella Gaffoglio, Marco Righero, Giorgio Giordanengo, Marcello Zucchi, and Giuseppe Vecchi. Fast Optimization of Temperature Focusing in Hyperthermia Treatment of Sub-Superficial Tumors. *IEEE Journal of Electromagnetics, RF and Microwaves in Medicine and Biology*, 5(3):286–293, September 2021.

6. Marcello Zucchi, Francesco Vernì, Marco Righero, and Giuseppe Vecchi. A Current-Based Algorithm for the Design of Metasurface Antennas. *2022 16th European Conference on Antennas and Propagation (EuCAP)*, Madrid, April 2022.

7. Marcello Zucchi, Marco Righero, and Giuseppe Vecchi. Current-Based Full-Wave Synthesis of Reactive Metasurface Antennas. *2022 IEEE International Symposium on Antennas and Propagation and USNC-URSI Radio Science Meeting*, Denver, July 2022.

8. Marcello Zucchi, Francesco Vernì, Marco Righero, and Giuseppe Vecchi. Current-Based Automated Design of Realizable Metasurface Antennas with Arbitrary Pattern Constraints. *TechRxiv*. Preprint. https://doi.org/10.36227/techrxiv.20425260.v1.

References

[1] S. Maci, G. Minatti, M. Casaletti, and M. Bosiljevac. Metasurfing: Addressing Waves on Impenetrable Metasurfaces. *IEEE Antennas and Wireless Propagation Letters*, 10:1499–1502, 2011.

[2] Yuanwei Liu, Xiao Liu, Xidong Mu, Tianwei Hou, Jiaqi Xu, Marco Di Renzo, and Naofal Al-Dhahir. Reconfigurable Intelligent Surfaces: Principles and Opportunities. *IEEE Communications Surveys Tutorials*, 23(3):1546–1577, 2021.

[3] E. F. Kuester, M. A. Mohamed, M. Piket-May, and C. L. Holloway. Averaged transition conditions for electromagnetic fields at a metafilm. *IEEE Transactions on Antennas and Propagation*, 51(10):2641–2651, October 2003.

[4] Valentina Sozio, Enrica Martini, Francesco Caminita, Paolo De Vita, Marco Faenzi, Andrea Giacomini, Marco Sabbadini, Stefano Maci, and Giuseppe Vecchi. Design and Realization of a Low Cross-Polarization Conical Horn With Thin Metasurface Walls. *IEEE Transactions on Antennas and Propagation*, 68(5):3477–3486, May 2020.

[5] Gabriele Minatti, Marco Faenzi, Enrica Martini, Francesco Caminita, Paolo De Vita, David González-Ovejero, Marco Sabbadini, and Stefano Maci. Modulated Metasurface Antennas for Space: Synthesis, Analysis and Realizations. *IEEE Transactions on Antennas and Propagation*, 63(4):1288–1300, April 2015.

[6] A. M. Patel and A. Grbic. Effective Surface Impedance of a Printed-Circuit Tensor Impedance Surface (PCTIS). *IEEE Transactions on Microwave Theory and Techniques*, 61(4):1403–1413, April 2013.

[7] G. Minatti, F. Caminita, M. Casaletti, and S. Maci. Spiral Leaky-Wave Antennas Based on Modulated Surface Impedance. *IEEE Transactions on Antennas and Propagation*, 59(12):4436–4444, December 2011.

[8] Gabriele Minatti, Francesco Caminita, Enrica Martini, Marco Sabbadini, and Stefano Maci. Synthesis of Modulated-Metasurface Antennas With Amplitude, Phase, and Polarization Control. *IEEE Transactions on Antennas and Propagation*, 64(9):3907–3919, September 2016.

[9] A. M. Patel and A. Grbic. Modeling and Analysis of Printed-Circuit Tensor Impedance Surfaces. *IEEE Transactions on Antennas and Propagation*, 61(1):211–220, January 2013.

[10] Stewart Pearson and Sean Victor Hum. Optimization of Electromagnetic Metasurface Parameters Satisfying Far-Field Criteria. *IEEE Transactions on Antennas and Propagation*, pages 1–1, 2021.

[11] Trevor Brown, Chaitanya Narendra, Yousef Vahabzadeh, Christophe Caloz, and Puyan Mojabi. On the Use of Electromagnetic Inversion for Metasurface Design. *IEEE Transactions on Antennas and Propagation*, 68(3):1812–1824, March 2020.

[12] Trevor Brown, Yousef Vahabzadeh, Christophe Caloz, and Puyan Mojabi. Electromagnetic Inversion With Local Power Conservation for Metasurface Design. *IEEE Antennas and Wireless Propagation Letters*, 19(8):1291–1295, August 2020.

[13] Trevor Brown and Puyan Mojabi. Cascaded Metasurface Design Using Electromagnetic Inversion With Gradient-Based Optimization. *IEEE Transactions on Antennas and Propagation*, 70(3):2033–2045, March 2022.

[14] Chaitanya Narendra, Trevor Brown, and Puyan Mojabi. Gradient-Based Electromagnetic Inversion for Metasurface Design Using Circuit Models. *IEEE Transactions on Antennas and Propagation*, 70(3):2046–2058, March 2022.

[15] Roberta Palmeri, Martina Teresa Bevacqua, Andrea Francesco Morabito, and Tommaso Isernia. Design of Artificial-Material-Based Antennas Using Inverse Scattering Techniques. *IEEE Transactions on Antennas and Propagation*, 66(12):7076–7090, December 2018.

[16] Jordan Budhu, Eric Michielssen, and Anthony Grbic. The Design of Dual Band Stacked Metasurfaces Using Integral Equations. *IEEE Transactions on Antennas and Propagation*, pages 1–1, 2022.

[17] J. Budhu and A. Grbic. Perfectly Reflecting Metasurface Reflectarrays: Mutual Coupling Modeling Between Unique Elements Through Homogenization. *IEEE Transactions on Antennas and Propagation*, 69(1):122–134, January 2021.

[18] Marco Di Renzo, Fadil H. Danufane, and Sergei Tretyakov. Communication Models for Reconfigurable Intelligent Surfaces: From Surface Electromagnetics to Wireless Networks Optimization. October 2021.

[19] M. Bodehou, C. Craeye, E. Martini, and I. Huynen. A Quasi-Direct Method for the Surface Impedance Design of Modulated Metasurface Antennas. *IEEE Transactions on Antennas and Propagation*, 67(1):24–36, January 2019.

[20] M. Bodehou, C. Craeye, and I. Huynen. Electric Field Integral Equation-Based Synthesis of Elliptical-Domain Metasurface Antennas. *IEEE Transactions on Antennas and Propagation*, 67(2):1270–1274, February 2019.

[21] Modeste Bodehou, Enrica Martini, Stefano Maci, Isabelle Huynen, and Christophe Craeye. Multibeam and Beam Scanning With Modulated Metasurfaces. *IEEE Transactions on Antennas and Propagation*, 68(3):1273–1281, March 2020.

[22] Giacomo Oliveri, Paolo Rocca, Marco Salucci, and Andrea Massa. Holographic Smart EM Skins for Advanced Beam Power Shaping in Next Generation Wireless Environments. *IEEE Journal on Multiscale and Multiphysics Computational Techniques*, 6:171–182, 2021.

[23] Marco Salucci, Angelo Gelmini, Giacomo Oliveri, Nicola Anselmi, and Andrea Massa. Synthesis of Shaped Beam Reflectarrays With Constrained Geometry by Exploiting Nonradiating Surface Currents. *IEEE Transactions on Antennas and Propagation*, 66(11):5805–5817, November 2018.

[24] Brian B. Tierney and Anthony Grbic. Designing Anisotropic, Inhomogeneous Metamaterial Devices Through Optimization. *IEEE Transactions on Antennas and Propagation*, 67(2):998–1009, February 2019.

[25] Luke Szymanski, Gurkan Gok, and Anthony Grbic. Inverse Design of Multi-Input Multi-Output 2-D Metastructured Devices. *IEEE Transactions on Antennas and Propagation*, 70(5):3495–3505, May 2022.

[26] Francesco Caminita, Enrica Martini, Gabriele Minatti, Marco Sabbadini, and Stefano Maci. Low-Profile Dual-Polarized Isoflux Antennas for Space Applications. *IEEE Transactions on Antennas and Propagation*, 69(6):3204–3213, June 2021.

[27] Francesco Vernì. *Advanced Computational Electromagnetics for Metasurfaces*. PhD thesis, Politecnico di Torino, August 2020.

[28] Francesco Vernì, Marco Righero, and Giuseppe Vecchi. On the Use of Entire-Domain Basis Functions and Fast Factorizations for the Design of Modulated Metasurface. *IEEE Transactions on Antennas and Propagation*, 68(5):3824–3833, May 2020.

[29] Slawomir Koziel, Muhammad Abdullah, and Stanislaw Szczepanski. Design of High-Performance Scattering Metasurfaces Through Optimization-Based Explicit RCS Reduction. *IEEE Access*, 9:113077–113088, 2021.

[30] I.V. Lindell, A.H. Sihvola, and I. Hanninen. Perfectly anisotropic impedance boundary. *Antennas Propagation IET Microwaves*, 1(3):561–566, June 2007.

[31] Constantine A. Balanis. *Antenna Theory: Analysis and Design*. John Wiley & Sons, December 2012.

[32] K. A. Michalski and J. R. Mosig. Multilayered media Green's functions in integral equation formulations. *IEEE Transactions on Antennas and Propagation*, 45(3):508–519, March 1997.

[33] M. A. Francavilla, E. Martini, S. Maci, and G. Vecchi. On the Numerical Simulation of Metasurfaces With Impedance Boundary Condition Integral Equations. *IEEE Transactions on Antennas and Propagation*, 63(5):2153–2161, May 2015.

[34] Krzysztof Arkadiusz Michalski. Electromagnetic Field Computation in Planar Multilayers. In *Encyclopedia of RF and Microwave Engineering*. John Wiley & Sons, Ltd, 2005.

[35] Roger F. Harrington. *Field Computation by Moment Methods*. IEEE, Piscataway, NJ, reprint edizione edition, April 1993.

[36] S. Rao, D. Wilton, and A. Glisson. Electromagnetic scattering by surfaces of arbitrary shape. *IEEE Transactions on Antennas and Propagation*, 30(3):409–418, May 1982.

[37] Weng Cho Chew, Jian-Ming Jin, Eric Michielssen, and Jiming Song. *Fast and Efficient Algorithms in Computational Electromagnetics*. Artech House, Boston, 2001.

[38] Seung Mo Seo and Jin-Fa Lee. A fast IE-FFT algorithm for solving PEC scattering problems. *IEEE Transactions on Magnetics*, 41(5):1476–1479, May 2005.

[39] Fasenfest, Capolino, Wilton, Jackson, and Champagne. A fast MoM solution for large arrays: Green's function interpolation with FFT. *IEEE Antennas and Wireless Propagation Letters*, 3:161–164, 2004.

[40] A. Ludwig. The definition of cross polarization. *IEEE Transactions on Antennas and Propagation*, 21(1):116–119, January 1973.

[41] R. W. Gerchberg and W. O. Saxton. A practical algorithm for the determination of the phase from image and diffraction plane pictures. *Optik*, 2:237–246, 1972.

[42] L. M. Brègman. Finding the common point of convex sets by the method of successive projection. *Doklady Akademii Nauk SSSR*, 162:487–490, 1965.

[43] O. M. Bucci, G. Franceschetti, G. Mazzarella, and G. Panariello. Intersection approach to array pattern synthesis. *Antennas and Propagation IEE Proceedings H - Microwaves*, 137(6):349–357, December 1990.

[44] Marcello Zucchi, Francesco Vernì, Marco Righero, and Giuseppe Vecchi. Automated Synthesis of Metasurface Antennas. In *2021 15th European Conference on Antennas and Propagation (EuCAP)*, Düsseldorf, March 2021.

[45] Jorge Nocedal and Stephen J. Wright. *Numerical Optimization*. Springer Series in Operations Research. Springer, New York, 2nd ed edition, 2006.

[46] IEEE Standard for Definitions of Terms for Antennas. *IEEE Std 145-2013 (Revision of IEEE Std 145-1993)*, pages 1–50, March 2014.

[47] D. H. Brandwood. A complex gradient operator and its application in adaptive array theory. *IEE Proceedings F (Communications, Radar and Signal Processing)*, 130(1):11–16, February 1983.

[48] Michael Grant and Stephen Boyd. CVX: Matlab software for disciplined convex programming, version 2.1, March 2014.

[49] Mei Li, Shao-Qiu Xiao, and Daniel F. Sievenpiper. Polarization-Insensitive Holographic Surfaces With Broadside Radiation. *IEEE Transactions on Antennas and Propagation*, 64(12):5272–5280, December 2016.

[50] S. Pandi, C. A. Balanis, and C. R. Birtcher. Design of Scalar Impedance Holographic Metasurfaces for Antenna Beam Formation With Desired Polarization. *IEEE Transactions on Antennas and Propagation*, 63(7):3016–3024, July 2015.

[51] P. Burghignoli, G. Lovat, and D.R. Jackson. Analysis and Optimization of Leaky-Wave Radiation at Broadside From a Class of 1-D Periodic Structures. *IEEE Transactions on Antennas and Propagation*, 54(9):2593–2604, September 2006.

[52] Ratnesh Ranjan and Jayanta Ghosh. SIW-Based Leaky-Wave Antenna Supporting Wide Range of Beam Scanning Through Broadside. *IEEE Antennas and Wireless Propagation Letters*, 18(4):606–610, April 2019.